ANALYTIC MASS RECONSTRUCTION OF TOP-ANTITOP RESONANCES IN THE DILEPTON CHANNEL AT ATLAS

by

Michelle Renée Boudreau

BSc., University of Guelph 2009

THESIS SUBMITTED IN PARTIAL FULFILLMENT

OF THE REQUIREMENTS FOR THE DEGREE OF

MASTER OF SCIENCE

IN THE

DEPARTMENT OF PHYSICS

FACULTY OF SCIENCE

© Michelle Renée Boudreau 2012

SIMON FRASER UNIVERSITY

Fall 2012

APPROVAL

Name: Michelle Renée Boudreau

Degree: Master of Science

Title of thesis: Analytic Mass Reconstruction of Top-Antitop Resonances in
                                   the Dilepton Channel at ATLAS

Examining Committee: Dr. Malcolm Kennett
                                   Associate Professor (Chair)

                                   _____

                                   Dr. Bernd Stelzer
                                   Senior Supervisor
                                   Assistant Professor

                                   _____

                                   Dr. Michel Vetterli
                                   Supervisor
                                   Professor

                                   _____

                                   Dr. Dugan O'Neil
                                   Supervisor
                                   Associate Professor

                                   _____

                                   Dr. Sarah Johnson
                                   Internal Examiner
                                   Senior Lecturer

Date Approved: November 26, 2012

Partial Copyright Licence

Abstract

Many theories beyond the Standard Model predict new massive particles that decay preferentially to top-antitop quark pairs. This thesis investigates the dilepton final state where both W bosons from the top quarks decay into leptons. This final state features the highest purity for top quarks but is kinematically under-constrained due to the presence of the two neutrinos that leave the ATLAS detector undetected. Using kinematic constraints from the top-antitop quark decay chain, along with the missing energy, leptons, and jets, that are measured with the ATLAS detector, a set of analytic solutions for the four-vectors of the neutrinos can be obtained. With this information, the invariant mass can be reconstructed up to a four-fold ambiguity. Methods used to eliminate incorrect neutrino solutions are investigated and characterized. For a resonance particle with a mass much larger than the top quark mass, the top quarks will be highly boosted, resulting in collimated decay products of the top quark. Optimizing the lepton selection in such an environment is very important and is also discussed.

À tous ceux que j'aime:

Mom, Dad, Amy, Mélanie, Justin, Eli, Mémère, Pépère, Ron, et

spécialement Ryan.

Acknowledgments

Contents

List of Tables

List of Figures

Chapter 1

Introduction

With the LHC in its third year in operation, the search for new physics beyond the Standard Model (SM) is one of the primary focuses for experimental analyses at ATLAS. Given the large center of mass energy at the LHC relative to past collider experiments, the ability to create high mass particles, if they exist, is greatly enhanced. The ability to explore a new energy frontier provides a unique opportunity to discover new physics which may have been previously kinematically inaccessible at lower energy.

This thesis focuses on the characterization of a new observable, the invariant mass, to be implemented in an analysis searching for top-antitop resonances decaying through the dilepton channel. Using ATLAS data, the invariant mass cannot be readily reconstructed since the neutrinos are not measured by the ATLAS detector. Although the algorithm in this thesis is characterized for the Kaluza-Klein gluon, which is predicted by the Randall-Sundrum model, this method can be applied in principle to any $t\bar{t}$ resonances predicted by other models which decay in the dilepton channel.

The first element investigated is the effect of lepton isolation cuts, typically used for SM $t\bar{t}$ analyses to reject background. As the mass of resonances increases, so does the p_T of top quarks originating from the decay of such a resonance, yielding more collimated decay products. In such scenarios, the isolation cuts used in lower-p_T top quark physics analyses become unfavourable, leading to increased signal rejection.

The invariant mass of the KK-gluon will be reconstructed using simulated ATLAS data and using constraints on the $t\bar{t}$ system to analytically solve for the neutrino four-vectors. Once neutrino four-vector solutions are obtained, the correct neutrino solution must be

extracted from the set of all possible solutions.

Finally, the performance of this new observable based on the limits set on the cross section is compared to the current observable used in the dilepton $t\bar{t}$ analyses, $H_T + E_T^{miss}$. The effect of the width and mass of the resonance on the performance of the invariant mass reconstruction will also be discussed.

Chapter 2

Theory

2.1   The Standard Model

The Standard Model of particle physics describes the fundamental constituents of matter and their interactions. It provides a theoretical framework for three of the four fundamental forces of nature: the strong, electromagnetic, and weak interactions. These interactions are described by quantum field theory. Currently, there is no complete quantum field theory describing the gravitational interaction, which has therefore failed to be incorporated as part of the Standard Model.

There are 12 fundamental spin-$\frac{1}{2}$ particles, or fermions, whose interactions are mediated by 4 different spin-1 particles, known as bosons [1]. Fermions are divided into three generations, where the particles in each generation have identical properties other than their mass. The first generation of quarks and leptons constitutes all observed matter. Fermions in higher generations are only directly observed in high-energy interactions because they are unstable, ultimately decaying into first generation particles. The physical properties of all of the observed Standard Model particles are listed in Tables 2.1 and 2.2 [2]. For each of the quarks and leptons there exists a corresponding antiparticle. A particle (p) and its corresponding antiparticle ($\bar{p}$) are observed to have identical masses but opposite electric charges.

Table 2.1: Properties of Quarks and Leptons, the fundamental fermions, in the Standard Model. Corresponding anti-particles have the same properties besides their charge, which is opposite in sign [2].

generation	quarks			leptons		
	flavor	charge*	mass (GeV)†	flavor	charge	mass (GeV)
I	up (u)	$\frac{2}{3}$	$1.7 - 3.1 (\times 10^{-3})$	electron (e)	-1	0.511×10^{-3}
	down (d)	$-\frac{1}{3}$	$4.1 - 5.7 (\times 10^{-3})$	elec. neutrino (ν_e)	0	0
II	charm (c)	$\frac{2}{3}$	1.29	muon (μ)	-1	0.106
	strange (s)	$-\frac{1}{3}$	0.100	muon neutrino (ν_μ)	0	0
III	top (t)	$\frac{2}{3}$	172.9	tau (τ)	-1	1.77
	bottom (b)	$-\frac{1}{3}$	4.19	tau neutrino (ν_τ)	0	0

Table 2.2: Properties of Force Mediators in the Standard Model [2].

Interaction	carrier	charge	mass (GeV)
electromagnetic	photon (γ)	0	0
weak	$W^\pm$	± 1	80.4
	Z	0	91.2
strong	gluon (g)	0	0

The electromagnetic interaction is the best understood interaction described by the Standard Model, with its quantum field theory known as Quantum Electrodynamics (QED). The electromagnetic interaction is mediated by the photon and any particle that carries electromagnetic charge couples via this interaction. As a result, all of the fundamental particles besides neutrinos can interact via the electromagnetic interaction. Another interaction which is included in the Standard Model is the weak interaction. There are two types of weak interactions: charged and neutral. The neutral weak interaction is mediated

---

*Electromagnetic charge.

†A convention where the speed of light (c) is a dimensionless quantity with magnitude equal to 1 is used throughout this thesis. This means that the kinematic quantities of mass (eV/c^2), momentum (eV/c), and energy (eV) are all expressed in units of eV. In the context of this analysis, eV is an extremely small quantity. Relevant energy ranges are on the order of 10^9 eV (GeV) or 10^{12} eV (TeV).

by the Z boson. Like the photon, the Z boson is neutral, however, it is not restricted to mediating the interaction between particles that are electromagnetically charged. As a result, Z bosons can couple to all fermions listed in Table 2.1. The charged weak interaction is mediated by the $W^\pm$ bosons. It is a unique interaction as it represents the only flavor changing interaction in the Standard Model. The $W^\pm$ bosons only couple to leptons within the same generation, which is to say that interactions such as $W \to e^- \nu_\tau$ have not been observed while $W \to e^- \nu_e$ have. This is not the case, however, for quarks. Albeit not required by the Standard model, weak mixing between different quark generations has been experimentally observed. This cross-generational coupling is represented by the Cabibbo-Kobayashi-Maskawa (CKM) quark-mixing matrix and is given by:

$$\begin{pmatrix} d' \\ s' \\ b' \end{pmatrix} = \begin{pmatrix} V_{ud} & V_{us} & V_{ub} \\ V_{cd} & V_{cs} & V_{cb} \\ V_{td} & V_{ts} & V_{tb} \end{pmatrix} \begin{pmatrix} d \\ s \\ b \end{pmatrix}, \tag{2.1}$$

where V_{ij} represents the non-zero coupling between quarks i and j, $\{d',s',b'\}$ represents weak eigenstates, and $\{d,s,b\}$ represents their mass (physical) eigenstates [2].

The strong interaction is described by the quantum field theory known as Quantum Chromodynamics (QCD). In nature, quarks cannot be isolated. This phenomenon is referred to as quark confinement [3]. Only bound states of quark-antiquark pairs known as mesons, or three (anti-)quark bound states known as baryons are observed; both are collectively referred to as hadrons. Each quark comes in three different colors: red, blue, and green. Color charge is unique to the strong interaction and as such only gluons, the mediating particle of the strong interaction, and quarks carry it. Each quark carries one unit of color, whereas gluons carry a unit of color and a unit of anti-color. Gluons couple only to particles that carry color, namely quarks and gluons.

Since the five lightest quarks are only observed as bound states, there is no direct access to their individual quark masses. Instead, quark masses are calculated based on hadron mass measurements, while taking into account the quantum chromodynamic binding energy. On the other hand, the mass of the top quark can be directly measured. Due to the large mass of the quark, it decays very quickly. Of all the quarks, it is the only quark whose lifetime (on the $O(10^{-25}s)$) is shorter than the timescale of the strong interaction (on the $O(10^{-24}s)$) and as a result it decays before forming a bound state.

The final particle predicted by the Standard Model is the spin-0 boson known as the Higgs boson. The Higgs particle plays a very important role in the Standard Model. In electroweak theory, the unified theory of the electromagnetic and weak interactions, the Higgs mechanism was introduced as the mechanism via which the electroweak gauge symmetry is broken, providing the source of mass for weak gauge bosons [4]. In the absence of such a mechanism, the *W* and *Z* bosons would be massless, which does not agree with experimental observations. Since the mass of the Higgs boson is a free parameter in the Standard Model only limits on its mass had been placed. However, on July 4th 2012, both the ATLAS and CMS experiments presented results on their Standard Model Higgs analyses, both announcing that a significant excess of Higgs candidate events was observed above Standard Model expectations. This excess corresponds to a new particle with a mass of 126.0 GeV and 125.3 GeV from ATLAS and CMS, respectively [5, 6].
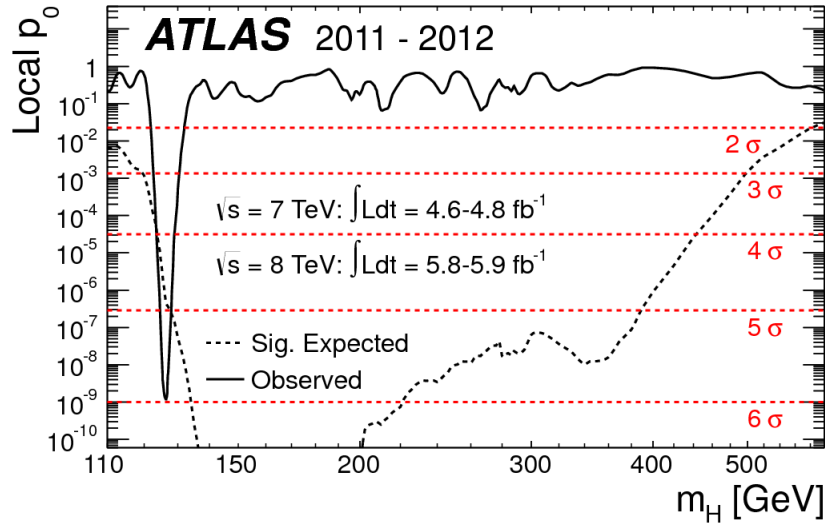
Figure 2.1: Observed (solid line) and expected (dashed line) local p_0 values for a Standard Model Higgs boson signal hypothesis as a function of the Higgs mass [5].

The corresponding plot from the ATLAS experiment is shown in Figure 2.1, which shows the local statistical significance of the observed data using a combination of Higgs decay channels and data from both $\sqrt{s} = 7$ TeV and $\sqrt{s} = 8$ TeV collisions. Although this new particle is compatible with the Standard Model Higgs boson hypothesis, more data are

needed to measure all of its properties.

2.2   Beyond the Standard Model

Although the Standard Model has had much success it may not be the most fundamental theory of nature. One reason to believe that a more fundamental theory exists stems from the fact that the Standard Model describes only a small fraction of the matter in the universe. It does not account for dark energy and dark matter. It also does not account for the full matter-antimatter asymmetry of the universe. Moreover, the Standard Model contains 18 (+ 7 for $m_\nu \neq 0$) free parameters that are not predicted by theory but are set by experimental observations; these include fermion masses, CKM mixing angles, coupling constants, m_Z and m_{Higgs}. There is also the so-called 'fine tuning' problem. In electroweak theory, quantum corrections to the Higgs mass diverge quadratically; specifically, the mass it acquires through interactions with other fields are as large as the largest mass scale in the theory. In order to prevent the Higgs mass from diverging, fine tuning which leads to cancellations between correction terms must occur. Although this is not considered to be fundamentally wrong, there may perhaps be a fundamental mechanism driving these cancellations that is currently unknown.

Many extensions to the Standard Model have been developed in order to create a more complete theory. Such extensions are collectively referred to as Beyond the Standard Model (BSM) theories. There are many theoretical approaches used to address the aforementioned problems. Some popular approaches include the concept of strings, the introduction of supersymmetric partners to Standard Model particles, or extra dimensions.

2.2.1   Basics of Kaluza-Klein Theory

Kaluza-Klein (KK) theory was introduced in the 1920's as an attempt to unify general relativity and electromagnetism [7, 8]. It is a 5-dimensional theory based on the principle of a fifth compactified dimension. Compactification refers to extra dimensions being 'curled up' into a geometrically small space such that these extra dimensions are unnoticeable on a macroscopic scale. The Kaluza-Klein setup is depicted in Figure 2.2.
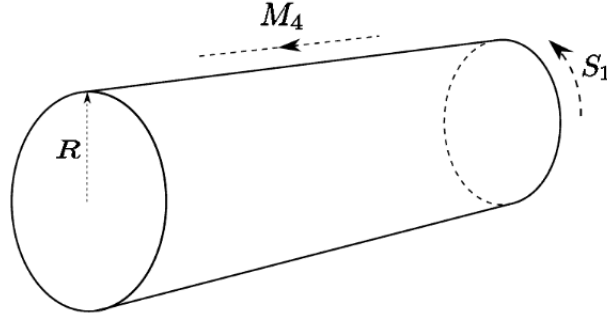
Figure 2.2: Schematic of the Kaluza-Klein setup. The additional dimension is a compactified dimension, S_1. Our 4-dimensional world is represented perpendicularly as M_4 [9].

In this setup, all quantum fields are now defined in a five dimensional space. A result of this setup provides the five dimensional scalar fields to be continuous at the boundary. This is expressed as:

$$\Phi(x_\mu, y) = \Phi(x_\mu, y + 2\pi R) = \sum_{k=0,\pm 1,...} \phi_k(x_\mu) e^{iky/R}, \tag{2.2}$$

where x_μ corresponds to four dimensional space-time coordinates ($\mu = 0, 1, 2, 3$), y corresponds to the additional coordinate of the fifth dimension, ϕ corresponds to 4-dimensional fields, Φ corresponds to 5-dimensional fields, and k represents the modes. The four dimensional field, $\phi_k(x_\mu)$, are referred to as Kaluza-Klein modes. The relevant outcome of this theory is that the zero modes ($k = 0$) correspond to four-dimensional fields for particles we currently observe and that the $k \neq 0$ modes are *massive* four-dimensional fields, which are excitations of zero mode particles. Masses for these KK excitations are given by:

$$m_k = \frac{|k|}{R}. \tag{2.3}$$

Each 4-dimensional field will give rise to KK excitations with each 'mode' of excitation being more massive. Compactification radii are typically very small and as a result the KK excitation can be extremely large [9].

In a five-dimensional space, the relativistic energy-momentum relationship is given by:

$$E^2 = (p_1 c)^2 + (p_2 c)^2 + (p_3 c)^2 + (mc^2)^2 + (p_y c)^2, \tag{2.4}$$

where p_y corresponds to the coordinate in the fifth dimension. The mass of the excitation, as observed in a four-dimensional space, is given as: $(M_y c^2)^2 = (p_y c)^2 + (mc^2)^2$.

2.2.2 The Randall-Sundrum Model

The Randall-Sundrum model will be used as a benchmark model for this thesis. This model, proposed in 1999 by Lisa Randall and Raman Sundrum involves only one extra dimension, which is warped in geometry and compactified [10]. The RS1 model where two 3-dimensional branes* are separated by a finite distance is considered. Specifically, the Planck brane and the TeV brane (the brane on or near which the Standard Model is localized) are at y = 0 and y = π, respectively, as depicted in Figure 2.3. Figure 2.3 depicts a slice of the 5-dimensional model shown in Figure 2.2.
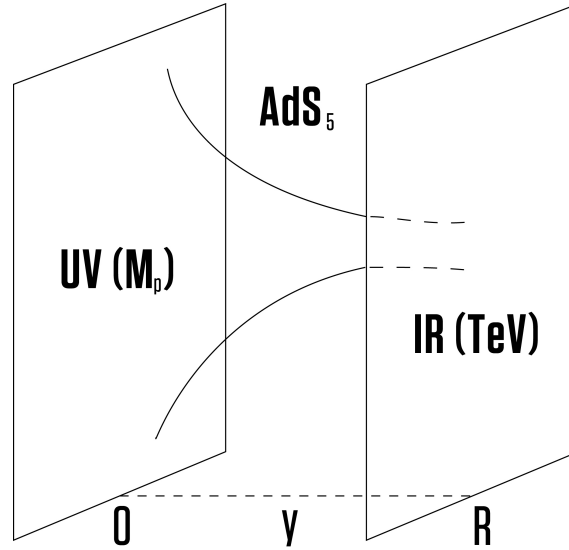
Figure 2.3: Depiction of the Randall-Sundrum scenario. One slice of the fifth dimension, containing two branes that are localized at opposite ends of the extra dimension. For this model, the TeV brane is located at R = π.

---

*Branes are topological spaces which are Lorentz invariant. For example, a 0-dimensional brane is a particle (point object) and a 1-dimensional brane is a string.

In this approach the five-dimensional metric is altered (with respect to the four-dimensional metric) by adding a five-dimensional component, and multiplying the four-dimensional Minkowski metric by a "warp" factor. It is given by:

$$ds^2 = e^{-2kR_cy}\eta_{\mu\nu}dx^\mu dx^\nu + R_c^2 dy^2, \tag{2.5}$$

where y represents the 5th-dimensional coordinate, k is a mass scale, and R_c, is the radius of compactification.

If the mass scale, k, is taken to be on the order of the Planck scale and R_c is taken on the order of the inverse of the Planck scale*, then TeV scales (with respect to the Planck scale) can naturally be attained on the TeV brane located at $y = \pi$. Observed masses are scaled by this warping factor like:

$$m = e^{-kR_c\pi}m_0, \tag{2.6}$$

where m_0 corresponds to the visible mass as observed on the TeV brane and m corresponds to the physical mass. The introduction of this warp factor provides a straightforward solution to the hierarchy problem. The weakness of gravity as perceived on our brane is not taken to be fundamental, but rather what is seen on our 3-dimensional brane is a 'diluted' version which comes as a direct result of the warping factor through the extra dimension.

In one version of the RS1 model, all Standard Model particles are localized on the TeV brane [11]. In the bulk RS1 model, the Higgs field alone is taken to be localized on the TeV; this not only resolves the hierarchy problem of gravity, but it can also resolve the mass hierarchy between fundamental particles of different flavor. If fermions are not localized on the TeV brane, but rather propagate in the bulk (the additional dimension, or space, between the two branes), the difference in the mass of particles as observed on our brane corresponds to where they are localized in the bulk. This difference can be large due to the exponential effect of the warp factor.

2.2.3   Top Quark in Beyond the Standard Model Theories

The top quark was predicted in 1973 by Maskawa and Kobayashi as a way to explain *CP* violation observed in Kaon decay. The top quark was later discovered in 1995 by the

---

*The Planck scale is the scale at which the quantum effects of gravity become strong. This (reduced) energy scale is on the order of 10^{18} GeV.

CDF [12] and D0 [13] experiments at Fermilab.

The top quark is a unique particle amongst all the fundamental particles because of its large mass. It has a mass of approximately 172.9 GeV which is substantially larger than the second heaviest quark (*b*) which has a mass of 4.2 GeV [2]. Not only is it much larger than all other quarks, its mass is also larger than any other fermion or boson observed in the Standard Model. Of the fundamental particles, it is the only particle whose mass is relatively close to the electroweak symmetry breaking scale, $v = 246$ GeV where $\mathrm{M}_{top} \approx \frac{v}{\sqrt{2}}$. The large coupling between the top quark and the mechanism of electroweak symmetry breaking provides good motivation for experimental analyses with top quarks.

The analysis presented in this thesis is relevant for any new model in which a heavy resonance decays to $t\bar{t}$. In the Randall-Sundrum model, the decay of the KK-gluon to top quarks is enhanced. This is due to the fact that top quarks have a large Yukawa coupling and as such are localized near the TeV brane. The Yukawa coupling represents the coupling between the Higgs field and the fermion fields. This coupling for the top quark is given by:

$$y_t = \frac{\sqrt{2}m_t}{v} \approx 1. \tag{2.7}$$

Calculations give the couplings of light quarks and leptons to the KK-gluon as approximately $\frac{1}{5}$ in comparison to a coupling of 5 to the right handed top quark [14].

2.2.4 Production and Decay of the Kaluza-Klein Gluon at the LHC

Of all Kaluza-Klein gauge excitations, the KK-gluon would be produced the most abundantly at the LHC due to its strong production mode [14]. At leading-order, KK-gluons are produced only by $q\bar{q}$ annihilations. Due to the flavor hierarchies discussed above, the production of KK-gluons is suppressed because of the small coupling between the KK-gluon and light quarks, the proton constituents, because they are localized far from the TeV brane. The total cross section for KK-gluon production is shown in Figure 2.4.

The dominant decay channel is given by the decay to top quarks as shown in Figure 2.5. Once the KK-gluon has a mass greater than twice the mass of the top quark, the $t\bar{t}$ channel is essentially the only relevant channel for the KK-gluon search. The large decay branching fraction to $t\bar{t}$ provides a promising channel for the discovery of a KK-gluon.
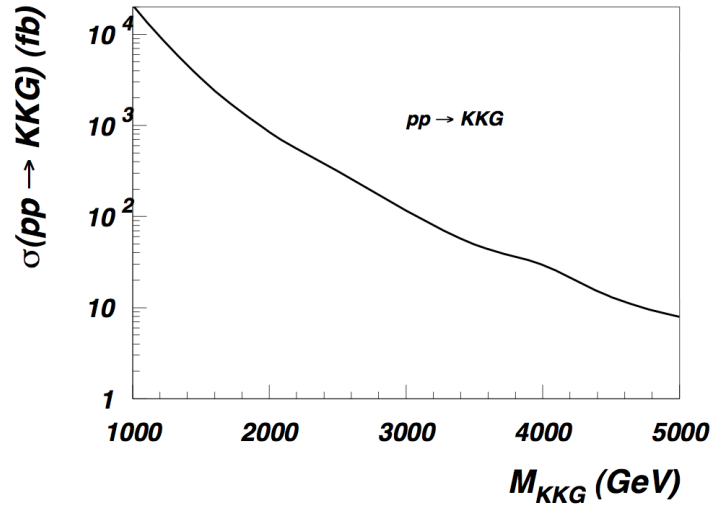
Figure 2.4: Total cross section of Kaluza-Klein gluon production as a function of its mass [14].
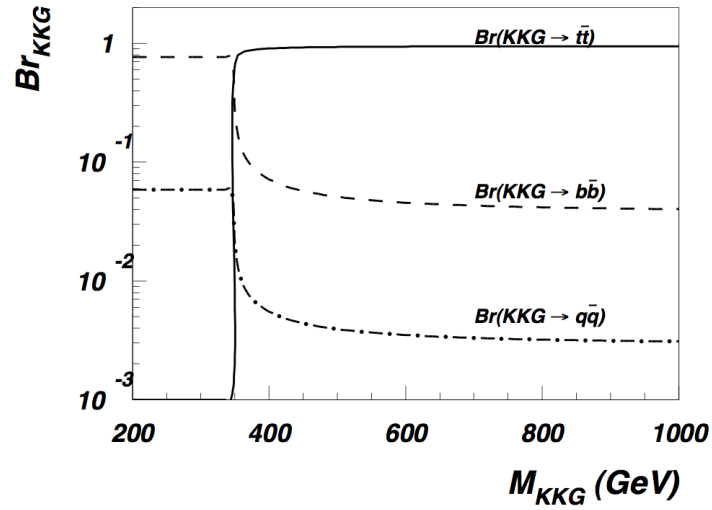
Figure 2.5: Branching ratio of Kaluza-Klein gluons to $t\bar{t}$ as a function of its mass [14].

Chapter 3

Experimental Setup

3.1 The Large Hadron Collider

The Large Hadron Collider (LHC) is a particle accelerator situated at CERN near Geneva, Switzerland. It is designed to accelerate protons up to a center of mass energy of 14 TeV and also accelerate heavy ions (Pb) up to 2.76 TeV per nucleon [15]. It is a 27 kilometre ring situated approximately 100 metres underground. The accelerator setup is shown in Figure 3.1. The acceleration process begins in the Linear Accelerator 2 (Linac2) where protons are accelerated to 50 MeV. These protons are then injected into a Proton Synchrotron Booster (PSB) that accelerates them to 1.4 GeV. The PSB protons are fed into the PS, further accelerated to 25 GeV, and injected into the Super Proton Synchrotron (SPS). The protons in the SPS are accelerated to 450 GeV and are finally injected into the LHC where protons are accelerated to (3.5) 4 TeV, resulting in collisions at a center of mass energy of (7) 8 TeV in (2011) 2012. In 2015, the LHC will accelerate protons to 6.5 TeV, leading to a center of mass energy of 13 TeV, and eventually reach 14 TeV, as designed.
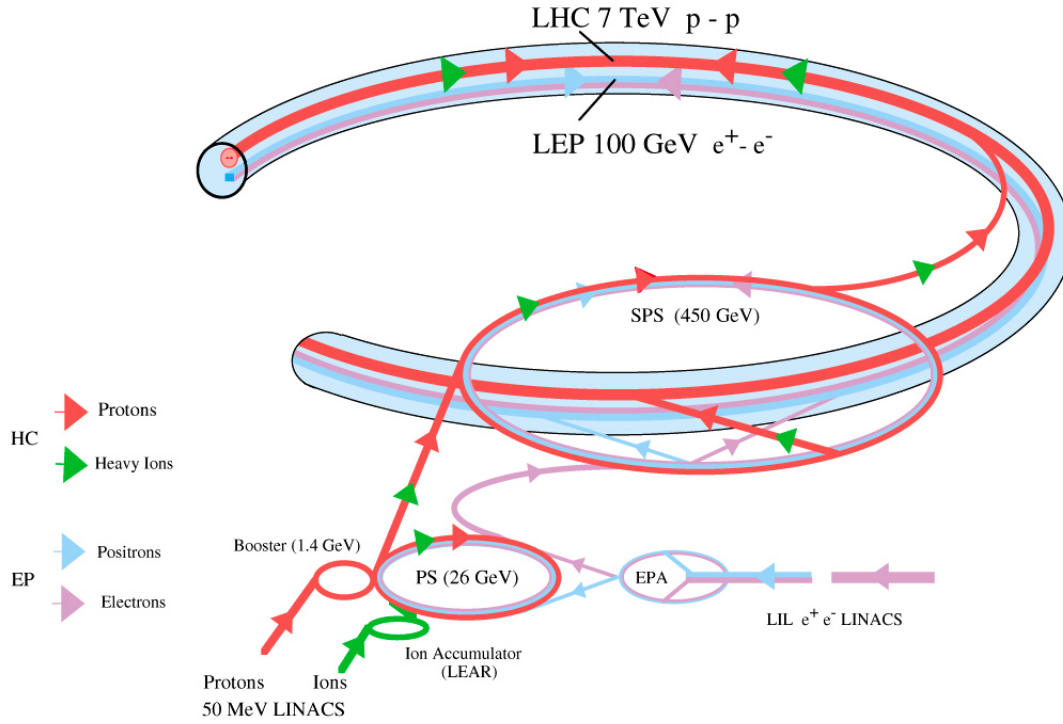
Figure 3.1: Schematic View of the Injection Chain into the LHC [16].

There are four intersection points where packets of accelerated protons, referred to as bunches, collide in the LHC tunnel. Currently, these proton bunches collide every 50 ns, with a design spacing of 25 ns. Four different experiments are located at these interaction regions:

- A Toroidal LHC ApparatuS (ATLAS)

- Compact Muon Solenoid (CMS)

- Large Hadron Collider beauty (LHCb)

- A Large Ion Collider Experiment (ALICE)

Both ATLAS and CMS are general-purpose detectors, meaning they have been designed for a diverse physics program. Both LHCb and ALICE are detectors optimized for

more specific analyses: LHCb focuses on heavy flavor physics and ALICE is optimized for analyses studying the physics of heavy ion collisions.
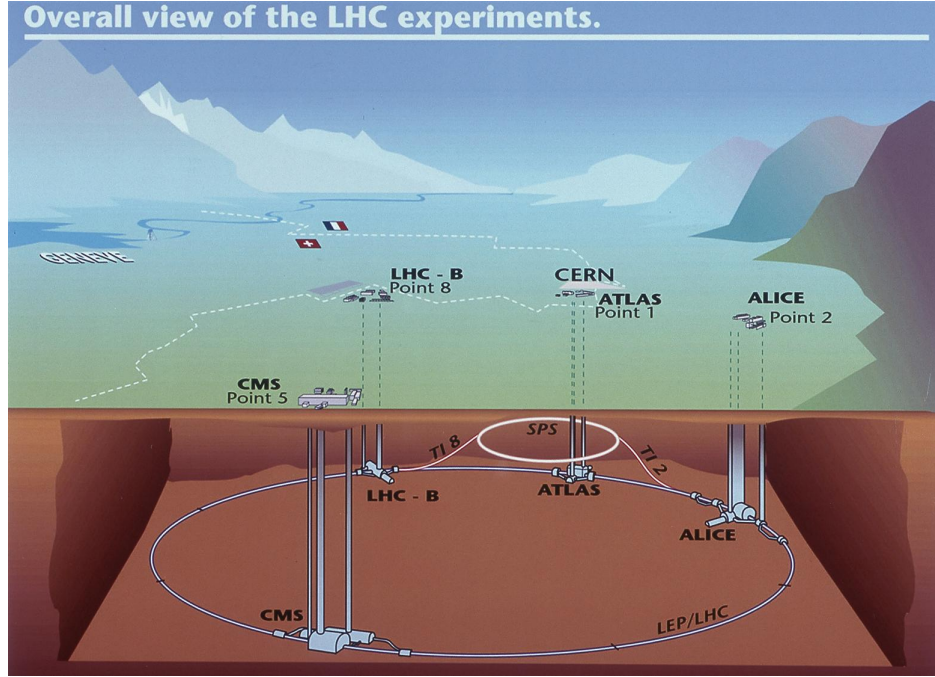
Figure 3.2: Schematic of the experiments at the LHC. ATLAS Experiment ©2012 CERN [17].

The geographic location of the interaction points, with labelled experiments, is show in Figure 3.2. There are also two more experiments at the LHC; TOTal Elastic and diffractive cross section Measurement (TOTEM), and LHC-forward (lhcf), which are located near the CMS and ATLAS collision points, respectively. The LHC will also spend a small fraction of its operation time colliding lead (or gold) ions, rather than protons, accelerated up to 2.76 TeV per nucleon.

At particle colliders, the rate at which particles collide is known as the luminosity. Since ATLAS is looking for rare interactions, a large luminosity is needed. Expressed in units of $cm^{-2}s^{-1}$, it is given by:

$$\mathcal{L} = \frac{fN_1N_2}{A}n,$$ (3.1)

where A is the cross section of the beam overlap, N_i is the number of particles in each bunch, n is the number of bunches, and f is the revolution frequency. The design luminosity of the LHC is 10^{34} cm^{-2}s^{-1}. The integrated luminosity, $\int \mathcal{L} dt$, provides a measure of how much data have been collected over the time interval dt, and is typically given in units of inverse barns (b^{-1}), where $b = 10^{-28}$ m^2. In 2011, the LHC operated at a peak luminosity of 3.65×10^{33} cm^{-2}s^{-1} and delivered a total of $\int \mathcal{L} dt = 5.61$ fb^{-1} of pp collisions at $\sqrt{s} = 7$ TeV.

3.2 The ATLAS Detector

The ATLAS detector is a multipurpose detector which is designed and optimized for a large physics program. The ATLAS collaboration consists of over 3000 physicists from 174 institutions in 38 different countries. ATLAS has been in stable data taking mode since 2010. A cut-away view of its layout, showing the individual components, is show in Figure 3.3.
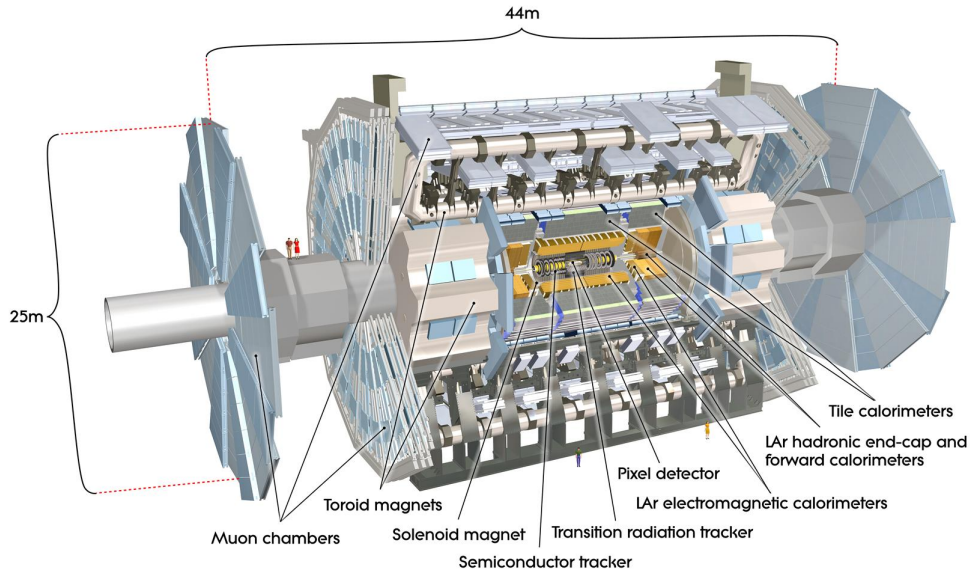
Figure 3.3: Schematic View of the ATLAS detector. ATLAS Experiment ©2012 CERN [17].

The design features of the LHC, mainly its high luminosity, and large beam energy, provide the possibility for many physics analyses; particularly, these design features are optimized for processes with low cross-sections and sensitivity to massive particles, compared to past collider experiments. These include the discovery or exclusion of the Standard Model Higgs boson, the search for new physics including new heavy gauge bosons, supersymmetric particles, and new particles predicted from extra dimension models [17]. For example, a relatively clean channel to look for the Higgs with a low mass would be its decay to two photons. For higher mass, a good channel would be the decay to two W/Z bosons, where each W/Z would decay to leptons. These channels require a detector which has an excellent electromagnetic calorimeter with excellent resolution and good photon and electron identification, a muon system with high acceptance, and hadronic calorimeters with large coverage.

In order to take advantage of all of the possible physics available from the LHC, it is important to optimize the design of the detector accordingly. With the high luminosity of the LHC, the detector is required to be fast, and utilize radiation-hard electronics. The collision of proton bunches provides a messy environment which means that the detector must have high granularity. The detector should also have maximal acceptance. Excellent calorimetry, including electromagnetic calorimeters for electron and photon identification and hadronic calorimeters for accurate jet and missing transverse energy measurements is required. The muon system must provide good muon identification, including good momentum resolution and differentiation between oppositely charged muons, specifically for high p_T muons as higher momentum charged particles bend less in magnetic fields compared to lower momentum particles. It is also important that efficient triggers are developed in order to ensure that physics processes of interest are being recorded. The components of the detector relevant to the analysis that will be presented in this thesis are described briefly in the following sections.

3.2.1 ATLAS coordinate system and other conventions

The direction of the incoming beam is defined as the *z*-axis. The *x*-*y* plane is transverse to the *z*-axis with the positive *x* direction pointing from the interaction point to the centre of the LHC ring and the positive *y* direction pointing upwards. The azimuthal angle, ϕ, is

measured around the beam axis. The polar angle, θ, is the angle from the positive *z*-axis.

The pseudorapidity, $\eta = -\ln\tan(\theta/2)$, is a more commonly used parameter related to the polar angle. This parameter is preferentially used over θ since $\Delta\eta$ is Lorentz invariant under boosts along the *z* direction. Analyses at ATLAS are often performed in η-ϕ space, with the distance in η-ϕ space between two particles defined by the variable $\Delta R = \sqrt{\Delta\phi^2 + \Delta\eta^2}$.

3.2.2 The Magnet Systems

Magnet systems are used in particle physics detectors to measure the momentum and electric charge of charged particles which pass through the detector. For a particle with momentum *p* in a homogeneous magnetic field B, the particle will be deflected in a circular trajectory with a bending radius ρ given by:

$$\rho\,[m] = \frac{p\,[GeV/c]}{0.3\,B\,[T]}. \tag{3.2}$$

The ATLAS magnet system consists of four large superconducting magnets: a solenoid, a barrel toroid, and two endcap toroid magnets as shown in Figure 3.4. The central solenoid magnet produces a 2 T magnetic field that is aligned with the beam axis and encapsulates the entire inner detector. The strength of the magnetic field is chosen to provide sufficient bending of high-p_T charged particles in the tracking system. The solenoid has a length of 5.8 m with inner and outer diameters of 2.46 m and 2.56 m, respectively. The central solenoid system is kept at a temperature of 2.7 K.
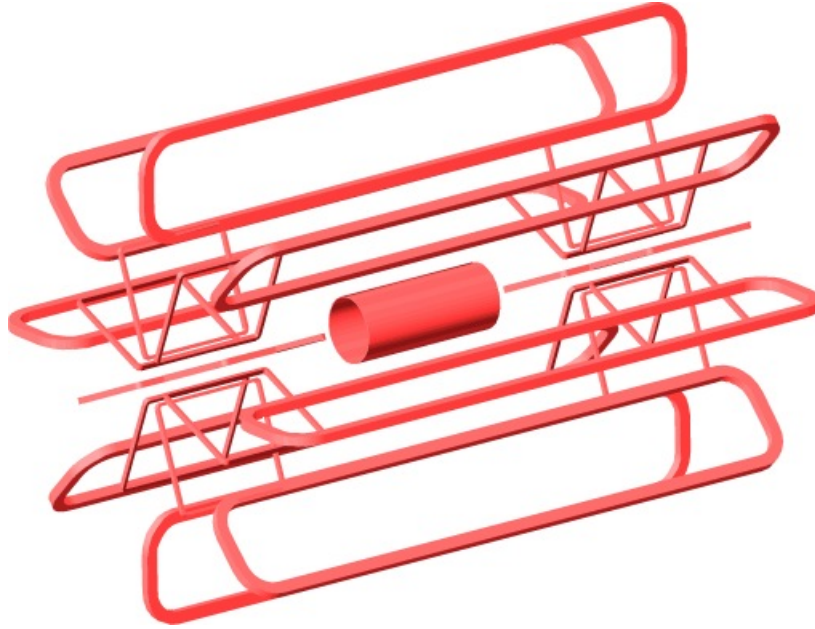
Figure 3.4: The ATLAS magnet system. ATLAS Experiment ©2012 CERN [17].

The magnets outside of the central tracking system are used to provide bending for measurements of muons, because unlike jets, electrons, and photons, muons will traverse through the calorimeter while depositing only a small fraction of their energy [2]. They can therefore be detected and uniquely identified outside of the calorimeters. The barrel toroid provides the magnetic field in the central region. It is made of eight coils surrounding the central solenoid. The entire barrel toroid system is 25.3 m in length with an inner diameter of 9.4 m and an outer diameter of 20.1 m. Each endcap toroid consists of eight square coil units, bolted onto a rigid structure. The entire toroidal magnet system operates at a temperature of 1.9 K.

3.2.3   Inner Detector

The inner detector, as the name suggests, is the detector located nearest to the interaction point (IP) of the colliding proton beams. The purpose of the inner detector is to reconstruct the trajectory of charged particles. This is done by measuring the response of the active material in the detector to the passage of charged particles, typically referred to as "hits", and combining a set of hits that form a track. Information about primary and secondary

vertices, defined by the position(s) where tracks converge, and the momentum of particles produced in the collision is obtained from measurements in the inner detector. A cut-away of the inner detector is shown in Figure 3.5.
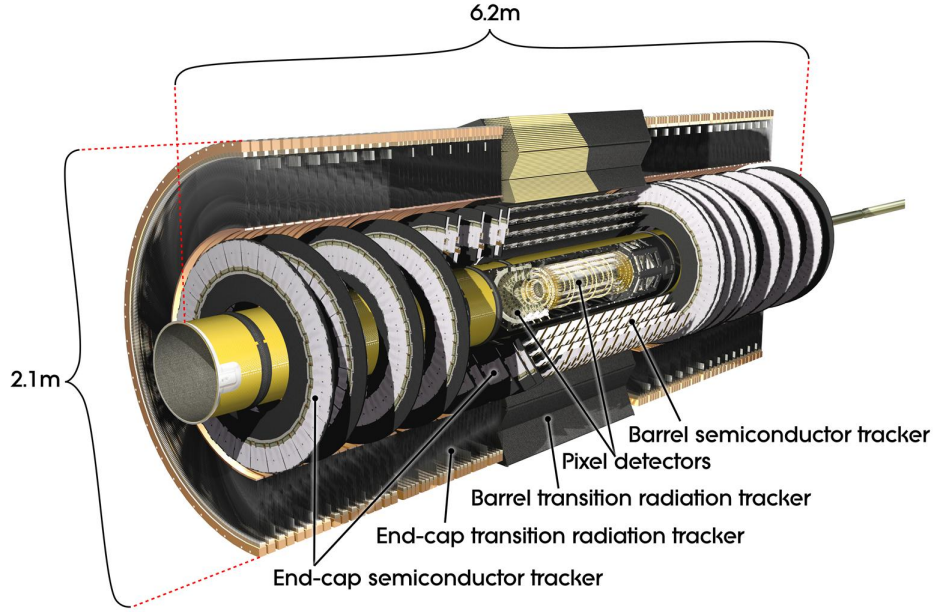
Figure 3.5: Schematic View of the ATLAS inner detector. ATLAS Experiment ©2012 CERN [17].

The inner detector is a tracking system consisting of 3 layers: a cylindrical silicon-pixel (PIXEL) detector nearest the interaction point, which is surrounded by a silicon tracker (SCT) barrel, and further surrounded by a Transition Radiation Tracker (TRT). The PIXEL detector surrounds the beam pipe, whereas both the SCT and TRT have barrel and endcap components.

The PIXEL and SCT detectors are semiconductor detectors. In semiconductors, a signal is obtained when a charged particle traverses the detector and produces electron-hole pairs. The TRT detector consists of gaseous straw tubes, interweaved with transition radiation material. Tracking is obtained by ionization of the gas in the drift tubes. The transition radiation provides electron identification and electron/pion discrimination.

This detector provides excellent coverage in the pseudorapidity range $\eta < 2.5$ and for charged particles above a p_T threshold of 0.5 GeV. It also provides electron identification in

the region $\eta < 2.0$ with energies between 0.5 GeV and 150 GeV. The entire system extends from a radius of 50.5 mm from the intersection of the proton bunches out to a radius of 1150 mm with length $\pm$ 3512 mm in the z direction from the interaction point.

3.2.4 Calorimeters

The calorimeters are destructive detectors, used to obtain energy measurements of particles by stopping them. A cut-away of the ATLAS calorimeter system is shown in Figure 3.6.
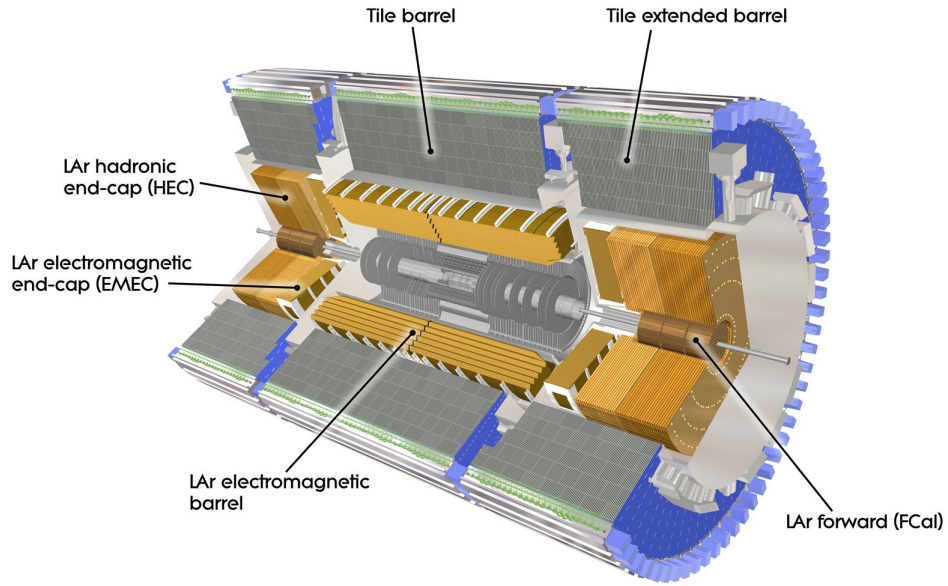
Figure 3.6: Schematic View of the ATLAS calorimeters. ATLAS Experiment ©2012 CERN [17].

The electromagnetic (EM) calorimeter is designed to measure the energy of electrons and photons via their electromagnetic interaction with the active detection media in the calorimeter. Particularly, the primary energy loss mechanism of high energy electrons and positrons is Bremsstrahlung. The photons produced from Bremsstrahlung will then convert into an electron-positron pair; this is referred to as pair production. This process, known as electromagnetic showering, continues until the energy of the electrons and photons do not

have enough energy to Bremsstrahlung and pair produce, respectively. Finally, the electrons will lose the remainder of their energy via ionization while photons will lose their energy via scattering until they are completely absorbed by the calorimeter. The barrel and endcap EM calorimeters are made of lead and liquid argon (LAr), providing coverage of $|\eta| < 1.475$ and between $1.375 < |\eta| < 3.2$, respectively. The lead plates are used to initiate electromagnetic showers and to absorb the energy of the electrons and photons. These plates are separated by layers of active material consisting of LAr which is used to sample the energy between each layer. This type of sampling calorimeter provides energy measurements and information on shower development. The EM calorimeter also includes a presampler, which uses LAr as the active material, and is used to correct for the energy loss of the electrons and photons before they reach the calorimeter. The presampler provides coverage in the region $\eta < 1.8$. In order to obtain reliable energy measurements, the detector must be thick enough to absorb all of a particles' energy, hence stopping the particle itself. The total thickness of the EM barrel (endcap) calorimeter is $>22(24)$ radiation lengths (X_0), where the radiation length is defined as the distance that it takes for a particle to lose $1/e$ of its initial energy.

The hadronic calorimeter (HCAL) is also a fully destructive calorimeter and it surrounds the EM calorimeter in order to detect hadrons since they do not deposit all of their energy in the EM calorimeter. The barrel calorimeter is a scintillating tile calorimeter, covering the region $|\eta| < 1.0$ and an extended tile calorimeter covering $2.5 < |\eta| < 3.2$, with radial extension from 2.28 m to 4.25 m. These scintillating sheets produce photons which are detected by photomultiplier tubes. The hadronic endcap calorimeter is a copper-LAr sampling calorimeter that provides coverage in the range $1.5 < |\eta| < 3.2$. The thickness of the calorimeter is given in interaction lengths (λ), defined as the mean free path length required to reduce the energy of relativistic charged particles to $1/e$ of its initial energy. The thickness of each layer in the barrel (endcap) is 1.5 (1.5), 4.1 (2.6), and 1.8 (3.3) λ.

The forward calorimeters (FCALs) provide coverage in over $3.1 < |\eta| < 4.9$. There are three FCAL detectors; one electromagnetic compartment (FCAL1) and two hadronic compartments (FCAL2 and FCAL3). Each FCAL uses LAr as the active medium while FCAL1 uses copper as its absorber and FCAL2 and FCAL3 use tungsten as the absorber. The design of the FCAL system is optimized for the high flux of particle in the high $|\eta|$ region.

3.2.5   Muon System

Since energy loss via Bremsstrahlung is proportional to m^{-4}, low energy muons do not lose a significant fraction of their energy via Bremsstrahlung but rather by ionization. As a result, muons only deposit a small fraction of their energy in the calorimeters and a separate detection system outside of the calorimeters is built to identify them and measure their momentum. Muons are deflected by the magnetic fields from the toroidal magnet system. There are three layers to the muon system. Over most of the pseudorapidity range Monitored Drift Tubes (MDT's) are used. In the range $2 < |\eta| < 2.7$, Cathode Strip Chambers (CSC's) are used. CSC's are multiwire proportional chambers with spaced cathode strips.

The trigger system for the muon spectrometer consists of Resistive Plate Chambers (RPC's) in the barrel and Thin Gap Chambers (TGC's) in the end caps. The trigger covers a pseudorapidity range of $|\eta| < 2.4$. The combined muon system is shown in Figure 3.7.
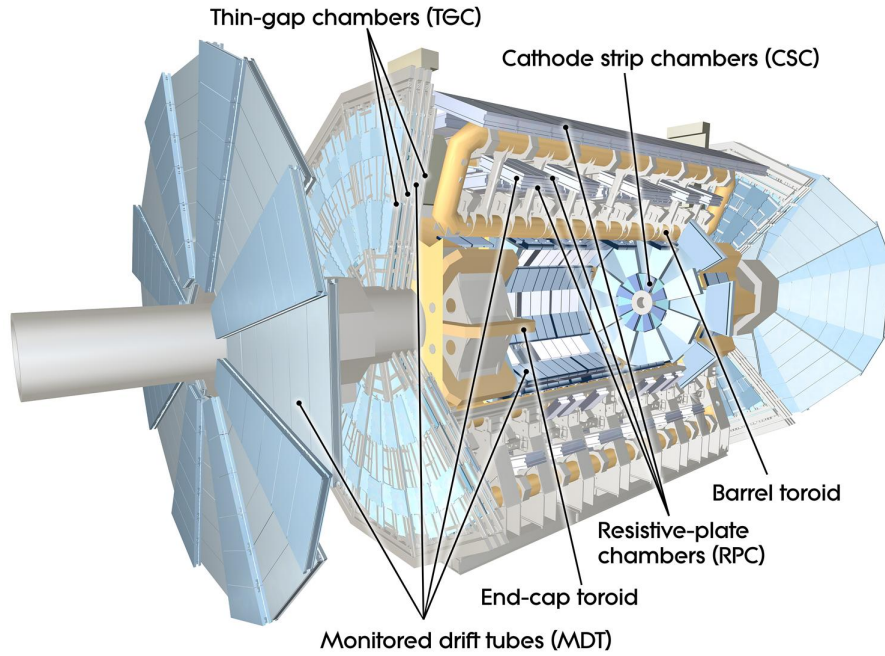
Figure 3.7: The ATLAS muon system. ATLAS Experiment ©2012 CERN [17].

3.2.6 ATLAS Triggers

With bunches colliding every 50 ns, the readout systems are unable to write out all the data and as such only a subset of the data is recorded. A set of what are called 'triggers' is used, which looks for characteristic signals, and decide whether an event should or should not be recorded. The triggers reduce the rate of the colliding bunches from 20 MHz to a manageable rate of at most 400 Hz. There are three levels to the trigger system used at ATLAS: Level 1 (L1), Level 2 (L2), and the Event Filter (EF). The L1 trigger is a hardware-based trigger which uses only a subset of the information available to reduce the rate to 100 KHz. This decision is based on the multiplicity and energy of physics objects and uses information from the calorimeters and muon systems. The L2 trigger further reduces the rate to approximately 1 KHz. This trigger refines the selection using the full granularity of all the detector subsystems. Finally, the EF trigger, also a software-based trigger, is designed to reduce the rate to 400 Hz. This trigger uses offline physics and event reconstruction algorithms.

Chapter 4

Event and Object Selection in $t\bar{t}$ Events

This analysis involves a search for the lightest Kaluza-Klein excitation of the gluon, specifically focusing on the decay of the KK-gluon to top-antitop quark ($t\bar{t}$) pairs. Top quarks decay almost exclusively to a *W* boson and a *b* quark. Each *W* can then decay to either a quark-antiquark pair or to a charged lepton-neutrino pair. The $t\bar{t}$ decay channels are shown below in Figure 4.1.

Top Pair Decay Channels

$\bar{c}s$	electron+jets	muon+jets	tau+jets	all-hadronic	
$\bar{u}d$					
$\bar{\tau}$	$e\tau$	$\mu\tau$	$\tau\tau$	tau+jets	
$\bar{\mu}$	$e\mu$	$\mu\mu$	$\mu\tau$	muon+jets	
$\bar{e}$	ee	$e\mu$	$e\tau$	electron+jets	
W decay	e^+	μ^+	τ^+	$u\bar{d}$	$c\bar{s}$

Figure 4.1: Chart of possible top pair decay channels [18].

25

With two W bosons in the event, there are three main channels for this system: either both W's decay to quark-antiquark pairs (all-hadronic), one quark-antiquark pair and one charged lepton-neutrino pair (semileptonic), or both W bosons decay to a charged lepton-neutrino pair (dileptonic). This analysis is performed in the dilepton channel. The Feynman diagram for this process is shown in Figure 4.2. Although the dilepton channel suffers from a smaller branching fraction relative to all others, and consequently a smaller fraction of the total $t\bar{t}$ events, this channel has its own advantages that motivate a search. For instance, by choosing this channel, the large fraction of QCD background events produced at the LHC is eliminated in comparison to the all-hadronic and semileptonic channels. This is favourable because signals with low cross sections can become buried in the large QCD multijet background, which are difficult to model; in comparison, the dilepton channel features fewer background processes which may contaminate signal events. This means that after event and object selection, the remaining candidate sample consists predominantly of top-antitop quark pairs. All backgrounds to these events are discussed in Section 4.2.
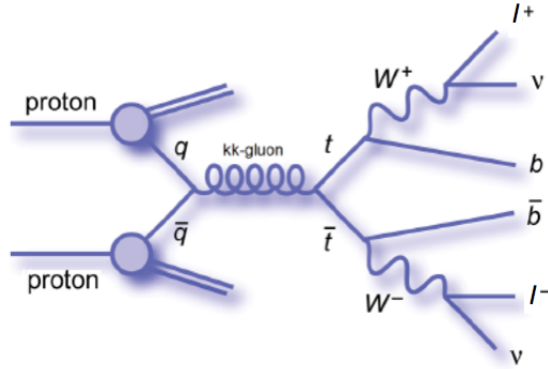
Figure 4.2: KK-gluon Feynman diagram at leading order in the dilepton channel [18].

4.1 Object Reconstruction

To enhance potential signal events, selection criteria which reduce the background, while keeping signal events, must be established. The object and event selection used in this analysis follow the choices suggested by the $t\bar{t}$ dilepton cross-section measurement group

at ATLAS. The reconstructed physics objects of interest for this analysis include electrons, muons, jets and the missing transverse momentum which is taken to infer the presence of undetected neutrinos.

Since electrons undergo electromagnetic showers in the calorimeter, electron candidates are defined as clusters of calorimeter cells corresponding to this electromagnetic shower. Electron candidates are required to fit the definition of a 'tight' electron [19]. In addition, the electron cluster candidate is required to have $p_T > 20$ GeV and to be within the pseudo-rapidity region $|\eta_{cluster}| < 2.47$, excluding a crack region of the detector between the barrel and endcap calorimeters in the region of $1.37 < |\eta_{cluster}| < 1.52$.

Muon candidates are reconstructed using the MuID algorithm [17]. This algorithm searches for track segments in the muon chambers and matches these tracks to an inner detector track. The tracks from the inner detector and the muon chambers are then refit to form a single track. This is referred to as a combined muon. Each muon candidate is required to have a $p_T > 20$ GeV and be within $|\eta| < 2.5$.

Jet candidates are reconstructed using an anti-k_t algorithm with radius parameter $R = 0.4$ [20]. They must have a $p_T > 20$ GeV and be within the region $|\eta_{cluster}| < 2.5$.

In order to remove events where leptons originate from the semileptonic decay of heavy quarks inside a jet, the leptons in the event are required to be isolated. For electrons, this isolation criterion requires the energy deposition in a cone of R = 0.2, with the cluster energy of the electron removed, to be less than 3.5 GeV. Similarly, for muons, the energy deposition in a cone of R = 0.3, with the muon energy removed, has to be less than 4.0 GeV. Furthermore, if a jet candidate is within a distance of $\Delta R < 0.2$ of an electron candidate, the jet candidate is removed so that the electron is not double counted as a jet. For muons, candidates are removed if they are within a distance of $\Delta R < 0.4$ of a jet candidate.

4.2 Backgrounds

The main irreducible background to any $t\bar{t}$ resonance will be the Standard Model $t\bar{t}$ production since the final states are identical. The second largest background comes from the Drell-Yan process, $Z/\gamma* \to \ell^+\ell^-$, produced with jets and large E_T^{miss} which may arise from jet mis-measurement. This background is referred to as Z + jets. The next largest background comes from events containing reconstructed objects that are misidentified as

leptons, such as *W* events produced with jets, where a jet is misidentified as a lepton or a jet decays semi-leptonically. These misidentified objects are referred to as 'fakes'. The contributions of Drell-Yan and fakes are determined from data [21]. A small fraction of background events is also obtained from single top production. Another small source of background events comes from the diboson (WW, ZZ, and WZ) production processes. The contributions from single top quark productions and dibosons are relatively small and are determined from Monte Carlo simulations.

4.3 Event Selection

First, the candidate event in the analysis must be triggered by either a single muon or single electron with $E_T > 15$ GeV. Each event must contain at least two leptons which pass the object selection described in section 4.1. One of these leptons must be matched to the trigger lepton for the event. If the event is considered to be a di-electron (di-muon) event, it must match the electron (muon) trigger lepton. If the event is an event with both an electron and muon, either trigger may have fired for the event to pass this selection. The trigger lepton must be matched to the reconstructed electron or muon within a distance of $\Delta R < 0.15$. Events are required to have at least five tracks associated with the primary vertex. Since there are two neutrinos in the event that do not interact with the detector, they are not directly measured, but lead to large E_T^{miss}. In the *ee* and *μμ* channels, the event is rejected if the E_T^{miss} is less than 40 GeV, in order to remove *Z* + jets background where no missing energy is expected, since there are no neutrinos present, but may originate from mismeasurements. For the *eμ* channel, a requirement of $H_T = \sum p_T^{leptons} + \sum p_T^{jets} > 130$ GeV (sum over all jet and lepton candidates) is placed in order to reduce contamination coming from the diboson background. In the *ee* and *μμ* channel, a cut on the invariant mass of the two leptons of $|m_{\ell\ell} - m_Z| > 10$ GeV is placed in order to remove events from Z+jets background. With all of the above selections applied, there must only be two leptons in the event and they are required to have opposite electric charges.

4.4   Event simulation

In order to validate the theoretical predictions of any model, these predictions need to be compared to observed data. In this case, predictions made from Standard Model or other theories Beyond the Standard Model must be compared to data obtained from ATLAS detector measurements.

At ATLAS, physics collisions and the time evolution of the colliding system and the detector response are simulated. Collectively, these simulations are referred to as Monte Carlo (MC) event simulations. The response of the particles in the ATLAS detector are simulated using the GEANT4 [22] program, whereas the pp collisions are simulated using a variety of MC event generators.

For this analysis, MC samples for all of the backgrounds described in section 4.2 have been generated. The MC samples used are those defined by the ATLAS Top Working Group, given in the Top Working Group Monte Carlo TWiki [23]. The irreducible Standard Model $t\bar{t}$ and the Single Top backgrounds are generated using the MC@NLO [24] event generator. The SM $t\bar{t}$ sample also uses HERWIG [25] to model parton showering and hadronization, the evolution mechanism from parton to jet, and JIMMY [26] to model the underlying event, processes in the event other than the hard scattering components. The Z + jets production and diboson backgrounds are generated using the ALPGEN [27] event generator. The KK-gluon signal sample is generated with MADGRAPH [28] for the hard interaction and PYTHIA [29] is used for parton showers.

Since the mass of the KK-gluon is unknown, a flexible MC re-weighting scheme has been employed. Rather than producing many independent samples with different masses, a single MC sample is used such that a large mass range can be studied with one MC sample. In order for this to be done, the functional form of the Breit-Wigner distribution can be exploited. The relativistic Breit-Wigner function gives the scattering amplitude of processes which form an unstable resonance that subsequently decays. This distribution is given by:

$$f(E) \propto \frac{1}{p^2 - M^2 + iM\Gamma},$$
(4.1)

where p, M, and Γ are the four-momentum, mass, and width of the resonant particle [30]. As such, the cross-section is proportional to the square of 4.1, giving:

$$\sigma \propto \frac{1}{(p^2 - M^2)^2 + M^2\Gamma^2}. \qquad (4.2)$$

For dedicated (single mass) MC samples, the appropriate Breit-Wigner distribution for a resonance of mass M with its corresponding width is fixed to generate the MC sample. In order to create a more flexible MC sample, a Breit-Wigner with arbitrary mass and width, taken to be large in order to cover a large mass range, is generated. This is referred to as a "quasi-flat" in mass sample. From this, in order to obtain the distribution for a single mass of interest (referred to as target mass), the sample is re-weighted by giving each event, i, a weight w_i. This is done by taking the ratio of the Breit-Wigner function with mass and width used to generate the sample to the Breit-Wigner of the target mass and corresponding width. This provides a weight for each event given by:

$$w_i = \frac{f(E)_t^2}{f(E)_{qf}^2} = \frac{(M_{event}^2 - M_{qf,pole}^2)^2 + M_{qf,pole}^2\Gamma_{qf}^2}{(M_{event}^2 - M_{t,pole}^2)^2 + M_{t,pole}^2\Gamma_t^2}, \qquad (4.3)$$

where $t(qf)$ denotes the target (quasi-flat) mass, M_{pole} is the pole mass, Γ is the width of a particle of mass M, and $M_{event} = \sqrt{(p_{\ell^-} + p_{\ell^+} + p_\nu + p_{\bar\nu} + p_b + p_{\bar b})^2}$ is the kinematic mass.

The invariant mass distribution using this re-weighting technique is shown in Figure 4.3 for a KK-gluon with invariant masses ranging from 500 GeV (black) to 1.4 TeV (purple), in 50 GeV mass increments.
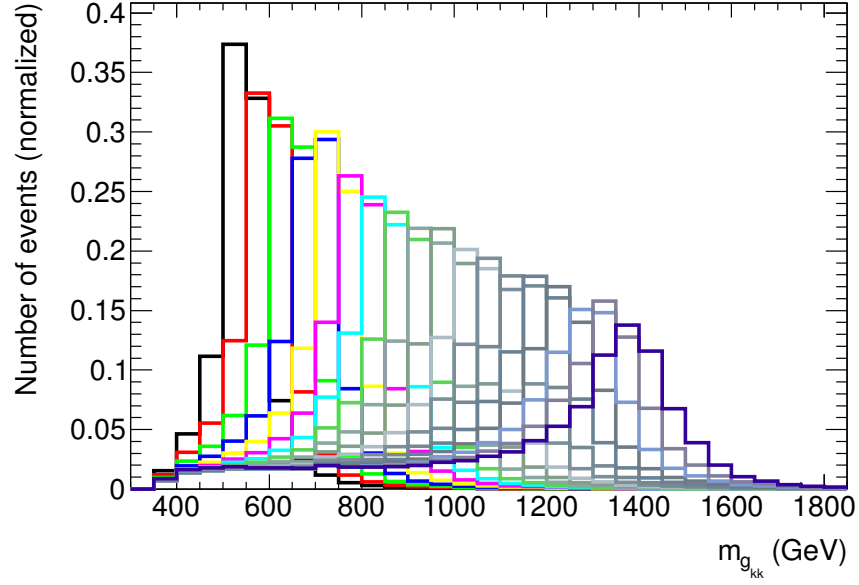
Figure 4.3: Re-weighted KK-gluon invariant mass distribution ranging from 500 GeV (black) to 1.4 TeV (purple) in 50 GeV mass increments obtained by reweighting the KK-gluon quasi-flat MC sample without detector simulations.

4.5 Kinematics and Discriminating Variable

The p_T and η distributions of the charged leptons and jets from the decay of a 1 TeV KK-gluon, after event and object selections, are given in Figure 4.4 and 4.5, respectively. The distributions with and without the simulated detector response are included.

(a) Charged lepton p_T.

(b) Jet p_T of two leading jets.
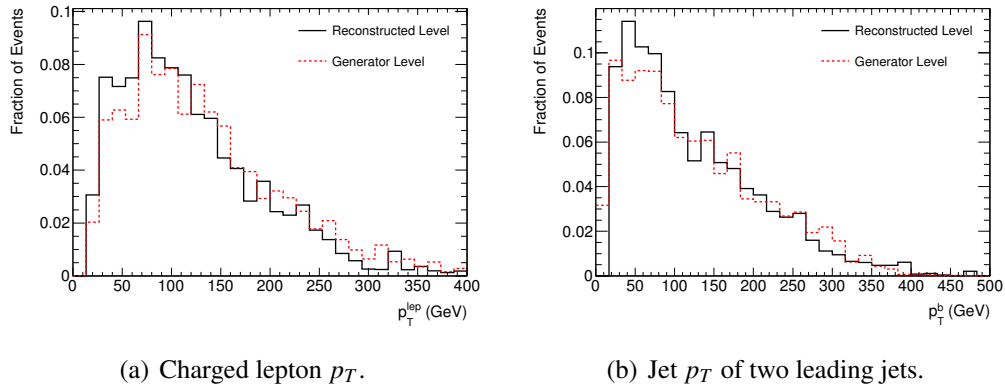
Figure 4.4: p_T distributions of charged leptons and of the two leading jets. The dashed (solid) distributions represent the particles simulated with (without) detector response.

(a) Charged lepton η (*μμ* channel).

(b) Charged lepton η (*ee* channel).

(c) Charged lepton η (*eμ* channel).

(d) Jet η of truth matched jets (all channels).
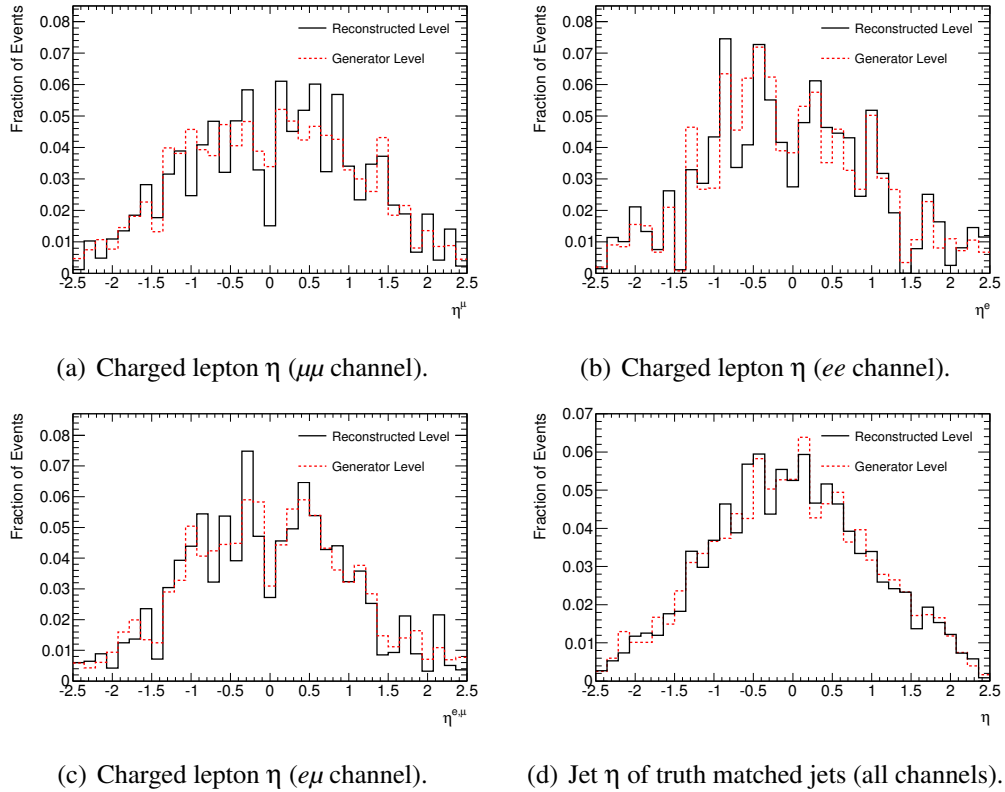
Figure 4.5: Pseudorapidity distributions of charged leptons and of the two truth matched (to *b*) jets. The dashed (solid) distributions represent the particles simulated with (without) detector response.

Since the final state in the dilepton channel contains two neutrinos, the invariant mass of a $t\bar{t}$ resonance cannot be reconstructed from its final state particles as the neutrinos traverse the detector without interacting and thus without being detected. The strategy for searching for such a resonance is to use a discriminating variable that is well-defined and which would, optimally, distinguish from background events. Because the invariant mass is not readily accessible, the discriminating variable used in such an analysis is the effective mass, defined as $H_T + E_T^{miss}$, where H_T is the scalar sum of the p_T of the two leading jets and the two leptons in the event. This distribution for corresponding KK-gluon masses from Figure 4.3 is shown in Figure 4.6. These results are obtained from MC and correspond to KK-gluons in a mass range of 500 GeV (purple) to 1.4 TeV (yellow) in 50 GeV mass increments. In Figure 4.7, the correlation between the effective mass and the $t\bar{t}$ invariant mass is shown.
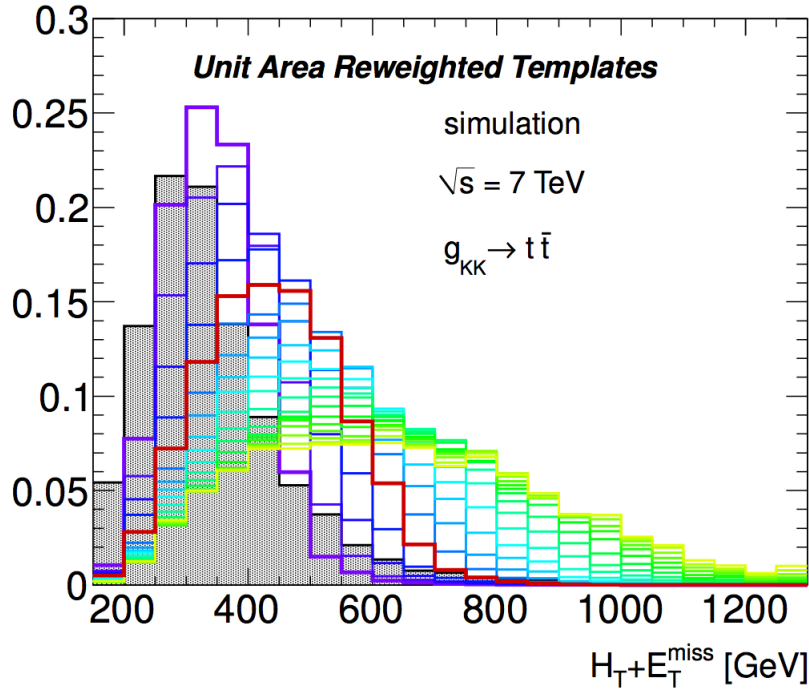
Figure 4.6: $H_T + E_T^{miss}$ for different KK-gluon masses ranging from 500 GeV (purple) to 1.4 TeV (yellow) in 50 GeV mass increments.
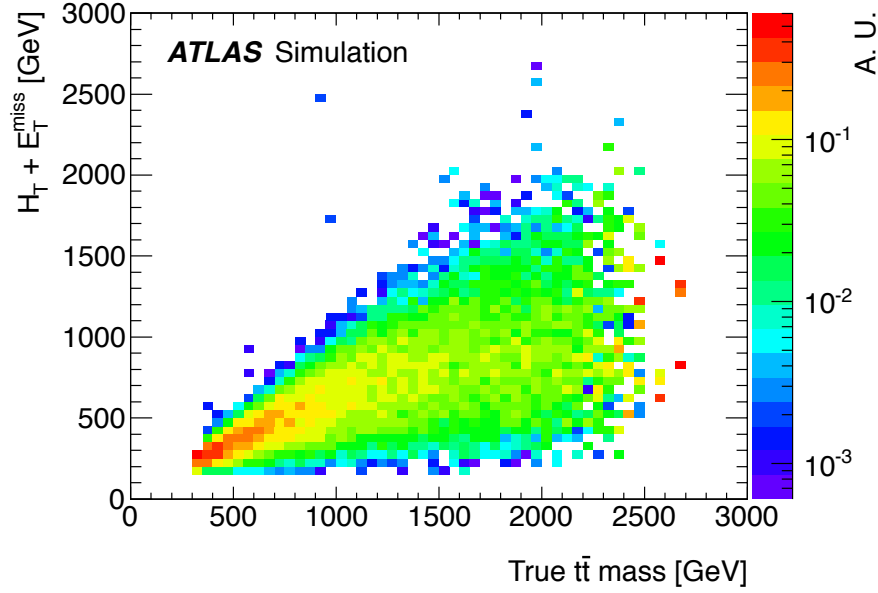
Figure 4.7: Plot of correlation between the effective mass and the true $t\bar{t}$ invariant mass of a KK-gluon [21].

The invariant mass at generator level for the KK-gluon for different masses is shown in Figure 4.3. In comparison to Figure 4.6, the peak of the invariant mass has a noticeable shift for increasing KK-gluon resonance masses. As the mass increases, however, there is an enhancement in the parton luminosity tail which develops as a result of the $q\bar{q}$ production mechanism considered for this model since the parton distribution functions (PDFs) for anti-quarks peak towards small fractions of the protons momentum (x). For low x values, an off-shell mass KK-gluon can be produced, which is distinctly seen in Figure 4.3.

The first result of the $t\bar{t}$ resonant analysis using the $H_T + E_T^{miss}$ variable is shown in Figure 4.8 [21]. This result uses $\mathcal{L} = 2.05$ fb^{-1} of proton-proton collisions recorded by ATLAS at a center of mass energy of 7 TeV Using this observable, the current lower limit on the KK-gluon mass is 1.08 TeV at 95% C.L. and is shown in Figure 4.9.
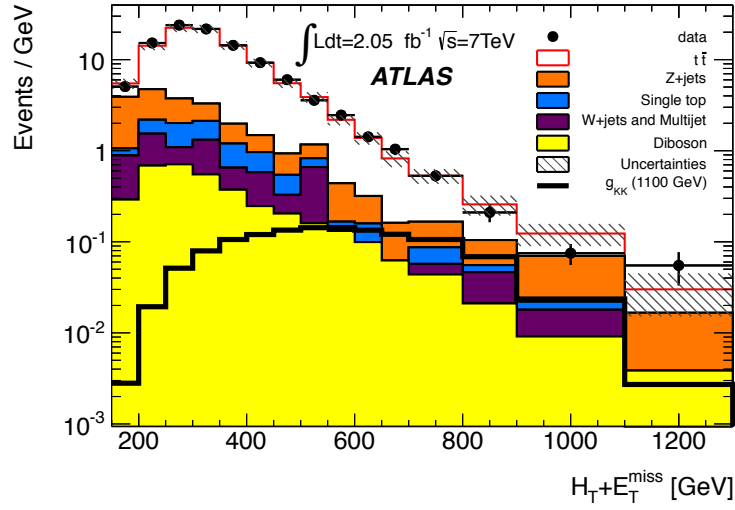
Figure 4.8: $H_T + E_T^{miss}$ distribution after event selection for significant backgrounds and hypothetical 1.1 TeV KK-gluon [21].
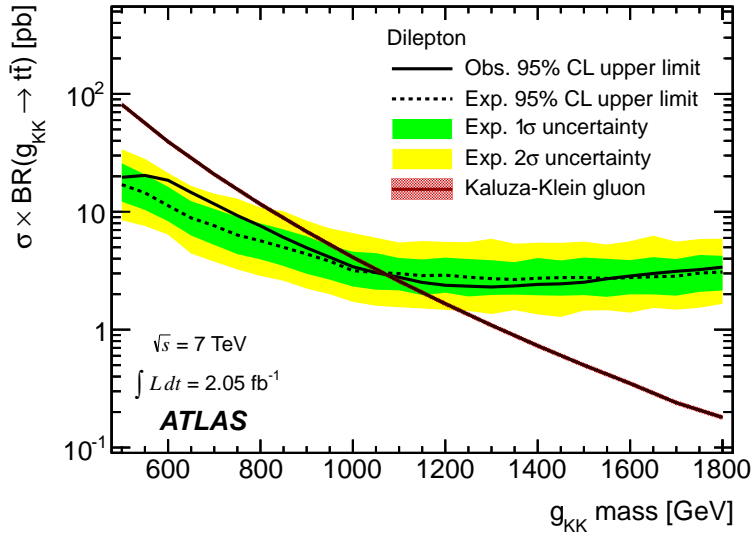
Figure 4.9: Expected and observed upper limit on KK-gluon cross section using 2.05 fb^{-1} of data as a function of KK-gluon mass [21].

4.5.1 Boosted Top Quarks

The decay of high mass resonances will produce high-p_T top quarks: the heavier the resonance particle, the higher the p_T of the top quarks. This is demonstrated in Figure 4.10 where the transverse momentum distribution is shown for a KK-gluon with mass between 500 GeV and 1.4 TeV. There is still a large subset of events which have lower p_T for higher mass resonance, originating primarily from the low mass parton luminosity tail, as seen in Figure 4.3.
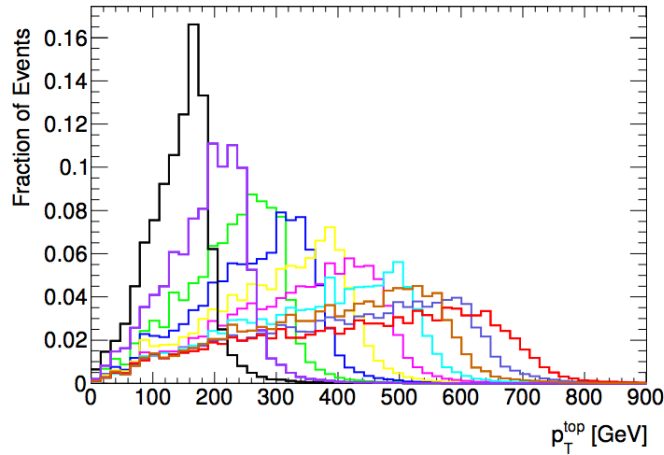
Figure 4.10: Top transverse momentum distributions originating from KK-gluon resonances of 500 GeV (black) to 1.4 TeV (red) in 100 GeV mass increments.

The decay products of high-p_T top quarks become collimated, meaning that final state particles may no longer be completely isolated from one another. The decay products from such decays often fall within a wider cone distribution of $\Delta R < 1$, in comparison to standard light-quark jets commonly defined with a cone size of $\Delta R < 0.4$ [31]. The separation between final state particles originating from the top quark decay is shown in Figure 4.11. A clear decrease in angular separation between the final state particles is observed for increasing KK-gluon resonance mass.

The p_T distributions of top quarks decaying from a 1 TeV KK-gluon are compared to the decay of the Standard Model $t\bar{t}$ events in Figure 4.12. A red line is placed at p_T= 350 GeV (approximately twice the rest mass of the top quark) which provides an approximate p_T region where top quarks become boosted. This is where the mean distribution

(a) $\Delta R(b,\ell)$

(b) Mean $\Delta R(b,\ell)$
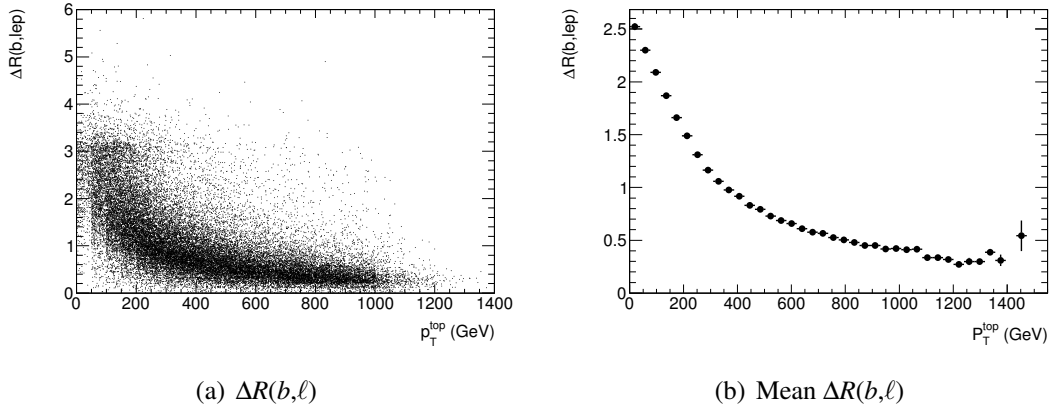
Figure 4.11: Scatter plot (left) and mean plot (right) of ΔR distance between a b quark and a lepton originating from the decay of a top quark as function of the top quark's transverse momentum.

of top quark decay products falls within the definition of a 'fat' jet ($\Delta R < 1$). For a 1 TeV KK-Gluon, 52% top quarks are considered boosted, which is significant compared to the Standard Model $t\bar{t}$ top quark distribution where only a very small fraction of top quarks with $p_T > 350$ GeV are expected in the tail of the p_T distribution.

(a) Standard Model $t\bar{t}$.
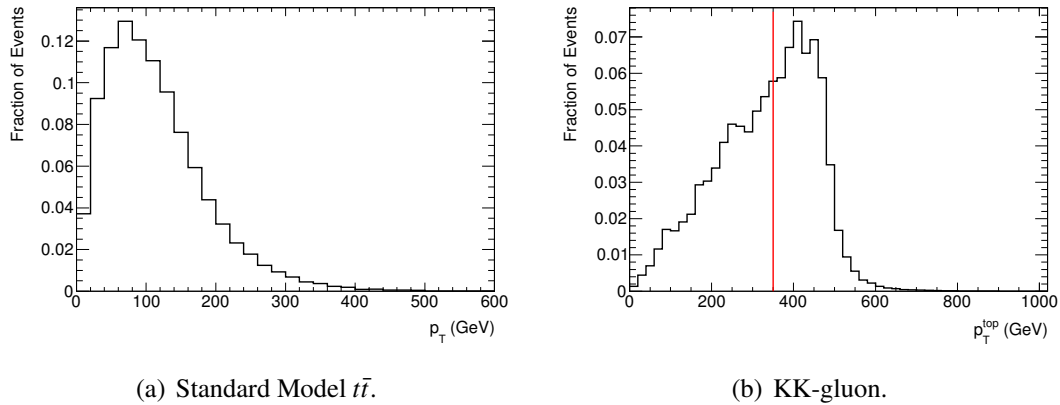
(b) KK-gluon.

Figure 4.12: Top quark p_T distribution in (a) Standard Model $t\bar{t}$ MC sample and (b) 1 TeV KK-gluon MC sample. A line is placed at 350 GeV to illustrate the fraction of events in which decay products fall within a cone of $\Delta R < 1$.

The standard selection cuts described in section 4.1 are not optimal for signal events containing these boosted tops since these selection criteria are optimized for Standard Model $t\bar{t}$ events. This results in a loss of signal events due to the object isolation requirements. Figure 4.14 shows the acceptance for the KK-gluon using selection criteria described in section 4.1 and 4.3 as a function of the KK-gluon mass. These cuts are referred to as 'standard cuts'.

The first isolation cut that is removed is the lepton isolation requirement. This requires the lepton cluster energy inside a cone of $R = 0.2$ ($R = 0.3$) with the lepton energy removed to be less than 3.5 GeV (4.0 GeV) for electrons (muons). The removal of this selection criteria is referred to as 'no isolation'. Finally, both electron and muon jet overlap cuts are completely removed. The event acceptance efficiency for each isolation criterion is given in Figure 4.13 and 4.14 for separate channels (*ee*, $\mu\mu$ and $e\mu$) and combined channels, respectively. By comparing the circle and star marker distributions in Figure 4.14, there is a clear gain in event acceptance resulting from the removal of standard isolation and overlap criteria, especially in the muon channel. The gain of signal efficiency with removal of isolation cuts relative to the signal efficiency with standard isolation cuts is given in Figure 4.15, showing a large gain in efficiency, mainly for events with $m_{g_{KK}} > 1$ TeV.

(a) *ee*

(b) *μμ*

(c) *eμ*
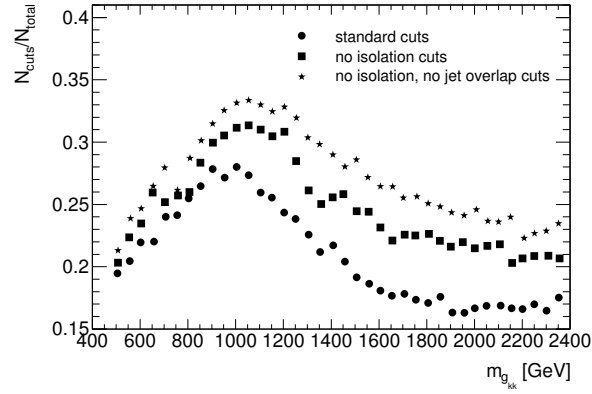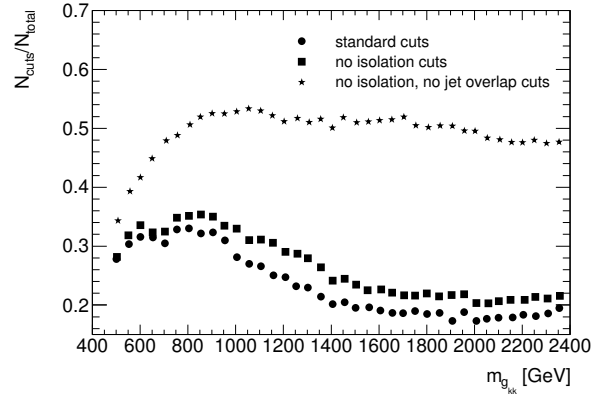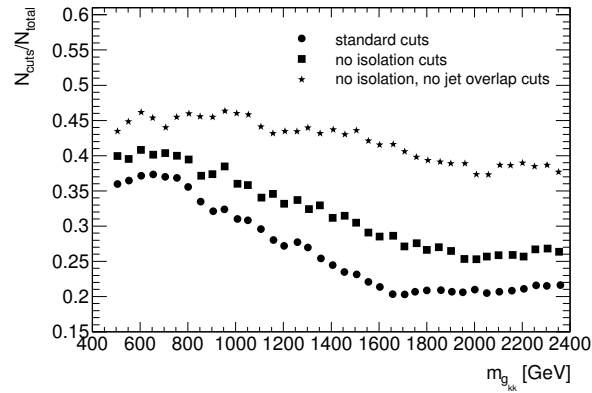
Figure 4.13: Event acceptance for different isolation criteria for $t\bar{t}$ dilepton events for all channels. The circle, square, triangle, and star markers show the acceptance using the standard cuts, lepton isolation removal, and removal of all isolation and jet overlap requirements, respectively, relative to the total number of events (N_{total}) before selection cuts.
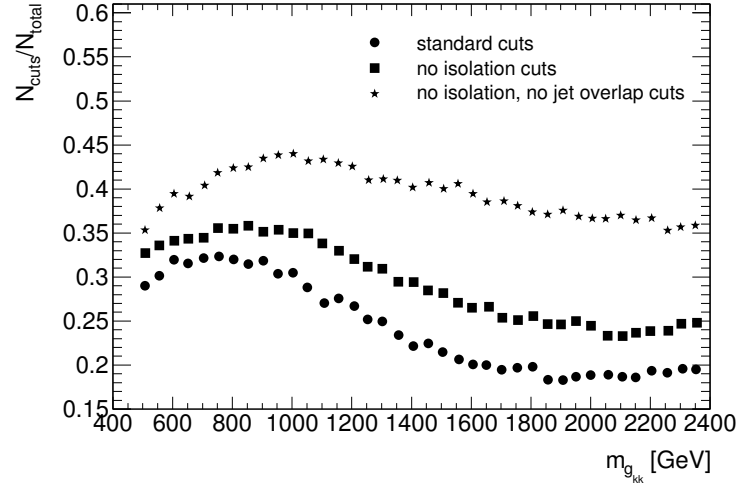
Figure 4.14: Event acceptance for different isolation criteria for $t\bar{t}$ dilepton events. The circle, square, triangle, and star markers show the acceptance using the standard cuts, isolation removal, and removal of all isolation and jet overlap, respectively, relative to the total number of events (N_{total}) before selection cuts.
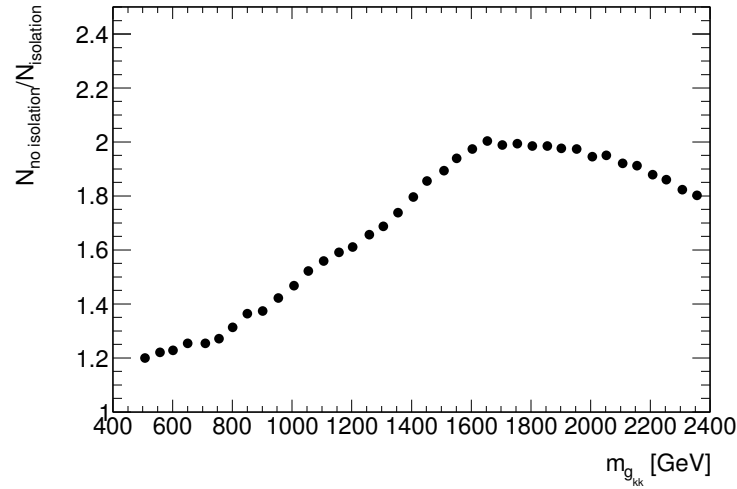
Figure 4.15: Acceptance gain due to isolation removal relative to standard selection for different KK-gluon masses.

The number of events that pass all selection criteria, with varying isolation criteria for

a 1 TeV KK-gluon is given in Table 4.1. Clearly, by loosening isolation selection criteria more events will pass event selection. Since these cuts should be implemented taking into account the signal to background ratio, the effect on the background must also be investigated. To ensure that removing isolation requirements optimizes signal to background significance, the number of events passing event selection for background events is given in Table 4.2. From these numbers, it can be seen that the fraction of events gained by implementing the standard isolation cuts has a larger effect on signal compared to the background processes.

Table 4.1: Total number of events passing all event selection for different object isolation criteria for a 1 TeV KK-gluon. The gain is relative to standard isolation criteria.

Implemented Isolation	Number of Events	Gain Factor
Standard Isolation	361402	1.00
No isolation, $\Delta R(\mu^{\pm}, jet) = 0.4$	424807	1.18
No isolation, no overlap cuts	509286	1.41

Table 4.2: Relative acceptance of background events for removed lepton isolation criteria.

	SM $t\bar{t}$	Z + jets	Diboson	Single Top	Signal
$\frac{N_{no\ isolation}}{N_{isolation}}$	1.22	1.24	1.13	1.14	1.41

Loosening isolation cuts on objects identified as electrons and muons, however, increases the possibility of accepting jets which are falsely reconstructed as a lepton. These are referred to as fakes. For this analysis, a liberal approach in which no isolation and no overlap cuts are implemented is taken. The effects and optimization on the background contribution from fakes are beyond the scope of this thesis and are considered in a PhD thesis in parallel.

Chapter 5

Mass Reconstruction

5.1 Analytic Solutions

The invariant mass, m, of a particle that decays to i particles is given by:

$$m = \sqrt{(\sum_i E_i)^2 - (\sum_i \vec{p}_i)^2} \tag{5.1}$$

In the dileptonic $t\bar{t}$ decay, there are two neutrinos in the final state. One of the disadvantages of analyses which have neutrinos in their final states is the inability to detect the neutrinos because they do not interact with the detector. The fact that they are not detected means that their four-vectors are unknown and therefore the mass of the parent particle cannot be obtained from equation 5.1 for these types of decays. Instead, the presence of the neutrino is inferred by the missing momentum. From conservation of momentum, the sum of the momentum before and after the collision must be equal. In practice, the missing momentum can only be calculated in the transverse $(x - y)$ plane because the longitudinal momentum of the constituents that collide is unknown. For the purposes of this analysis, E_T^{miss} is attributed to both of the neutrinos, however it is important to realize that the missing energy may arise from another source, such as mismeasurements at the experimental level. The effect of detector resolution, including the resolution of E_T^{miss} will be discussed.

Even though the dileptonic $t\bar{t}$ decay has two neutrinos, and as such the invariant mass is not directly available, this channel does provide enough kinematic constraints which

can be used to analytically reconstruct possible four-vector neutrino solutions. Assuming E_T^{miss} originates solely from the neutrinos, the relevant kinematics for neutrino four-vector reconstruction in the dilepton channel can be represented by the following set of eight equations:

$$
\begin{aligned}
\displaystyle{\not{E}_x} &= p_{\nu_x} + p_{\bar{\nu}_x} \\
\displaystyle{\not{E}_y} &= p_{\nu_y} + p_{\bar{\nu}_y} \\
E_\nu^2 &= p_{\nu_x}^2 + p_{\nu_y}^2 + p_{\nu_z}^2 \rightarrow p_\nu^2 = 0 \\
E_{\bar{\nu}}^2 &= p_{\bar{\nu}_x}^2 + p_{\bar{\nu}_y}^2 + p_{\bar{\nu}_z}^2 \rightarrow p_{\bar{\nu}}^2 = 0 \\
m_{W^+}^2 &= (p_{l^+} + p_\nu)^2 \\
m_{W^-}^2 &= (p_{l^-} + p_{\bar{\nu}})^2 \\
m_t^2 &= (p_{l^+} + p_\nu + p_b)^2 \\
m_{\bar{t}}^2 &= (p_{l^-} + p_{\bar{\nu}} + p_{\bar{b}})^2 .
\end{aligned}
\tag{5.2}
$$

From ATLAS data, the missing transverse energy along with the four-vectors of the leptons and jets can be reconstructed. The on-shell mass of the top quark and W boson is also known and used as constraints, along with the assumption that the neutrinos are approximately massless. The system of equations given in 5.2 reduces to a quartic equation with coefficients provided in the appendix of reference [32, 33]. This results in at most four solutions satisfying the set of equations. However, if any of the neutrino solutions are complex, they are considered unphysical and are rejected.

It is important to note that these constraints do not pertain to the τ branch of the dilepton channel ($W \rightarrow \tau\nu_\tau$) because τ leptons will further decay. If the τ decays leptonically, to $e + \bar{\nu}_e + \nu_\tau$ or $\mu + \bar{\nu}_\mu + \nu_\tau$, the detected final state objects will be identical to the leptonic decay of the W to e or μ. There will, however, be a third neutrino that contributes to the missing energy and the kinematic constraints in equation 5.2 are no longer satisfied. The characterization in this chapter uses generator level particles and only true dilepton events in the e and μ branches are investigated.

5.2 Extracting the Correct Neutrino Solution

When solutions to the kinematic constraints exist, the correct neutrino solution must be extracted from the set of all possible solutions if the correct $t\bar{t}$ invariant mass is to be obtained. In practice, if objects are improperly measured, such that the kinematics do not match correctly to the set of equations 5.2, there may be no neutrino solution set which truly corresponds to the physical neutrinos. Even when there is a correct solution, selecting the solution is not a trivial task. This thesis focuses on methods used to extract correct solutions in order to re-gain the invariant mass of the $t\bar{t}$ system.

5.2.1 Target Mass Approach

One method used to extract the correct neutrino solution for an event is to reconstruct the invariant mass using each neutrino solution set and comparing the invariant mass of each solution with a 'target' resonance mass which is of interest for the analysis. The invariant mass obtained using each possible neutrino solution set can be compared to this target mass and the neutrino-antineutrino solution set that corresponds to the invariant mass matching most closely to this target mass is taken to be the correct solution. Clearly, this method enhances a signal closest to the target mass, which should generally be the correct solution. However, this has a negative effect on background processes because it creates a bias to solutions whose invariant mass reconstructs nearest to the target mass, regardless of the true invariant mass. This effect is demonstrated in Figure 5.1. In Figure 5.1(a), the invariant mass using neutrino solutions which reconstructs closest to 1 TeV is given by the dashed distribution. In comparison to the invariant mass reconstructed using all generator level particles, given by the solid distribution, only slight broadening is obtained. However, in Figure 5.1(b), a shift to higher mass in the in the Standard Model $t\bar{t}$ spectrum, as compared to the invariant mass of the $t\bar{t}$ system at generator level, is seen when selecting the invariant mass solution that match the closest to the 1 TeV KK-Gluon hypothesis.

(a) KK-gluon
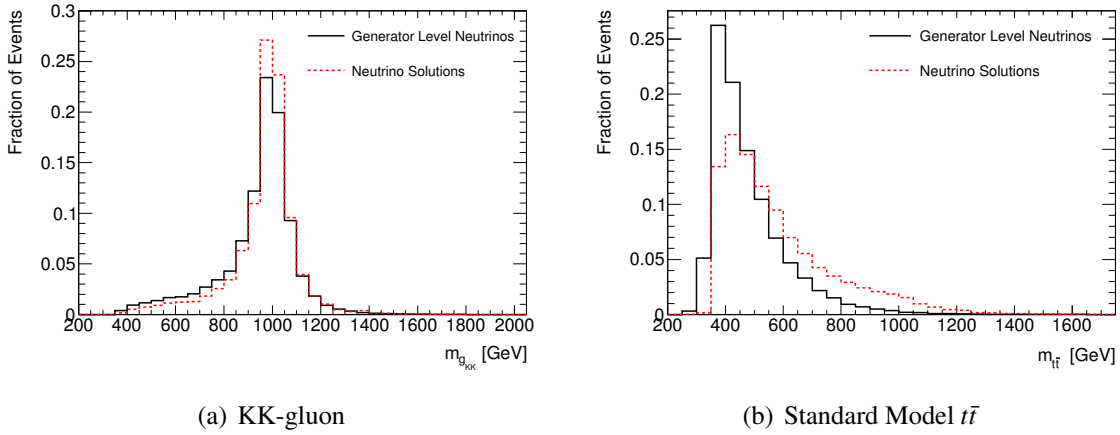
(b) Standard Model $t\bar{t}$

Figure 5.1: $t\bar{t}$ invariant mass for a (a) 1 TeV KK-gluon sample and (b) Standard Model $t\bar{t}$ sample. The solid distribution represents the invariant mass using generator level final state particles while the dashed distributions represents the invariant mass calculated using the neutrino solution that matches most closely to 1 TeV.

Another drawback of this particular method is its dependence on the target mass of the resonance. This dependence means that both the signal and backgrounds change as a function of the target mass. This makes the analysis more complex since the complete evaluation of the background distributions would need to be repeated for each iteration of the analysis corresponding to different target masses. Moreover, biasing background events to the signal region is undesirable because the signal of processes with smaller cross sections, such as the KK-gluon with respect to background, will become more difficult to extract when the observable of background events and signal events overlap.

5.2.2 Characterizing Decay Products

Since this analysis focuses on $t\bar{t}$ resonances, a more physics motivated approach is to characterize the decay of the top quark and use this information to obtain correct neutrino solutions. This approach involves characterizing the relative kinematics of the final state products of the top decay. In this way, the algorithm remains unbiased to signal events since the main background also consists of top quarks. The solutions obtained from solving the system of equations given in 5.2 are purely analytic and contain only some kinematic information. Adding information on the relative kinematics of particles essentially provides

another set of constraints which can be used as selection criteria. To characterize the top decay, the distance in η-φ space between the top quark and the neutrino, ΔR, is obtained for different top quark momentum ranges. This is done because top quarks are common to both the signal and the irreducible background (which is the largest), meaning that no bias towards signal is introduced. A Standard Model $t\bar{t}$ Monte Carlo sample is used to characterize the $\Delta R(t,\nu)$ distributions. In order to obtain a larger sample for the high top-p_T region, the unweighted KK-gluon template sample is also used to characterize this distribution. For each top quark momentum range, the ΔR distribution is normalized and as a result each bin in the distribution has an associated probability value based on this normalization. Once neutrino solutions are obtained, the ΔR between each neutrino solution and the top quark is calculated. Using the characterized $\Delta R(t,\nu)$ distributions, each neutrino solution is assigned a probability. The value obtained by each neutrino solution is compared and the solution which has the highest probability is selected to reconstruct the invariant mass.

As discussed, high-p_T top quarks become boosted and the angular distance between the neutrino and the top quark, $\Delta R(t,\nu)$, gets smaller. Top quarks with small p_T are not boosted and consequently the $\Delta R(t,\nu)$ distribution in these distributions is quite broad. In Figure 5.2, the ΔR distribution between the top quark and neutrino is shown for top quarks with momentum ranges 0-50 GeV (left) and 1550-1600 GeV (right).
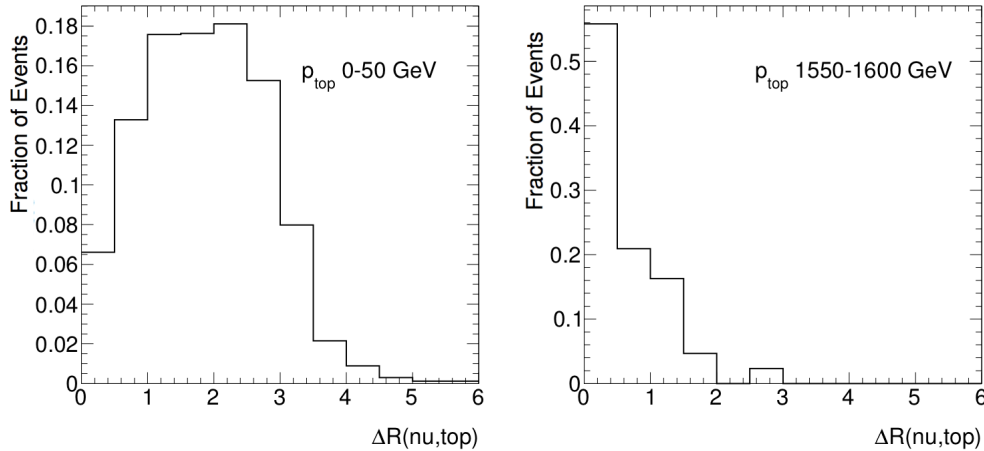
Figure 5.2: $\Delta R(t,\nu)$ for top decays in the range of $p_{top} = 0 - 50$ GeV (left) and $p_{top} = 1550 - 1600$ GeV (right).

Since all kinematics from generator level are provided as input in this scenario, one expects perfect neutrino reconstruction. From the distribution shown in Figure 5.3, it is clear that the kinematic distribution $\Delta R(t,\nu)$ is not, alone, a strongly characterizing variable. In fact, this variable appears to preferentially select neutrino solutions which reconstruct to form a larger resonant invariant mass, which manifests itself in the high-mass tail, in comparison to Figure 5.1(a), resulting in a larger degradation in the resolution of the peak.
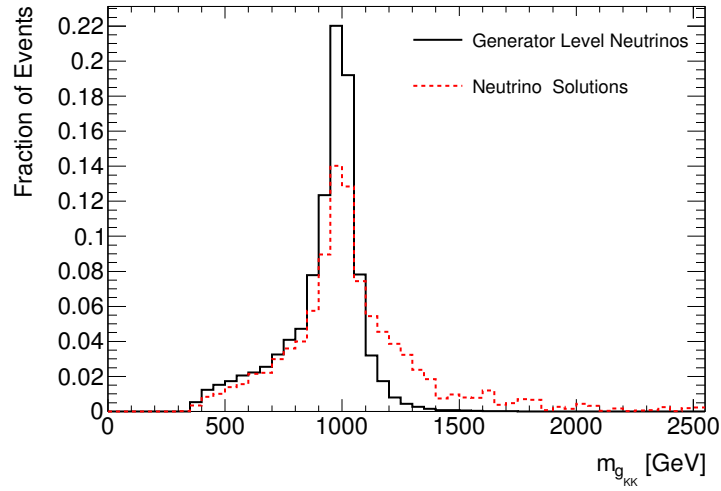
Figure 5.3: Invariant mass distribution using $\Delta R(t,\nu)$ as a kinematic constraint is shown in red. Invariant mass distribution using generator level neutrinos is provided in black for comparison.

In an attempt to improve the discrimination between the correct neutrino solution and the wrong neutrino solution(s), additional kinematic quantities, involving p_T and E, are used. The complete set of kinematic constraints are:

$$\Delta R(t(\bar{t}), \nu(\bar{\nu}))$$
$$\Delta R(\ell^+(\ell^-), \nu(\bar{\nu}))$$
$$\Delta R(b(\bar{b}), \nu(\bar{\nu}))$$
$$p_T^{\nu(\bar{\nu})}/p_T^{b(\bar{b})}$$
$$p_T^{\nu(\bar{\nu})}/p_T^{\ell^+(\ell^-)}$$
$$p_T^{\nu(\bar{\nu})}/p_T^{t(\bar{t})}$$
$$E^{\nu(\bar{\nu})}/E^{b(\bar{b})}$$
$$E^{\nu(\bar{\nu})}/E^{\ell^+(\ell^-)}$$
$$E^{\nu(\bar{\nu})}/E^{t(\bar{t})}.$$

$$(5.3)$$

As was done for $\Delta R(t, \nu)$, each of these kinematic distributions is characterized for different top quark momentum ranges. Each E and p_T ratio is assigned a probability value based on the normalized content in each bin. The likelihood for each event is obtained by taking the product of the probability for each kinematic quantity. The neutrino-antineutrino solution with the highest likelihood is chosen as the correct neutrino solution set. Once the neutrino solution is chosen, the invariant mass is calculated using equation 5.1.

There are two issues that arise when using the kinematic distributions for the selection criteria. First, since each quantity is considered for different top quark momentum ranges, the lack of statistics for top quarks with large momentum becomes problematic when the kinematic quantity calculated for a particular neutrino solution falls in a bin where there are no events. This is rectified by using a nearby bin which has an associated probability and assigning that probability to the event. However, if there is only one bin filled for a specific momentum range, this provides no discriminating power whatsoever. The second issue presents itself when at least two solutions have similar kinematics and as such fall in the same bin. Of course, this problem can be rectified by decreasing the bin size. However, for regions of low statistics, this approach may lead to more empty bins which would increase the occurrence of the first problem. To avoid both of these problems, each kinematic distribution from equation 5.3 is fit to a continuous function for the different top quark momentum ranges. Each different distribution was fit to a continuous function. Top quark momentum ranges of 100 GeV is selected to optimize accurate mapping of the dif-

ferent behaviour of the kinematic distribution as the top quark momentum increases, while providing enough events to fit to a smooth distribution rather than statistical fluctuations. The overflow bin is taken to be for $p_{top} > 1000$ GeV where there are minimal events and the kinematic distributions essentially do not change. In this scenario, solutions with similar kinematics will have unique, and non-zero, probabilities. The likelihood for a given neutrino solution is given by:

$$\mathcal{L} = \prod_i P(\Delta R(i, \nu)) \cdot P(p_T^\nu / p_T^i) \cdot P(E^\nu / E^i). \tag{5.4}$$

where i = bottom quarks, charged leptons, and top quarks. The neutrino solution set which maximizes equation 5.4 is used to reconstruct the invariant mass of the $t\bar{t}$ system.

5.3 Generator Level Studies

In this section, the analytic mass reconstruction methods described in the last section are investigated. The performance of the neutrino solution selection criteria is first investigated for the case where detector effects are not taken into account (referred to as generator, or truth level).

5.3.1 Truth Level Masses

The first step is to characterize the best case scenario. One set of inputs required for the set of equations 5.2 is the masses of the top quarks, bottom quarks, and W bosons. These masses are spread out by their decay width as a direct consequence of the Heisenberg uncertainty principle. This decay width will contribute to the broadening of the invariant mass distributions as they propagate through to the analytic neutrino solutions. At truth level, however, the mass of each of these particles is available on an event-by-event basis and the best case performance of the likelihood method can be characterized by using the known masses as inputs to solve for the neutrino kinematics. Moreover, in this case, neutrino solutions are available for every $t\bar{t}$ event, allowing a direct comparison between analytic neutrino solutions and the true neutrino kinematics for each event.

As previously mentioned, at most 4 solutions can be obtained; if imaginary solutions are obtained, they are rejected. Figure 5.4 shows the number of solutions obtained while

using truth masses. As expected, solutions are obtained for all events.
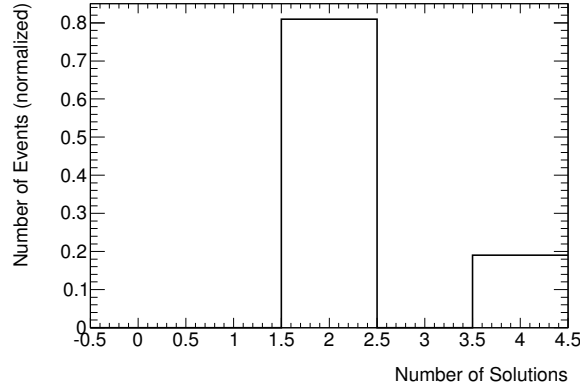
Figure 5.4: Number of neutrino solutions obtained from the analytic mass reconstruction algorithm, per event, using truth level particles.

By applying each kinematic constraint individually, their individual performance can be compared. The invariant mass using neutrino solutions selected by each method is shown in Figure 5.5. The selection criteria generate some broadening when incorrect neutrino solutions are selected. From these distributions, it is clear that the kinematic constraints do not select the correct neutrino solutions all of the time. Particularly, the ΔR distribution between the top quark and the neutrino performs the poorest with respect to choosing the correct neutrino solution. This is evident by the preferential selection of neutrino solutions that reconstruct to form a larger invariant mass, and hence more broadening compared to the true invariant mass.
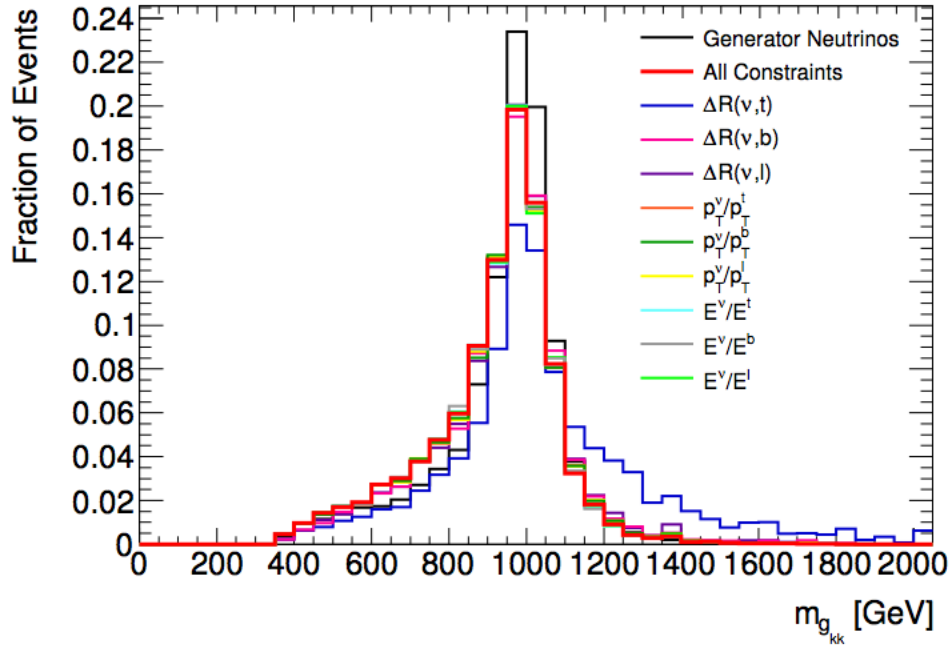
Figure 5.5: KK-gluon invariant mass using all truth level charged leptons and b quarks, while each colored distribution uses neutrino solutions selected by the kinematic constraint as labelled in the legend.

In Figure 5.6, the relative difference between the energy of the analytic neutrino solutions and truth level neutrinos is shown. The dashed line represents the selected neutrino in comparison to the solid line which represents all other neutrino solutions. Overall, the kinematic selection criteria preferentially select neutrinos whose energy matches more closely to the energy of the true neutrino. This is demonstrated by the narrower distributions, peaked at zero, for the selected neutrino solutions (dashed) in comparison to the broader non-selected neutrino solutions (solid).
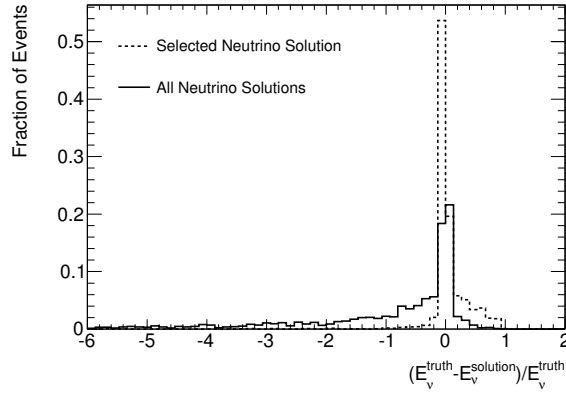
Figure 5.6: Energy resolution of the reconstructed neutrino relative to truth level neutrinos. The dashed (solid) lines represent the selected (all) neutrino solution(s).

5.3.2 Truth level - Pole Masses

Considering a more realistic scenario, the pole mass of the top quark and *W* boson is used as input into the kinematic constraints from equation 5.2 rather than the mass of the particles at truth level on an event by event basis. Truth level final state objects are still used. In this case, some broadening of the invariant mass distribution is expected since neutrino solutions may vary as a result of using the average pole mass. Most of the time, the pole mass of both the top quark and the *W* boson provides a good estimate of their mass and neutrino solutions are obtained. If the true mass of either the *W* boson or the top quark is very off-shell, there may be no analytic solution satisfying the set of equations in 5.2. If no solution is obtained, the input masses of the top quarks and *W* bosons are varied within a more tightly constrained Breit-Wigner width, relative to their known width. This is repeated until a solution is obtained, for at most 1000 iterations. For this scenario, however, a solution is obtained for every event. The variation, as compared to top quark and *W* masses from truth level, is shown in Figure 5.7.

(a) Relative top mass variations.

(b) Relative *W* boson mass variations.
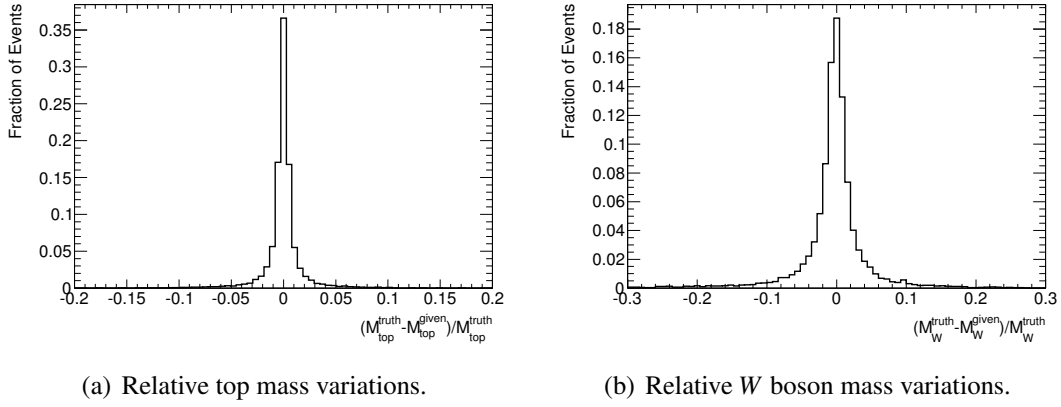
Figure 5.7: Relative variations between true (a) top quark and the mass provided to solve for neutrino four-vectors and the (b) true *W* boson mass and mass provided to solve for neutrino four-vectors.

The invariant mass distributions selected using the individual constraints in Equation 5.2, and the combined constraints, are shown below in Figure 5.8.
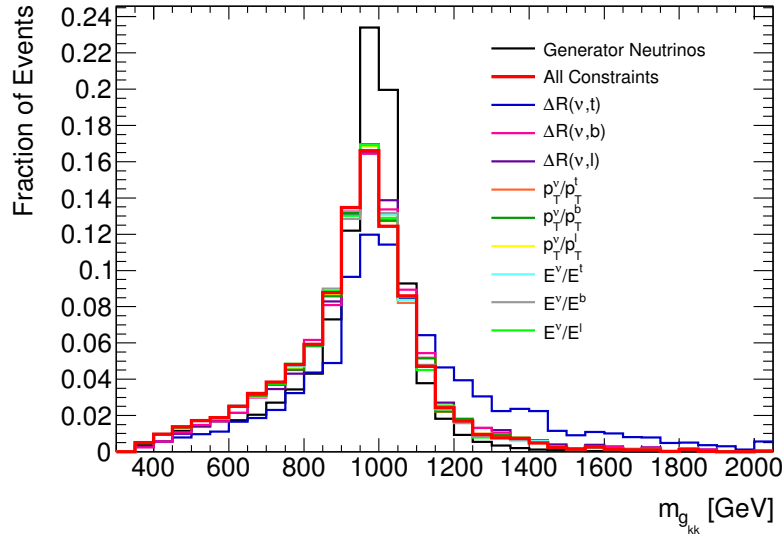
Figure 5.8: Invariant mass distributions using individual kinematic constraints for neutrino selection, as labelled in the legend. The black distribution uses truth level neutrino four-vectors for reconstructing the invariant mass.

From the distributions shown in Figure 5.8, it is clear that the invariant mass distribution broadens when the pole masses of top quarks, bottom quarks, and *W* bosons are used (in comparison to distributions shown in Figure 5.5). To numerically characterize the performance of this method, the invariant mass using each neutrino solution is compared to the invariant mass using truth level neutrinos. The invariant mass reconstructed with neutrino solutions that match most closely to the truth invariant mass is chosen. With at least two solutions, there is the possibility that there are two kinematically similar neutrinos and in such cases choosing either solution may not yield any difference in the reconstructed invariant mass. To quantify this, events are considered to be correct if they satisfy the condition given below in Equation 5.5.

$$\text{Correct Solution} = \min|m_{truth} - m_{solution}| \qquad (5.5)$$

The efficiency of selecting the correct solution for each kinematic variable is given in Table 5.1. If a neutrino solution is chosen that leads to a reconstructed mass that has the smallest difference to the truth invariant mass, the values in Table 5.1 provide the fraction of events which are within the same mass bin or one bin (50 GeV) from the truth level invariant mass. On the other hand, if this neutrino solution is not chosen, Table 5.1 provides the fraction of events where the invariant mass calculated using the selected neutrino are within the same mass bin or one mass bin from the invariant mass distribution which uses the neutrino solution that leads to the reconstructed invariant mass that has the smallest difference to the truth invariant mass. It is important to note that the values given in Table 5.1 are calculated for a 1 TeV KK-gluon. Since the kinematic distributions change for different KK-gluon resonance masses, the efficiency of each kinematic variable will also be different for each mass point.

In Figure 5.9, poorer energy resolution is seen in comparison to 5.6, where the event-by-event mass of both the top quark and the *W* boson is used to reconstruct the neutrino four-vectors. However, the resolution of the selected neutrino solution is, again, better than the resolution of the entire set of possible neutrino solutions. This indicates that the neutrino solution selection criteria provides good discrimination between correct and incorrect neutrino solutions.

Table 5.1: Correct solution selection based on each kinematic constraint for a 1 TeV KK-gluon MC sample using truth objects and pole masses.

| Constraint(s)	Closest Mass Soln Chosen				Other Chosen		
	Closest Mass Solution Chosen	± (0-50) GeV	± (50-100) GeV	> 100 GeV or < -100 GeV	± (0-50) GeV	± (50-100) GeV	>100 GeV or < -100 GeV
$\Delta R(b,\nu)$	0.73	0.78	0.12	0.10	0.59	0.17	0.24
$\Delta R(\ell,\nu)$	0.72	0.78	0.12	0.10	0.57	0.19	0.24
$\Delta R(t,\nu)$	0.36	0.76	0.13	0.11	0.39	0.15	0.46
p_T^ν/p_T^b	0.85	0.80	0.11	0.09	0.60	0.17	0.23
p_T^ν/p_T^ℓ	0.85	0.80	0.11	0.09	0.59	0.17	0.24
p_T^ν/p_T^t	0.85	0.80	0.11	0.09	0.59	0.17	0.24
E_ν/E_b	0.89	0.80	0.11	0.09	0.66	0.15	0.19
E_ν/E_ℓ	0.90	0.80	0.11	0.09	0.67	0.17	0.16
E_ν/E_t	0.90	0.80	0.11	0.09	0.66	0.16	0.18
All	0.87	0.79	0.12	0.09	0.65	0.17	0.18
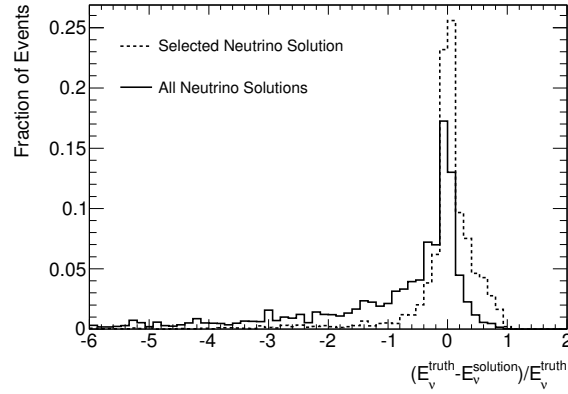
Figure 5.9: Energy resolution of the analytic neutrino solutions relative to truth level. The dashed (solid) lines represent the selected (all) neutrino solution(s).

In Figure 5.10(a), two-dimensional distributions of the truth level invariant mass and of the invariant mass solution which is closest to the truth invariant mass is shown. In comparison, the neutrino solution selected via the likelihood selection is shown in Figure 5.10(b). In this case, there is clear broadening for both the closest and selected invariant mass solutions.

(a) Closest Solution.

(b) Chosen Solution.
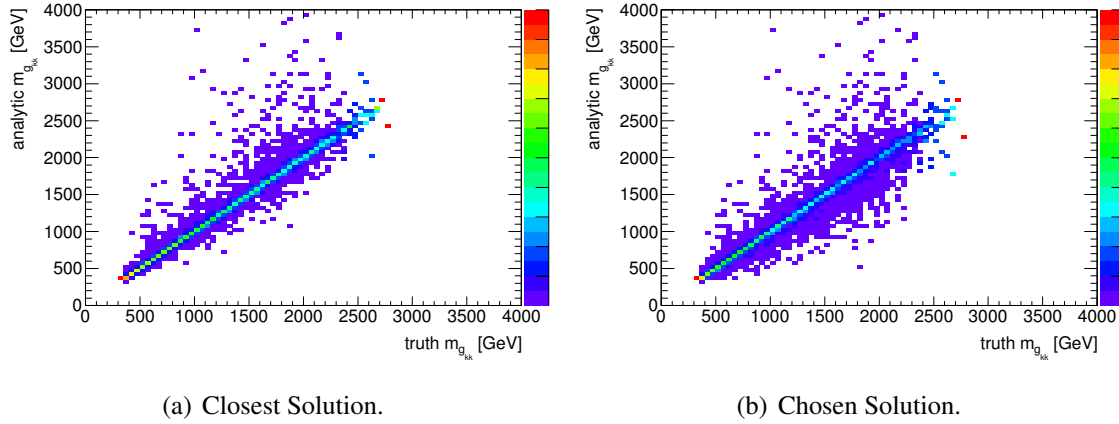
Figure 5.10: The 2-dimensional distribution of the invariant mass using truth level neutrino four-vectors in the mass reconstruction and using analytic neutrino solutions which form the closest truth invariant mass (left) and the selected neutrino solutions (right).

Chapter 6

Mass Reconstruction with Detector Simulated Objects

In order to use the analytic mass reconstruction algorithm on ATLAS data, the effects that resolution introduces to this algorithm are studied. In Chapter 5, the effects of using the pole mass of the top quark and the *W* boson were studied. Now, in addition, the effects of using detector simulated particles are studied. In comparison to using truth level particles, broadening of the invariant mass distribution is expected as a result of the measurement resolution of leptons and jets with the ATLAS detector. Moreover, since *b*-quarks are reconstructed in the detector as jets, and no charge information is used to assign the jets to the correct top quark, there is a n-fold ambiguity in the jet assignment, where n is the number of jets in the event which pass the event and object selection criteria described in Chapter 4. These effects will be studied in this chapter, and the performance of the mass reconstruction algorithm will be presented on both signal and background events.

There are many complications that arise when implementing this algorithm on fully simulated events that include the detector simulation, and analogously real LHC *pp* collision events recorded by the ATLAS detector. Such objects are referred to as reconstructed objects. In parallel with the previous chapter, the first issue to consider is how the use of reconstructed objects affects the kinematic constraints employed for the neutrino solution extraction. Since the four-vectors of the top quark cannot be directly measured with the ATLAS detector, the kinematic criteria given in equation 5.3 which are defined in terms of $p_{(T)}^{top}$ are not available. In the real experimental scenario, only information of reconstructed

objects measured with the ATLAS detector are directly available for analysis. Figures 6.1 and 6.2 show the correlation between the momentum of the top quark and b-quark, and of the top quark and charged lepton, respectively. Equivalently, Figure 6.3 shows the correlation between the momentum of the top quark and the combined lepton+jet system. The left (right) plots show the correlation between particles simulated without (with) detector resolution effects. The correlation factor provided in the inset is defined by the covariance factor between the x and y axes [34].
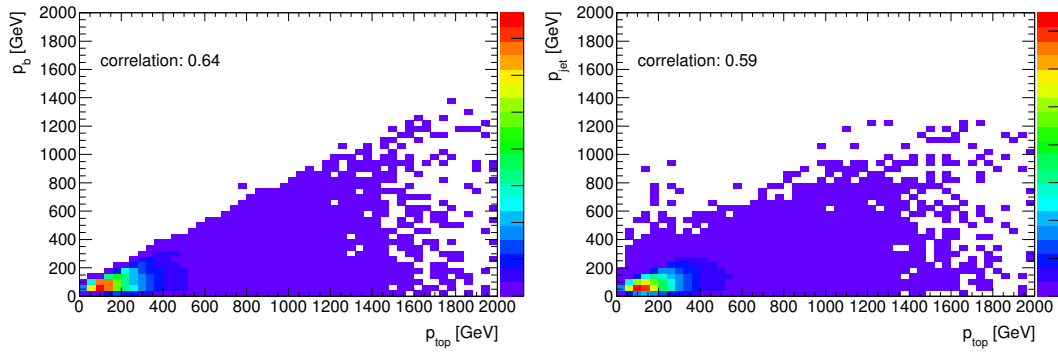
Figure 6.1: Left: Correlation plot for top momentum and b quark momentum. Right: Correlation plot for top momentum and momentum of reconstructed jet matched to b quark.
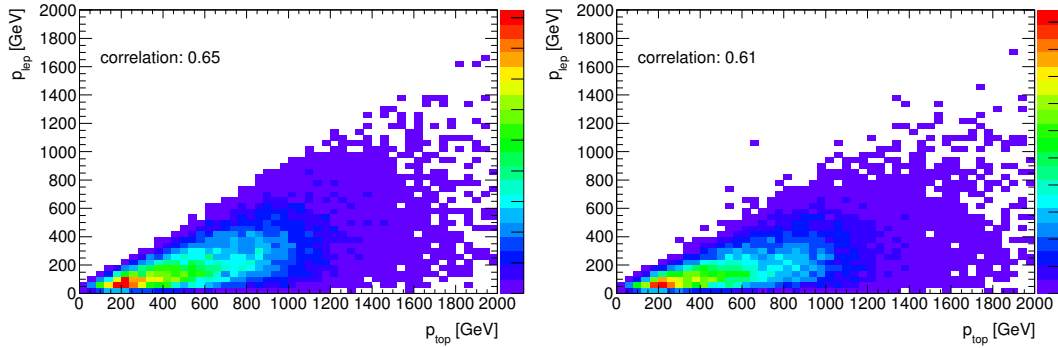
Figure 6.2: Left: Correlation plot for top momentum and charged lepton momentum. Right: Correlation plot for top momentum and reconstructed charged lepton momentum.
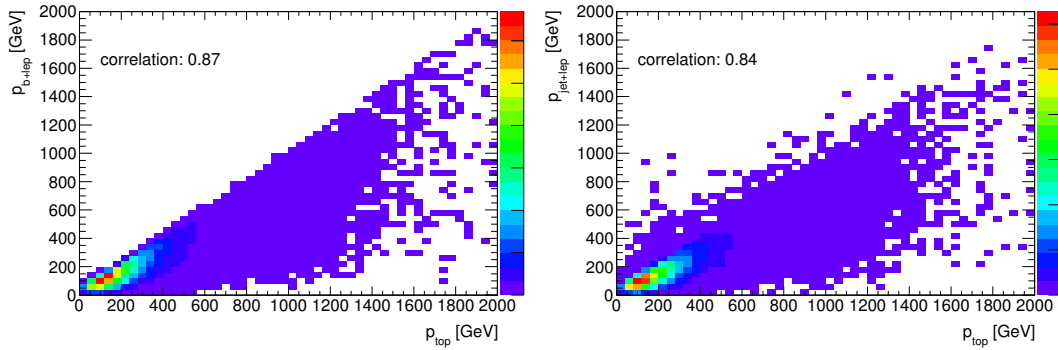
Figure 6.3: Correlation plot for top momentum and the momentum of the combined lepton+jet system at truth level (left) and reconstructed level using jets matched to *b* partons (right).

In the fully reconstructed scenario, the momentum of the combined lepton+jet system is used as a proxy for the top quark momentum since it shows the highest correlation to the top quark momentum in comparison to the correlation between the top quark and the jet or charged lepton individually. Following the procedure outlined in Chapter 5, each kinematic variable is binned in different lepton+jet momentum ranges rather than top momentum ranges.

6.1 Resolution Effects

From the set of equations used to calculate the neutrino solutions, as provided in equations 5.2, the inputs that depend on detector measurements are the four-vectors of the *b*-quarks, leptons, and the missing energy. Since these kinematic quantities are used in the analytic reconstruction of neutrino four-vectors, any mismeasurements of these quantities propagates to the neutrino four-vector solutions.

The energy resolution of both the leptons and jets is shown in Figure 6.4. It is clear from these distributions that the detector resolution is worse for jets than it is for leptons. Another source of resolution smearing that affects the analytic mass reconstruction comes from the transverse components of the missing energy. The $E_{x,y}^{miss}$ resolution, with respect to the missing energy from the two neutrinos, is shown in Figure 6.5.

(a) Lepton energy resolution

(b) Jet energy resolution
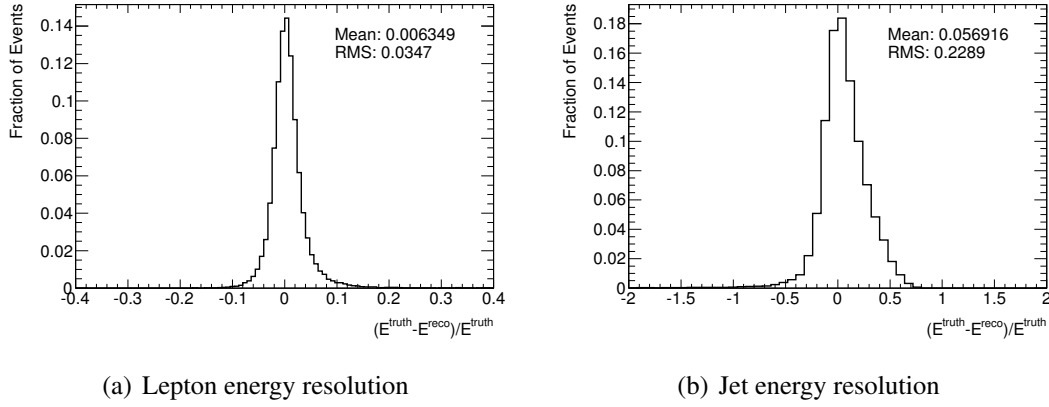
Figure 6.4: Simulated energy resolutions of leptons and jets as measured by the ATLAS detector.
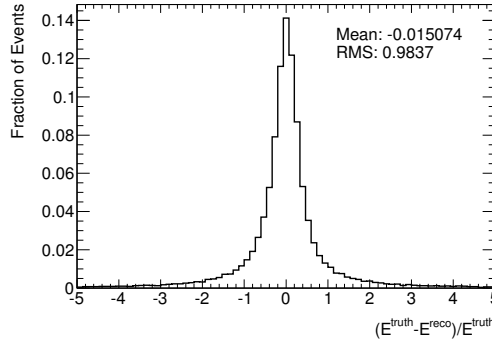
Figure 6.5: Simulated $E^{miss}_{x,y}$ resolution as measured by the ATLAS detector.

In the fully reconstructed scenario, the two leading jets are selected to be the jets that originate from the two top quark decays. At random, each of the two leading jets is assigned to one of the top quarks. In addition to the procedure given in chapter 5, if no solution is obtained after 1000 variations of the top quark mass and W boson mass, the two jets are permuted and the algorithm is repeated. In contrast to the truth level approach, solutions are not obtained for every single event; 7% of the time no solution is obtained for either jet permutation. Of most concern is the subset of events where no solution is obtained and both jets selected originate from b quarks since these provide the most promising possibility of proper analytic neutrino reconstruction. For these events, the measured detector objects are

characterized. In Figure 6.6, the two-dimensional energy resolution distributions of two different objects are provided.

(a) Lepton vs. E_T^{miss}

(b) Jet vs. E_T^{miss}

(c) Jet vs. Lepton
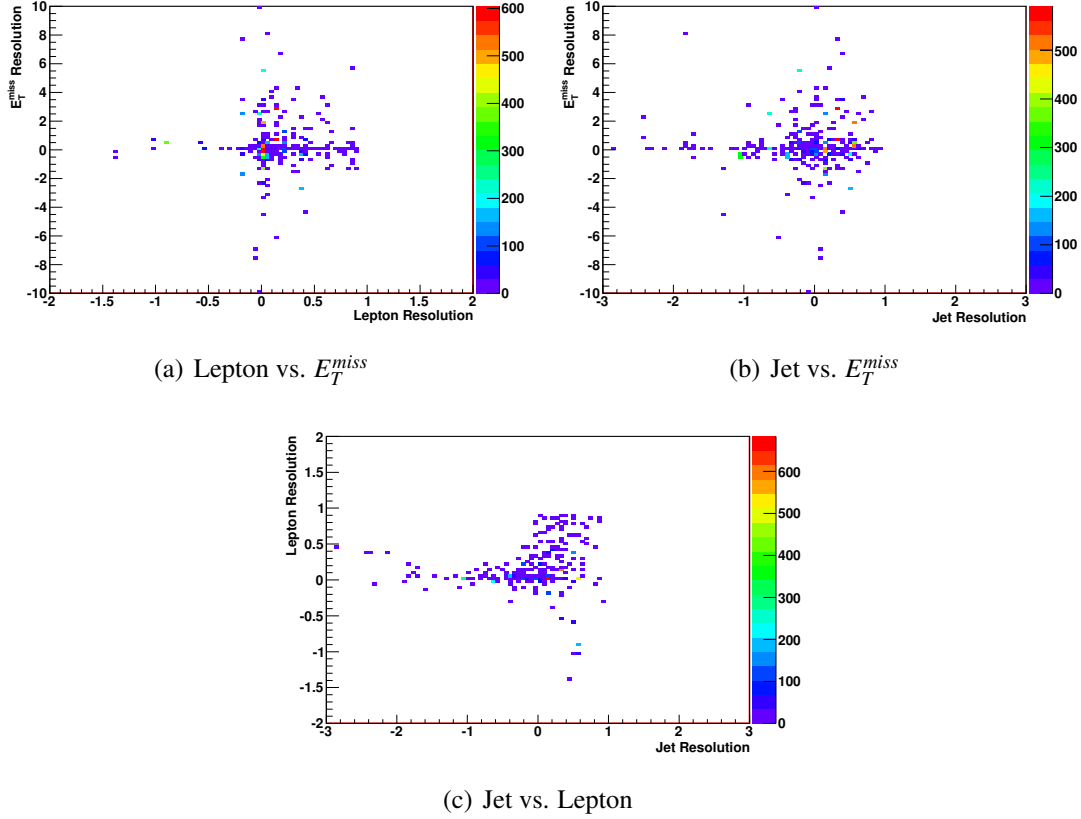
Figure 6.6: 2-dimensional resolution distributions for the subset of events where no neutrino solutions are obtained.

Poorer resolution is seen for these subset of events in comparison to the average resolution distributions shown in Figures 6.4 and 6.5. If any object(s) have poor resolution, there is no reason that any solution should be obtained since these measured kinematics may not fit the top decay kinematics. Fortunately the subset of events, where no solutions are obtained when both jets are matched to truth, only represents approximately 1% of the sample of events and does not provide a large degradation in event acceptance.

6.2 Invariant Mass

The invariant mass using fully reconstructed objects is studied in this section. The invariant mass distributions for each neutrino solution selection criteria, individually and combined, is shown in Figure 6.7. Clear degradation, in comparison to the truth level distributions shown in Figure 5.8 is seen. In Figure 6.7, the black distribution represents the invariant mass using truth level neutrinos whereas the colored distributions use analytic neutrino solutions selected via the kinematic(s) constraint(s) denoted in the legend. For all of the colored distributions, large broadening is seen in the invariant mass distributions, with generally about a 40% decrease in the peak height at 1 TeV, in comparison to the black distribution.
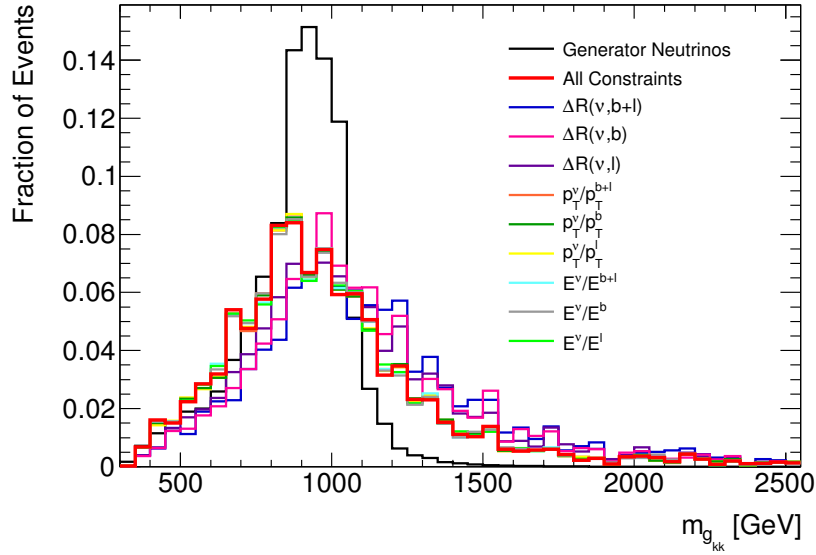
Figure 6.7: Invariant mass distributions obtained using reconstructed leptons and jets, and using neutrino solution selected from individual constraints as labelled in the legend. The black distribution uses reconstructed leptons and jets with truth level neutrinos.

Table 6.1: Correct solution selection based on each kinematic constraint for a 1 TeV KK-gluon MC sample using reconstructed objects.

Constraint(s)	Closest Mass Solution Chosen	Closest Mass Soln Chosen			Other Chosen		
		$\pm$ (0-50) GeV	$\pm$ (50-100) GeV	> 100 GeV < -100 GeV	$\pm$ (0-50) GeV	$\pm$ (50-100) GeV	> 100 GeV or < -100 GeV
$\Delta R(b,\nu)$	0.44	0.32	0.21	0.47	0.20	0.19	0.61
$\Delta R(\ell,\nu)$	0.55	0.30	0.20	0.50	0.21	0.20	0.69
$\Delta R(t,\nu)$	0.40	0.27	0.18	0.65	0.20	0.18	0.62
p_T^y/p_T^b	0.84	0.38	0.22	0.40	0.24	0.20	0.56
p_T^y/p_T^ℓ	0.84	0.38	0.22	0.40	0.25	0.21	0.54
p_T^y/p_T^t	0.84	0.38	0.22	0.40	0.24	0.21	0.55
E_ν/E_b	0.88	0.38	0.21	0.41	0.29	0.18	0.53
E_ν/E_ℓ	0.88	0.38	0.21	0.41	0.26	0.18	0.56
E_ν/E_t	0.88	0.38	0.21	0.41	0.26	0.19	0.55
All	0.85	0.38	0.21	0.41	0.27	0.20	0.53

The numerical selection efficiency, which is defined by satisfying equation 5.5, for each kinematic variable is given in Table 6.1. If a neutrino solution is chosen that leads to a reconstructed mass that has the smallest difference to the truth invariant mass, the values in Table 6.1 provide the fraction of events which are within the same mass bin or one bin (50 GeV) from the truth level invariant mass. On the other hand, if this neutrino solution is not chosen, Table 6.1 provides the fraction of events where the invariant mass calculated using the selected neutrino are within the same mass bin or one mass bin from the invariant mass distribution which uses the neutrino solution that leads to the reconstructed invariant mass that has the smallest difference to the truth invariant mass.

Much like the truth level results, the ΔR constraints do not select the most closely matched neutrino solutions to true neutrino solutions, however, its contribution to the selection criteria has a negligible effect once all the other kinematic criteria are implemented. This is demonstrated in Table 6.1, where the fraction of events using all of the combined kinematic constraints is better than each ΔR and p_T individual constraints. Although the ΔR constraints have no effect on the event selection once all kinematic constraints are used, each p_T and E ratio provide very similar, and good, discriminating power; the p_T and E kinematic constraints selects the closest solution to truth 84% and 88% of the time, respectively. Although, visually from the invariant mass distribution, it may appear that the constraints do not provide good guidance in the neutrino selection, 85% of the time the closest neutrino solution, as quantified by equation 5.5, to the truth neutrino solution is selected via the kinematic ratio(s). This implies that all solutions are largely affected by the resolution of the reconstructed objects used as input in to the mass calculator.

The decrease in resolution of the invariant mass peak is largely due to performance of reconstructing neutrino solutions that match the true neutrino in the event. This is depicted in Figure 6.8, where the energy resolution of the selected neutrino relative to the truth neutrinos are shown. In this scenario, the spread of the selected neutrino solution relative to the truth neutrino is smaller compared to the spread of all neutrino solutions and truth neutrinos. This demonstrates that, overall, the algorithm preferentially selects the neutrino solutions which reconstruct most closely to the truth level neutrinos. However, in comparison to the same distributions shown in the truth level scenario, the overall spread in the energy of the neutrino solutions is much larger.
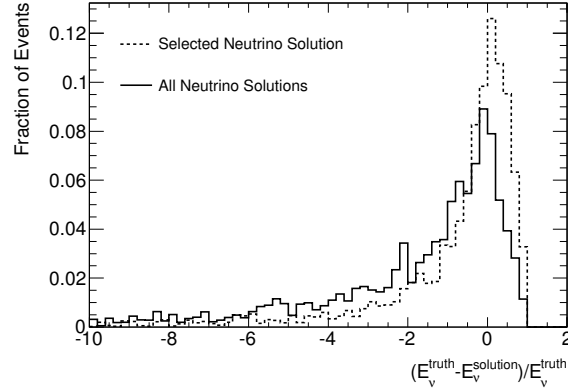
Figure 6.8: Energy resolution of the reconstructed neutrinos. The dashed (solid) lines represent the selected (all) neutrino solution(s).

Analogous to the previous chapter, the two-dimensional distributions of the invariant mass using truth neutrinos and neutrino solutions are shown in Figure 6.9. To compare, Figure 6.9(a) shows the two-dimensional distribution of the invariant mass with the selected neutrino solution, while Figure 6.9(b) shows two-dimensional distribution between the event whose invariant mass is closest to the truth invariant mass.

(a) Chosen Solution.
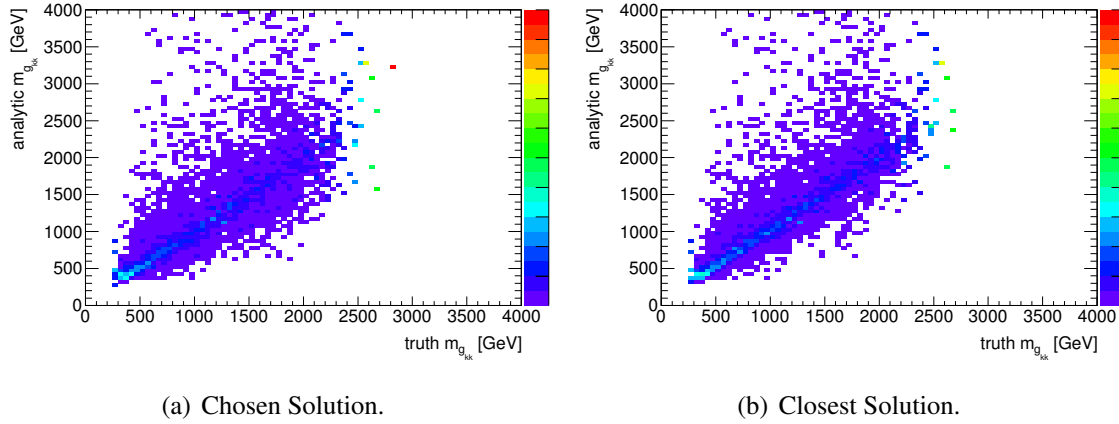
(b) Closest Solution.

Figure 6.9: The 2-dimensional distribution of the invariant mass using truth level neutrino four-vectors in the mass reconstruction and using four-vectors obtained from the analytic neutrino solutions which form the closest invariant mass to the true mass of the event.
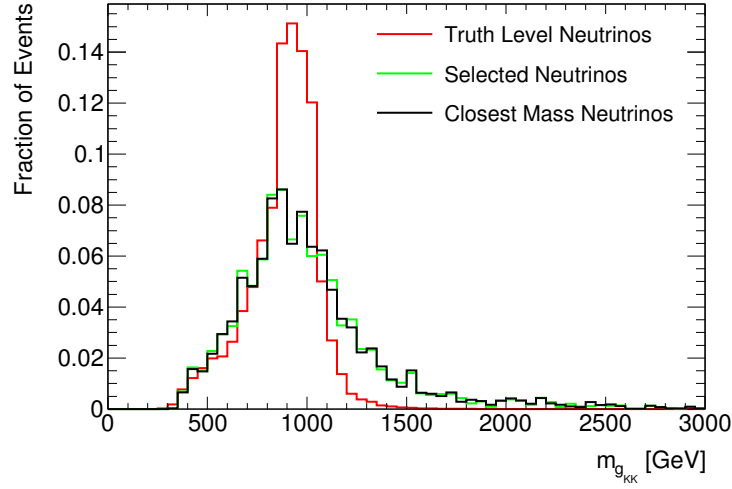
Figure 6.10: Invariant mass of a 1 TeV KK-gluon. Both distributions use reconstructed leptons and jets. The dashed line distribution uses the truth neutrino four-vectors whereas the solid distribution uses the neutrino solutions which match most closely to the truth neutrinos.

In Figure 6.10, the corresponding invariant mass distributions are shown. From the behaviour of all the distributions shown, it is evident that the effect that the resolution of measured objects is significant. Particularly, no significant differences are seen between the two distributions shown in Figure 6.10. This signifies that although the invariant mass distribution using selected neutrino solutions looks broad in comparison to the invariant mass distribution which uses truth level neutrinos, the selected neutrino solution essentially provides the best possible invariant mass reconstruction that can be attained when using the reconstructed objects as input into the neutrino kinematic solver. It is clear that the resolution has a negative effect on the ability to correctly reconstruct the neutrino four-vectors and because of this a large broadening of the invariant mass distributions is seen.

6.3 Kinematic Likelihood Fitter

Since the resolution of the analytic neutrino solutions are dependent on the resolution of the particles, it is important to consider these resolution effects. In Figure 6.7, the degradation

of the invariant mass reconstruction due the resolution of the objects, namely the energy of jets and subsequently the missing energy, can be seen.

In order to improve the resolution of the reconstructed $t\bar{t}$ mass, a kinematic likelihood approach is implemented. This method involves maximizing a multi-parameter likelihood function. This likelihood function is calculated based on the Breit Wigner constraints on the mass of the top quark and W boson mass and the resolution constraints for muons, electrons, jets, and missing transverse energy obtained from simulation. The likelihood function for the $t\bar{t}$ dilepton events is then defined as:

$$
\begin{aligned}
\mathcal{L} \;=\; & BW[m(l_1\nu_1)|m_W,\Gamma_W] \cdot BW[m(l_2\nu_2)|m_W,\Gamma_W] \cdot \\
& BW[m(l_1\nu_1 b_1)|m_{t_1},\Gamma_{t_1}] \cdot BW[m(l_2\nu_2 b_2)|m_{t_2},\Gamma_{t_2}] \cdot \\
& W[E_{jet_1}|E_{b_1}] \cdot W[E_{jet_2}|E_{b_2}] \cdot W[E_{\ell_1}|E_{lep_1}] \cdot \\
& W[E_{\ell_2}|E_{lep_2}] \cdot W[E_x^{miss}|p_{x,\nu}] \cdot W[E_y^{miss}|p_{y,\nu}],
\end{aligned}
\tag{6.1}
$$

where *BW* represents the Breit-Wigner function, which constrains the invariant mass of particles to the known pole mass, and *W* represents a transfer function, which quantifies the probability that the measured object originates from the true final state particle [35]. After scanning the parameter space, the set of parameters which maximizes this likelihood distribution is chosen. This algorithm uses the Markov Chain Monte Carlo (MCMC) technique and is implemented using the Bayesian Analysis Toolkit (BAT) to scan the parameter space [36]. For each sampled set of parameters, the neutrino solutions are calculated. If a set of neutrino solutions is obtained, the best neutrino solution is selected by the constraints given in 5.4, else if no neutrino solution is obtained with the generated parameter set, the likelihood is not calculated for the set of parameters. The likelihood, as defined in equation 6.1, is calculated for the selected neutrino solution pair. This algorithm is repeated for 2000 iterations and after all iterations are complete, the parameters which provide the maximum likelihood is selected as the appropriate object parameter set.

The range in which the parameters are allowed to vary are defined in the following way:

Table 6.2: List of the parameter ranges that each objects are varied within.

Object	Parameter Range
Electrons	$\pm 20\%$
Muons	$\pm 20\%$
Jets	$\pm 30\%$
Missing Energy	± 40 GeV
Top Quark Mass	160 - 190 GeV
W Boson Mass	60 - 100 GeV

In addition to parameter variation, the permutation of the two leading jets (to each top decay branch) are compared. For both permutations, the likelihood is obtained and the maximum likelihood of the two is selected as the correct permutation. The difference for the likelihood values obtained for both permutation are given below in Figure 6.11.

In this Figure, a distinction can be seen between the permutation that was chosen in comparison to the permutation which was not chosen. This method allows some permutation providing some distinction between the two solutions.
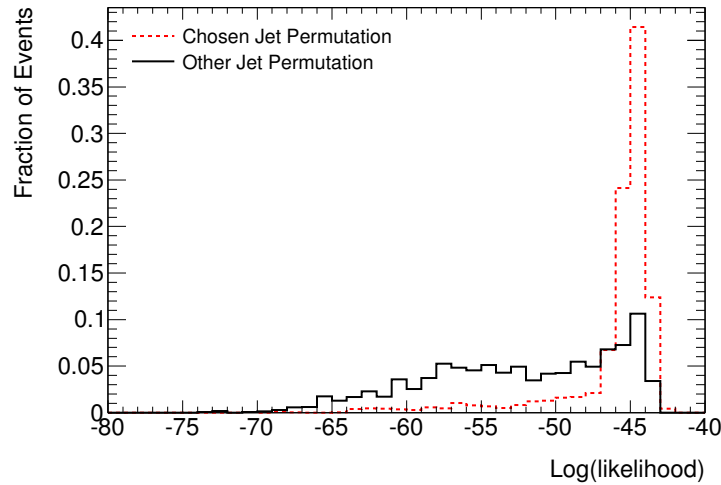
Figure 6.11: Distributions of the logarithmic values of the likelihood for the permutation with the highest likelihood (red) and the other permutation (black).

Characterizing the event using this likelihood method, an increase in the number of solutions per event is seen as shown below in Figure 6.12. The increase in events with 4 solutions in comparison to 2 solutions enhances the probability that the correct neutrino solution set is reconstructed.
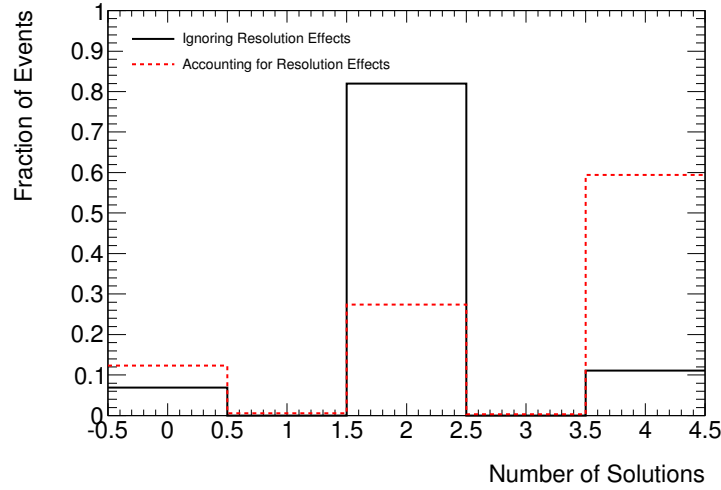
Figure 6.12: The distribution of the number of solutions obtained for the set of variables yielding the highest likelihood (red) and obtained when no parameter variation is implemented (black).

For the purpose of comparison between methods, Figure 6.13 shows the invariant mass distributions when the object resolution is ignored and when it is considered. Comparing the two, relative to the truth level distribution, a more centralized distribution is seen when considering object resolution, however no significant improvement is observed.
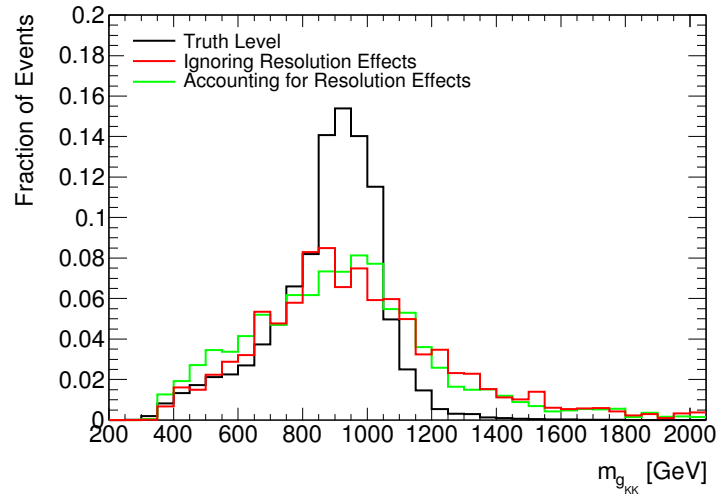
Figure 6.13: 1 TeV KK-gluon invariant mass distributions. The black (red distribution uses truth level (analytic solution) neutrinos and reconstructed leptons and jets. The green distribution uses the set of four vectors of leptons and jets along with the analytically calculated neutrinos with the highest likelihood.

Chapter 7

Performance

7.1   Resonance Mass and Width Dependence

The previous chapters have all focused on the improvements on the object selection and neutrino solution extraction for a KK-gluon with a mass of 1 TeV. However, since a quasi-flat (in mass) MC sample is used, it can be re-weighted to a different resonance mass, allowing a large range of KK-gluon masses which can be investigated. Moreover, the effect of the decay width of the resonance on the neutrino reconstruction can be characterized by re-weighting the KK-gluon MC sample to a narrower width than that of the KK-gluon. In the RS model, the KK-gluon has a width between 11-13% of its mass in the range of 500-2300 GeV. Between the large decay width of the KK-gluon and the effects of parton luminosity, the discriminating variable becomes increasingly broad for increasing KK-gluon masses. To see the effect that the width of the resonance has on the neutrino reconstruction algorithm, the KK-gluon template sample is re-weighted to a width of 6.5% of its mass, which is half of the width of the KK-gluon at 1 TeV*.

In Figure 7.1, the invariant mass for a (a) 750 GeV, (b) 1 TeV, (c) 1.5 TeV and (d) 2 TeV KK-gluon are shown. For comparison, in Figure 7.2, the invariant mass for the narrow $t\bar{t}$ resonance is shown.

---

*Many BSM models predict new $t\bar{t}$ resonances, such as Z', Topcolor, etc.

(a) 750 GeV
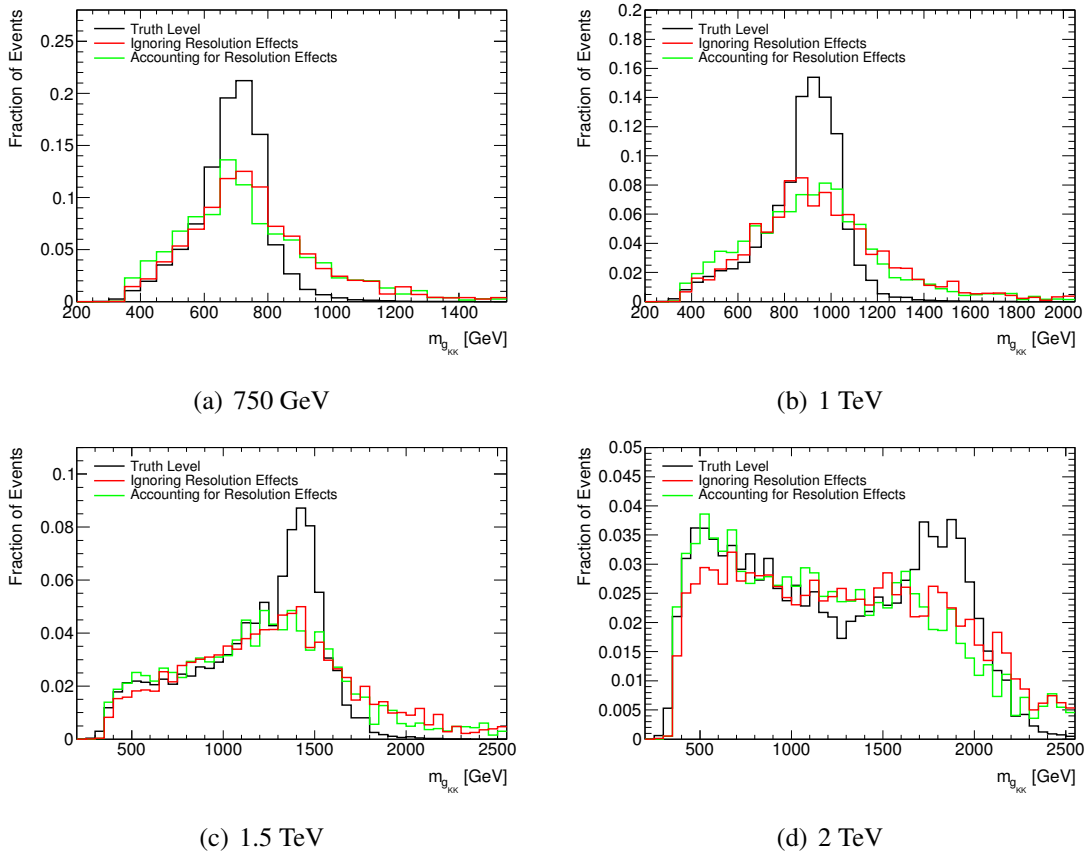
(b) 1 TeV

(c) 1.5 TeV

(d) 2 TeV

Figure 7.1: Invariant mass distributions for (a) 750 GeV (b) 1 TeV (c) 1.5 TeV and (d) 2 TeV KK-gluon. The black line represents the invariant mass truth level neutrinos. The red distribution uses reconstructed charged leptons and jets, and uses neutrino solutions obtained from kinematic constraints. The green distribution uses the set of four vectors of leptons and jets and calculated neutrinos which give the highest likelihood of the kinematic fitter.

Figure 7.1 suggests a slightly better performance of the analytic mass reconstruction when object resolution is considered, compared to the case when object resolution is ignored, since the distribution tends to follow some of the features of the truth invariant mass. This is particularly evident in the low mass tails. The same effect is also seen in Figure 7.2 for the invariant mass distributions of the narrow $t\bar{t}$ resonance.

(a) 750 GeV
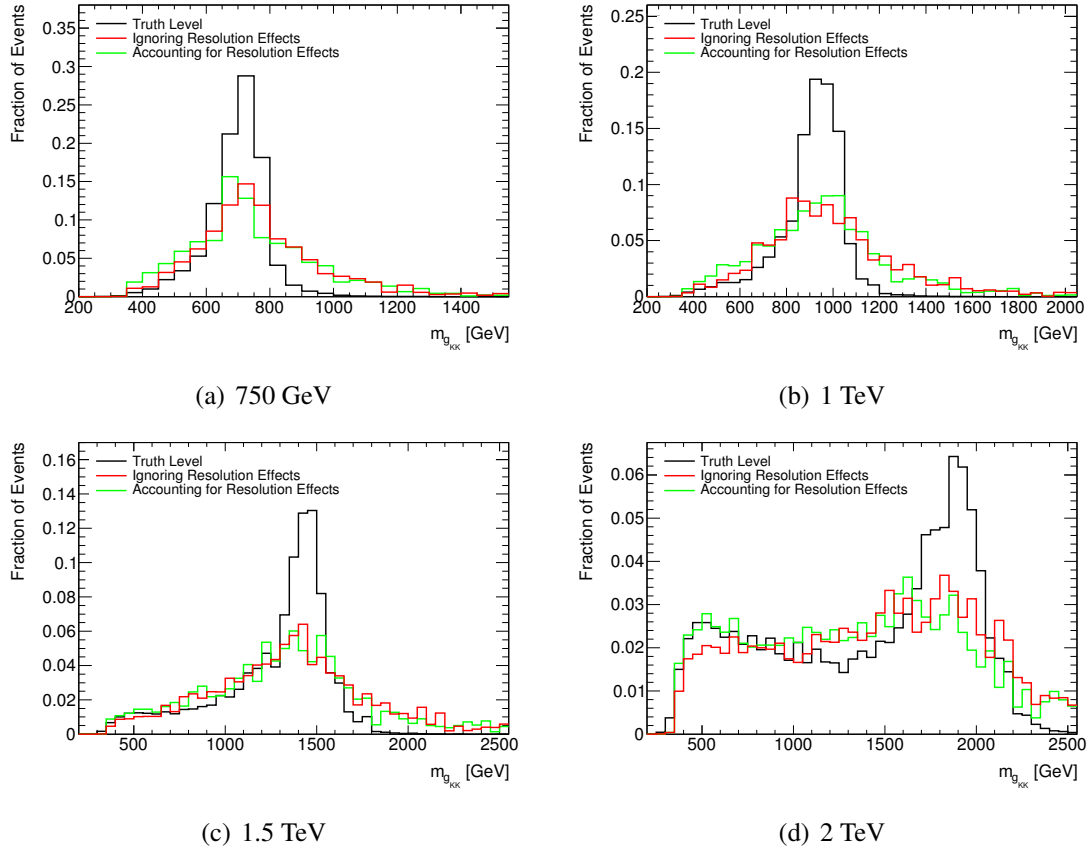
(b) 1 TeV

(c) 1.5 TeV

(d) 2 TeV

Figure 7.2: Invariant mass distributions for (a) 750 GeV (b) 1 TeV (c) 1.5 TeV and (d) 2 TeV $t\bar{t}$ resonance with a decay width of 6.5% of its mass. The black line represents the invariant mass using truth level neutrinos. The red distribution uses reconstructed charged leptons and jets, and uses neutrino solutions obtained from kinematic constraints. The green distribution uses the set of four vectors of leptons and jets and calculated neutrinos which give the highest likelihood of all sampled parameters.

To provide a more meaningful comparison between the two distributions, the sensitivity of the search for both the narrow and broader $t\bar{t}$ resonance will be compared and discussed in Section 7.3.

7.2 Background

The irreducible background for $t\bar{t}$ resonances is Standard Model $t\bar{t}$ production as their final states are identical. A desired property of any analysis that searches for new physics is to identify an observable that separates signal from background events. Because the SM $t\bar{t}$ is the dominant background, at high mass it will be used as an approximation of the total background to the signal events. In Figure 7.3, the invariant mass using the analytic mass reconstruction is shown using truth level neutrinos (black), and analytic neutrino solutions constrained by top decay kinematics ignoring resolution effects (red) and accounting for resolution effects (green).
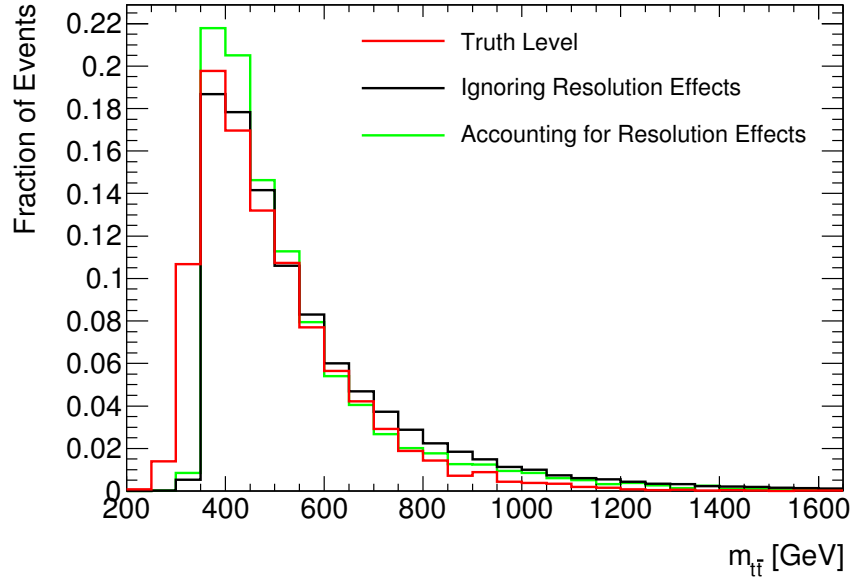
Figure 7.3: Performance of the invariant mass reconstruction algorithm on the Standard Model $t\bar{t}$ background. The red (black) distribution uses truth level (analytic solution) neutrinos and truth level leptons and jets. The green distribution uses the set of four vectors of leptons and jets along with the analytically calculated neutrinos with the highest likelihood.

By comparing the invariant mass distribution that uses analytic neutrino solutions with the distribution that uses truth level neutrinos, it is clear that the effect that the resolution of the reconstructed objects has on the SM $t\bar{t}$ background is much less significant than the effect it has on signal events. There is, however, a high-mass tail that manifests itself when implementing the algorithm. Although small, the shift to higher mass is unfavorable because the cross-section of the SM $t\bar{t}$ background process is much larger than that of the KK-gluon. The smaller the overlap between signal and background processes, the better the signal extraction.

In Figure 7.3, the invariant mass distribution when using the kinematic likelihood method, as depicted by the green distribution, is both narrower and more shifted to lower mass in comparison to the method which does not consider object resolution, as depicted by the red distribution.

In Figures 7.4 through 7.6, the distributions for both signal and the $t\bar{t}$ background are shown for both the KK-gluon and narrow $t\bar{t}$ resonances for different $t\bar{t}$ resonance mass points. In each figure, subfigure (a) uses the algorithm which ignores object resolution. In subfigure (b), the algorithm which accounts for object resolution is used. Finally, in subfigure (c), the effective mass distributions are also compared.
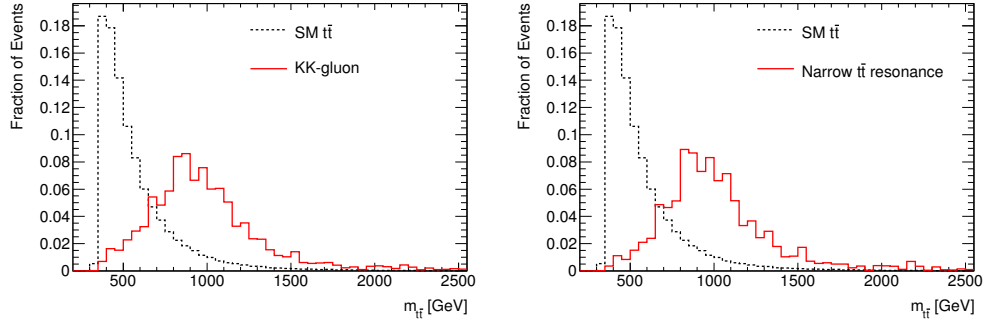
(a) $m_{t\bar{t}}$ using kinematically constrained neutrino solution.
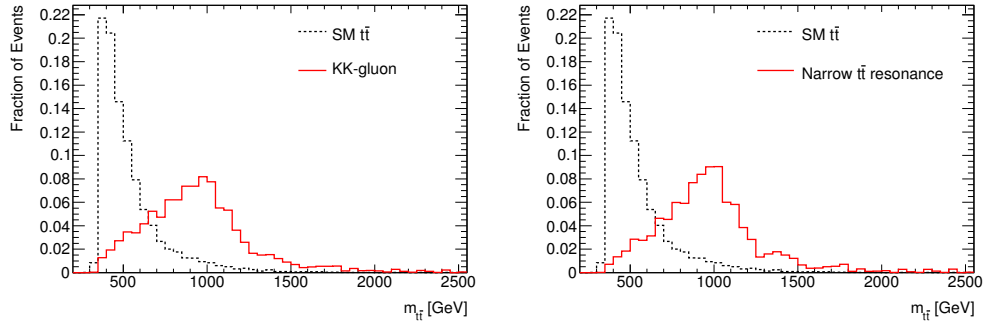
(b) $m_{t\bar{t}}$ using the neutrino solutions from the kinematic likelihood fitting method.
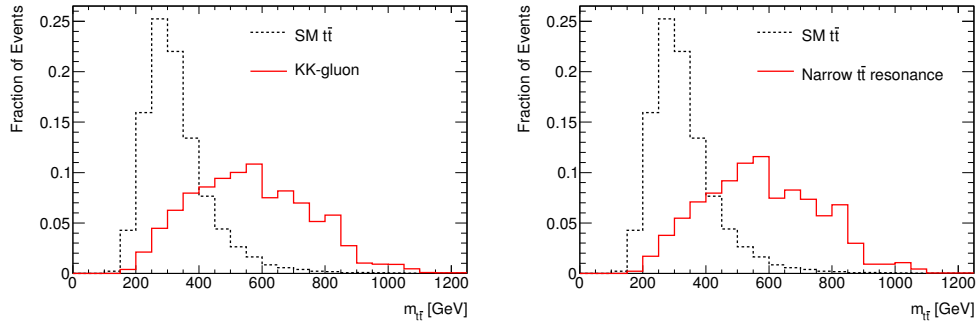
(c) $H_T + E_T^{miss}$

Figure 7.4: In (a) and (b), the SM $t\bar{t}$ (black) and invariant mass using neutrino solutions obtained while ignoring object resolution and accounting for object resolution are shown for a $t\bar{t}$ resonance (red), respectively. In (c) the effective mass is shown for both the SM $t\bar{t}$ (black) and for a $t\bar{t}$ resonance (red). Distributions on the left correspond to a 1 TeV KK-gluon while distributions on the right correspond to a narrow $t\bar{t}$ resonance.
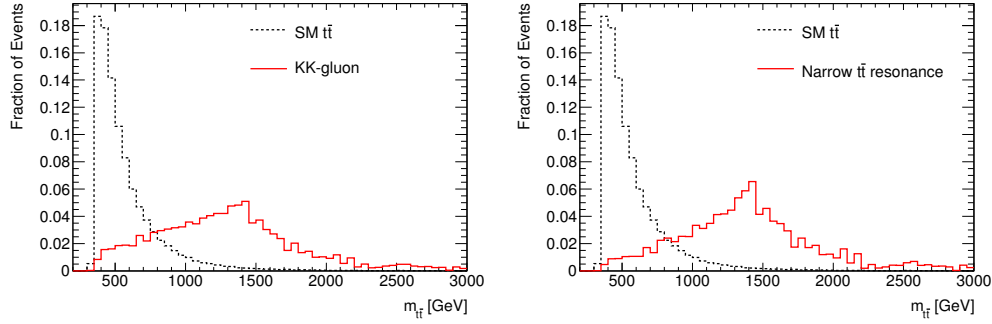
(a) $m_{t\bar{t}}$ using kinematically constrained neutrino solution.
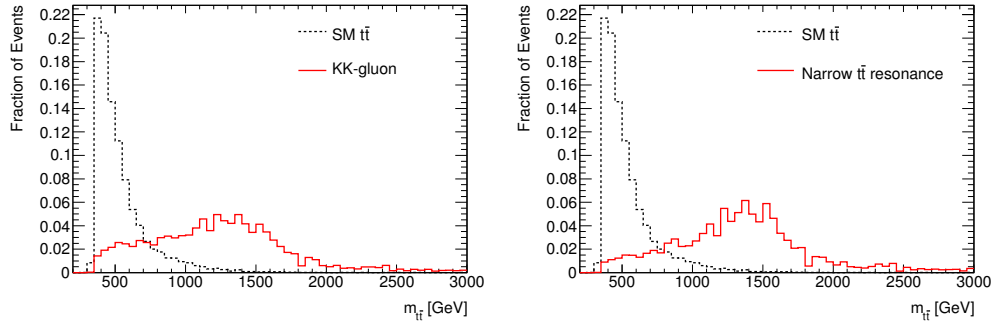
(b) $m_{t\bar{t}}$ using the neutrino solutions from the kinematic likelihood fitting method.
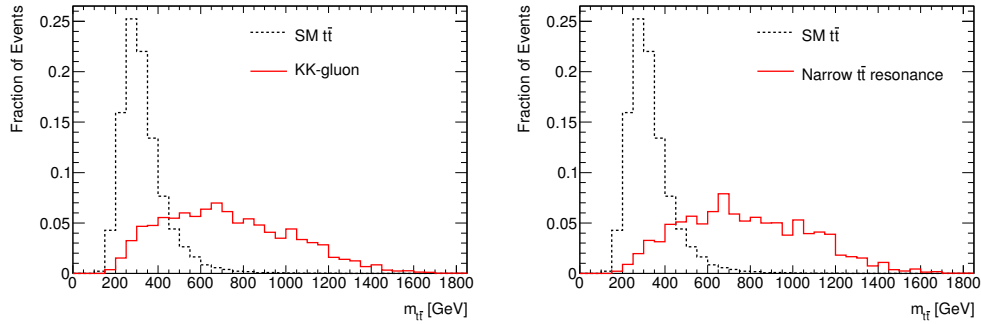
(c) $H_T + E_T^{miss}$

Figure 7.5: In (a) and (b), the SM $t\bar{t}$ (black) and invariant mass using neutrino solutions obtained while ignoring object resolution and accounting for object resolution are shown for a $t\bar{t}$ resonance (red), respectively. In (c) the effective mass is shown for both the SM $t\bar{t}$ (black) and for a $t\bar{t}$ resonance (red). Distributions on the left correspond to a 1.5 TeV KK-gluon while distributions on the right correspond to a narrow $t\bar{t}$ resonance.
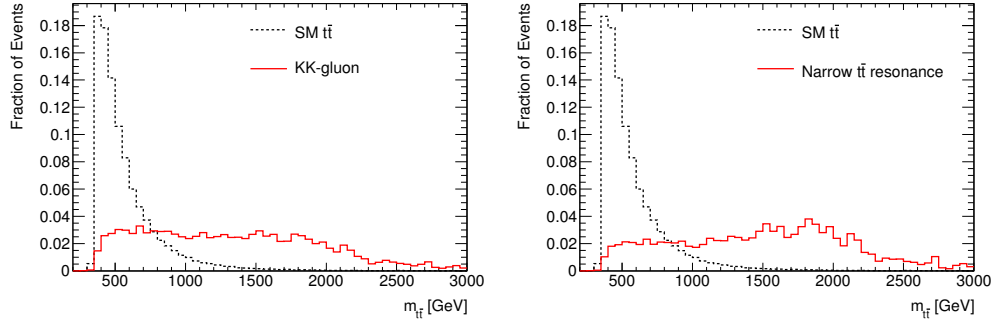
(a) $m_{t\bar{t}}$ using kinematically constrained neutrino solution.
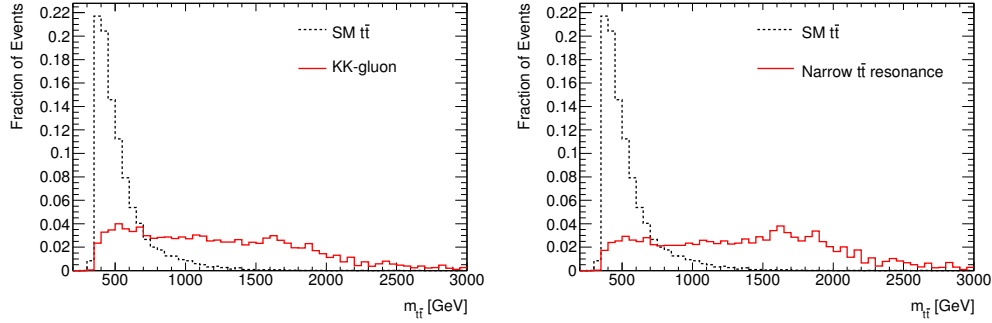
(b) $m_{t\bar{t}}$ using the neutrino solutions from the kinematic likelihood fitting method.
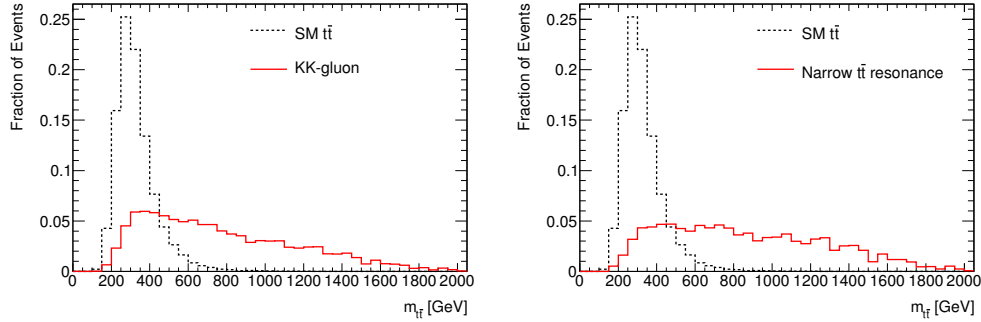
(c) $H_T + E_T^{miss}$

Figure 7.6: In (a) and (b), the SM $t\bar{t}$ (black) and invariant mass using neutrino solutions obtained while ignoring object resolution and accounting for object resolution are shown for a $t\bar{t}$ resonance (red), respectively. In (c) the effective mass is shown for both the SM $t\bar{t}$ (black) and for a $t\bar{t}$ resonance (red). Distributions on the left correspond to a 2 TeV KK-gluon while distributions on the right correspond to a narrow $t\bar{t}$ resonance.

7.3 Expected Limits

In order to quantify the performance of the $t\bar{t}$ mass reconstruction, the upper limit on the cross section using the effective mass and the analytic invariant mass reconstruction is compared. To do this, upper limits on the KK-gluon cross section are set by using both discriminating variables. This is done by creating a likelihood function, based on the Poisson probability, which is a function of the number of signal and background events in each bin of the $m_{t\bar{t}}$ spectrum. Since this method has not been performed on data, no observed limits are included. Separately, the invariant mass and effective mass distributions are used to calculate an expected limit for different KK-gluon masses between 500-2400 GeV. A brief description of the limit setting procedure is given in Appendix A.

7.3.1 Limits Ignoring Object Resolution Effects

In Figure 7.7, the expected limits are shown for a search for the KK-gluon using the effective mass and invariant mass calculated with truth level neutrino four-vectors. Using truth level neutrinos represents the best case performance for the invariant mass observable.
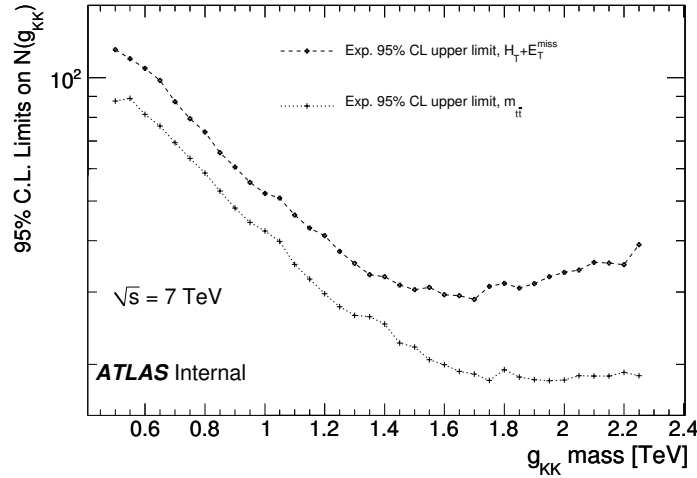
Figure 7.7: Expected upper limit on the number of KK-gluon events using the effective mass and the invariant mass. The invariant mass uses truth level neutrinos, providing a best case scenario of the algorithm.

In practice, neutrino solutions are not reconstructed perfectly. In fact, large broadening in the invariant mass is seen when analytic neutrino solutions are used and as a result the expected limits using the invariant mass observable is degraded. The expected limits are shown below in Figures 7.8 and 7.9 for a KK-gluon and a narrow $t\bar{t}$ resonance, respectively. In these figures, the expected limits set by the invariant mass and the effective mass are plotted on the same axis for a direct comparison.
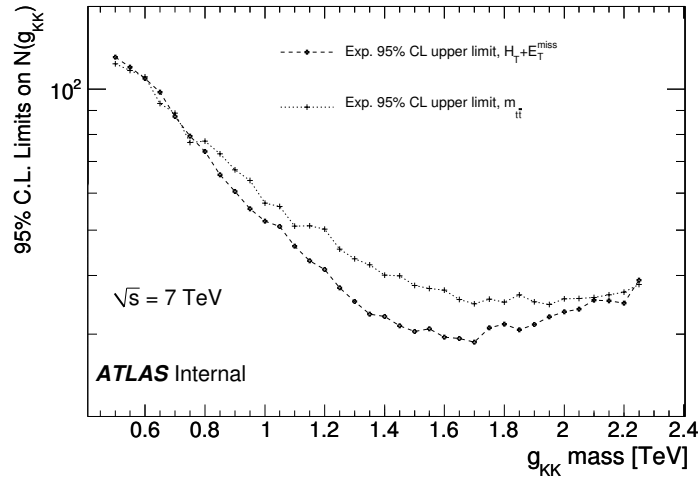
Figure 7.8: Expected limits on the number of KK-gluon events. The expected limits are obtained using the reconstructed invariant mass with selected neutrinos from kinematic constraints along with the expected limits of effective mass observable, shown for comparison.

Figure 7.9: Expected limits on the number of narrow $t\bar{t}$ resonance events. The expected limits are obtained using the reconstructed invariant mass with selected neutrinos from kinematic constraints along with the expected limits of effective mass observable, shown for comparison.

Comparing the above limit distributions, the effective mass appears to provide a betters sensitivity for a larger range of invariant masses. In fact, for the KK-gluon (large decay width), the effective mass performs the same or better over the entire mass spectrum. In comparison, for the narrower $t\bar{t}$ resonance, there is a cross-over point for higher mass, just below 2 TeV, where the invariant mass sets a better expected limit. In this mass region, the invariant mass for the narrower $t\bar{t}$ resonance still has a slightly larger peak contribution at the pole mass relative to the parton luminosity tail as observed in Figure 7.2. In contrast, for the broader resonance there appears to be a larger fraction of events in the low mass tail as observed in Figure 7.1.

7.3.2   Limits Using Kinematic Likelihood Fitting

Since the invariant mass distributions show some improvement, particularly in the background distributions, when using the kinematic likelihood fitting algorithm, the sensitivity of the search when accounting for resolution should have some improvement as well. Be-

low, in Figure 7.10, the limit obtained by the invariant mass is compared to the effective mass is shown.
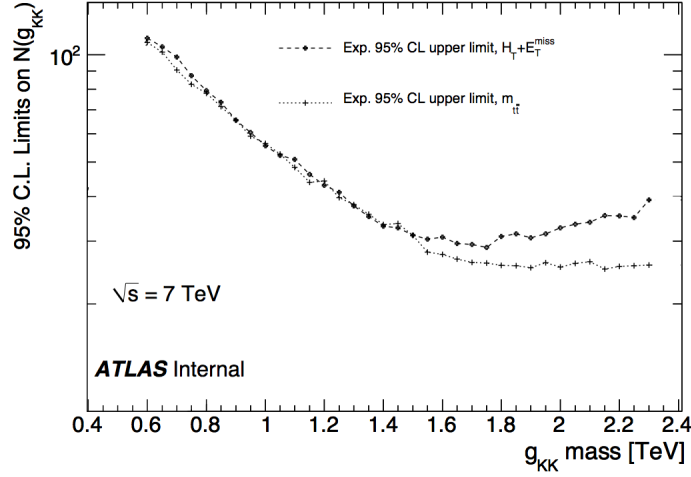
Figure 7.10: Expected limits on the number of KK-gluon events. The expected limits are obtained using the reconstructed invariant mass with selected neutrinos from kinematic likelihood fitter algorithm, along with the expected limits of effective mass observable, shown for comparison

In comparison to the limit distributions shown in figure 7.8, an improvement can be seen in the limit set by the invariant mass. There is, however, no consistent improvement over the entire mass spectrum.

However, when the narrow resonance is considered there is a clear improvement over the entire mass range, as seen in Figure 7.11.

The ratio of the limits on the number of events placed by both the $H_T + E_T^{miss}$ and $m_{t\bar{t}}$ is shown in Figure 7.12. An improvement between $10\% - 20\%$ for a narrow $t\bar{t}$ resonance with mass less than $1500\,\text{GeV}$ is obtained, with up to nearly a factor of 2 for larger masses.
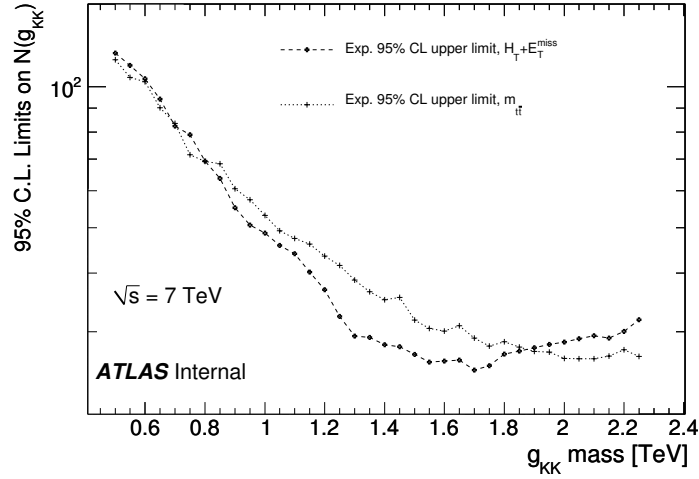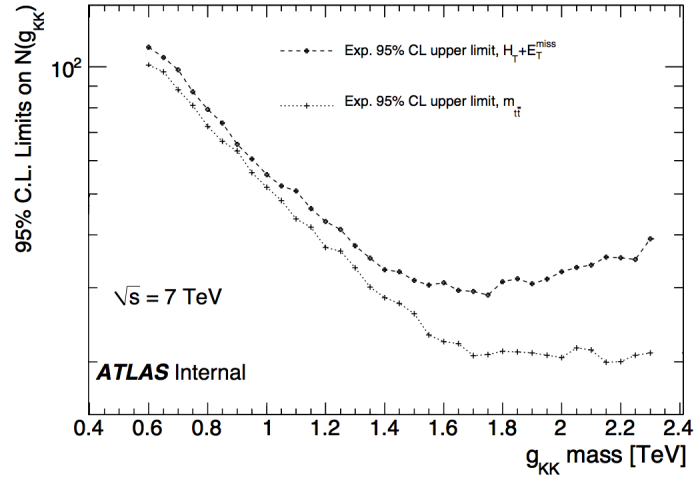
Figure 7.11: Expected limits on the number of narrow $t\bar{t}$ resonance events. The expected limits are obtained using the reconstructed invariant mass with selected neutrinos from kinematic likelihood fitter algorithm, along with the expected limits of effective mass observable, shown for comparison
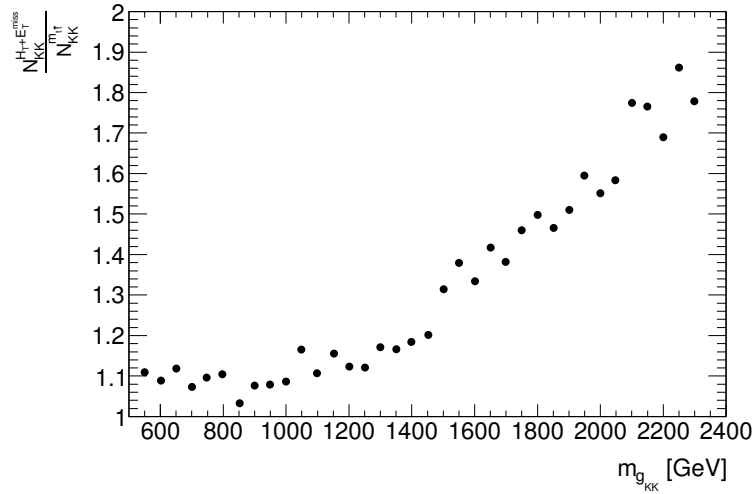
Figure 7.12: Ratio of the limits of number of narrow $t\bar{t}$ resonance events set by the effective mass and the invariant mass.

Chapter 8

Summary and Conclusions

The unprecedented high center of mass energy and high luminosity of the LHC enables the search for physics beyond the Standard Model in a new kinematic region, inaccessible to previous experiments. Many theoretical models predict new massive particles, some of which decay preferentially to top quark pairs. Of the possible $t\bar{t}$ decay channels, the selection criteria in the dilepton channel provide a highly pure $t\bar{t}$ sample, with few non-$t\bar{t}$ background events. The invariant mass provides the most important observable to establish a potential signal in the search for new massive particles. The benchmark model studied in this thesis is a massive KK-gluon with strong top quark coupling as predicted by the RS extra dimension model. Reconstructing the KK-gluon invariant mass is complicated by the presence of neutrinos that are not detected by the ATLAS detector. Using kinematic constraints from the well known masses of the top quark and the W boson as well as the measured missing momentum one can solve for the neutrino kinematics up to a four-fold ambiguity and reconstruct the KK-gluon invariant mass.

Preliminary results of the analytic mass reconstruction algorithm show that it provides poorer sensitivity to a KK-gluon signal in comparison to using the effective mass. However, the sensitivity of the invariant mass observable for a narrow $t\bar{t}$ resonance, when the resolution of measured objects is taken into account, shows an improvement between 20% to 90% over the studied mass range of 550 – 2350 GeV.

Further improvements to the analytic mass reconstruction can be made by the inclusion of additional jets and b-tagging information to the algorithm. On a statistical basis, the kinematic fitter can be used to extract the correct jet-parton assignment based on the

permutation with the highest likelihood.

Moreover, optimization of the lepton isolation requirements is essential to account for the collimated decay products of boosted top quarks. A promising new lepton isolation criteria, for boosted top quarks, referred to as the mini-isolation has recently been suggested [37, 38]. The mini-isolation requirements depend on the lepton p_T, with high efficiency for signal events, 95% (98%) for muons (electrons).

All distributions shown in this thesis are for events produced with pp collisions at a center of mass energy of 7 TeV. The center of mass energy of the LHC has increased to 8 TeV in 2012, and is set to further increase to 13 and ultimately 14 TeV after future upgrades. An increase in center of mass energy will lead to an increased sensitivity to high mass KK-gluons due to an increase in production cross-section. Another effect that arises from the increase in the center of mass energy is a decrease in the parton luminosity tail which will provide better separation between signal and background.

The next iteration of this analysis must also include the small non-top background contributions ignored in this thesis in order to provide a full description of the expected background in the ATLAS data. Sources of systematic uncertainty and their effects on the analysis must be evaluated. With all ingredients in place, the analysis can be applied to ATLAS data.

Appendix A

Jet Selection

Another complication comes from the 2-fold ambiguity which is a result of the assignment of the 2 jets to *b*-quarks in the decay of each top quark. There is a further ambiguity in jet selection and assignment which arises due to the fact that there is a substantial fraction of events with more than two jets which pass event and object selection. In Figure A.1, the distribution of the number of jets is shown for $t\bar{t}$ dilepton events. For events with *n* number of, the jet assignment increases to a *n*-fold ambiguity, rather than a 2-fold ambiguity. In order to appropriately reconstruct the correct neutrino four-vectors, it is import that the appropriate jet is matched to the correct branch of the top quark decay.
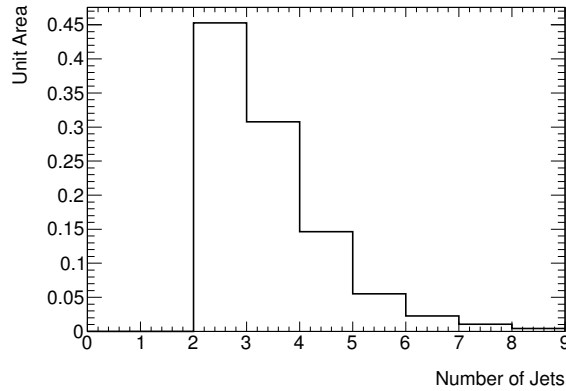

Figure A.1: Fractional number of jets passing object and event selection cuts in a KK-gluon MC sample of 1 TeV.

Two scenarios are considered for jet selection: either the jet corresponding to the small-est angular distance, $\Delta R(\ell, jet)$, can be chosen as the jet coming from the same top decay as the lepton or the two leading (highest-p_T) jets can be chosen. In boosted scenarios, the distance $\Delta R(\ell, jet)$ should be minimized since final state particles from boosted top decays are collimated, as discussed and depicted in Figure 4.11, motivating the former. At the same time, one also expects the jets from the hard scattering events to have the highest-p_T quarks and the other lower-p_T quarks to originate from initial and final state radiation, underlying events, or pile-up. The efficiencies of both jet selections criteria are given in Table A.1 for a 1 TeV KK-Gluon MC sample. A reconstructed jet with the smallest ΔR between the reconstructed jet and generator level parton, up to $\Delta R = 0.4$, is taken to be truth matched.

Table A.1: Efficiencies for a 1 TeV KK-Gluon MC sample for two different jet selection criteria.

Method	Number of Solutions	From Total	Neither Matches	One Jet Matches	Both Jets Match
ΔR	0	0.15	0.41	0.54	0.05
	> 0	0.85	0.14	0.22	0.64
Leading Jets	0	0.07	0.24	0.64	0.12
	> 0	0.93	0.32	0.07	0.61
Leading Jets, KL Fitter	0	0.12	0.64	0.33	0.03
	> 0	0.88	0.26	0.13	0.61

It is reasonable to expect no solutions if the incorrect particle kinematics are provided as input to the constraint equations of the $t\bar{t}$ system. The inability to find solutions if these constraints are not met is seen from the results in Table A.1. For the case where no solutions are obtained using the 2 leading jets (smallest $\Delta R(b, \ell)$), 88% (95%) of these events have at least one incorrect jet (not matched to truth b parton) provided as input to the mass reconstruction algorithm. However, it is reasonable to obtain solutions even when the correct jets are not chosen although no correlation between the true neutrino four-vectors and the analytically calculated neutrino solutions is expected.

The distribution of the number of jets for the subset of events where no solution is found

is given in Figure A.2 for both jet selection options. When using the smallest $\Delta R(b,\ell)$ as the criteria for jet selection, a large fraction of events where no solutions are found occurs for events with exactly 2 jets. This gives clear indication that choosing the two leading jets provides a better jet selection criteria because one expects that the jets in events with exactly 2 jets are in the predominantly originate from the decay of a top quark. In contrast, only a small fraction of the total events where no solution are found are events with only 2 jets satisfying jet selection criteria.

(a) Leading jets

(b) Minimum $\Delta R(b,\ell)$
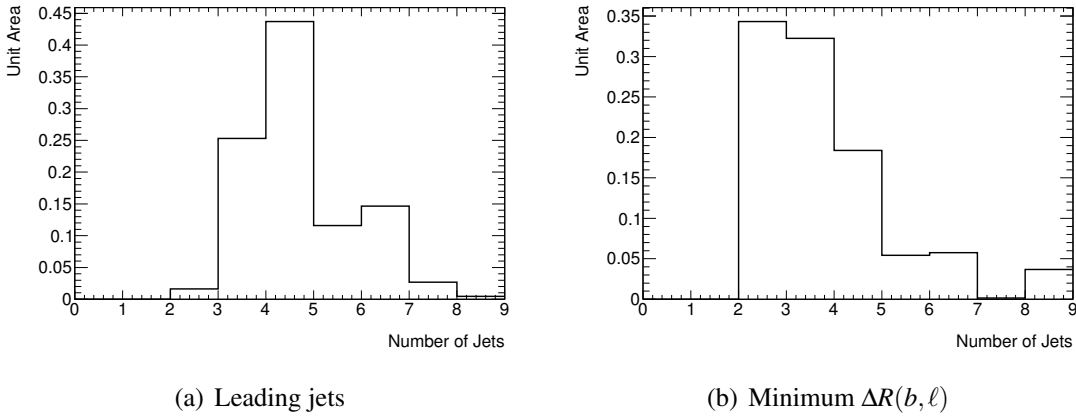
Figure A.2: Fractional number of jets passing object and event selection cuts in a KK-gluon MC sample of 1 TeV, when no neutrino solutions are obtained in the analytic mass reconstruction algorithm when (a) 2 leading jets and (b) jets with smallest $\Delta R(b,\ell)$ are used as inputs into the neutrino reconstruction algorithm.

Appendix B

Two-Dimensional Invariant Mass Distributions

The two-dimensional distributions between the invariant mass which uses truth neutrinos and those which use neutrino solutions selected by the individual constraints presented in chapter 5. These distributions show the spread, per event, that the mass reconstruction and neutrino solution finder generates.

In Figure B.1, only minimal broadening is seen, which is introduced by the both the use of the pole mass of the W bosons and top quarks as inputs into the mass reconstruction. Broadening can also be introduced by the neutrino solution that is selected. Overall, however, there is good agreement between both distributions. This is demonstrated by the clear line along the diagonal, which represents events reconstructed with the same mass.

Comparatively, in Figure B.2, large broadening is seen between the distributions which use truth level neutrinos and those which reconstructed neutrino solutions. These figures do not take into account the resolution of the leptons, jets, and missing energy. Here, one does see a higher concentration of events on the diagonal, however a large spread between the invariant mass distributions is evident.

(a) p_T^{ν}/p_T^{ℓ}

(b) $\Delta R(\ell, \nu)$

(c) E^{ν}/E^{ℓ}

(d) p_T^{ν}/p_T^{t}

(e) $\Delta R(t, \nu)$

(f) E^{ν}/E^{t}

(g) p_T^{ν}/p_T^{b}

(h) $\Delta R(b, \nu)$

(i) E^{ν}/E^{b}

Figure B.1: The 2-dimensional distribution of the invariant mass using generator level neutrino four-vectors in the mass reconstruction and using analytic neutrino solutions with highest probability using kinematic constraint listed in the subfigure caption. Analytic neutrino solutions are determined using generator level objects, and assumed pole masses.

(a) p_T^ν/p_T^ℓ

(b) $\Delta R(\ell,\nu)$

(c) E^ν/E^ℓ

(d) p_T^ν/p_T^t

(e) $\Delta R(t,\nu)$

(f) E^ν/E^t

(g) p_T^ν/p_T^b

(h) $\Delta R(b,\nu)$

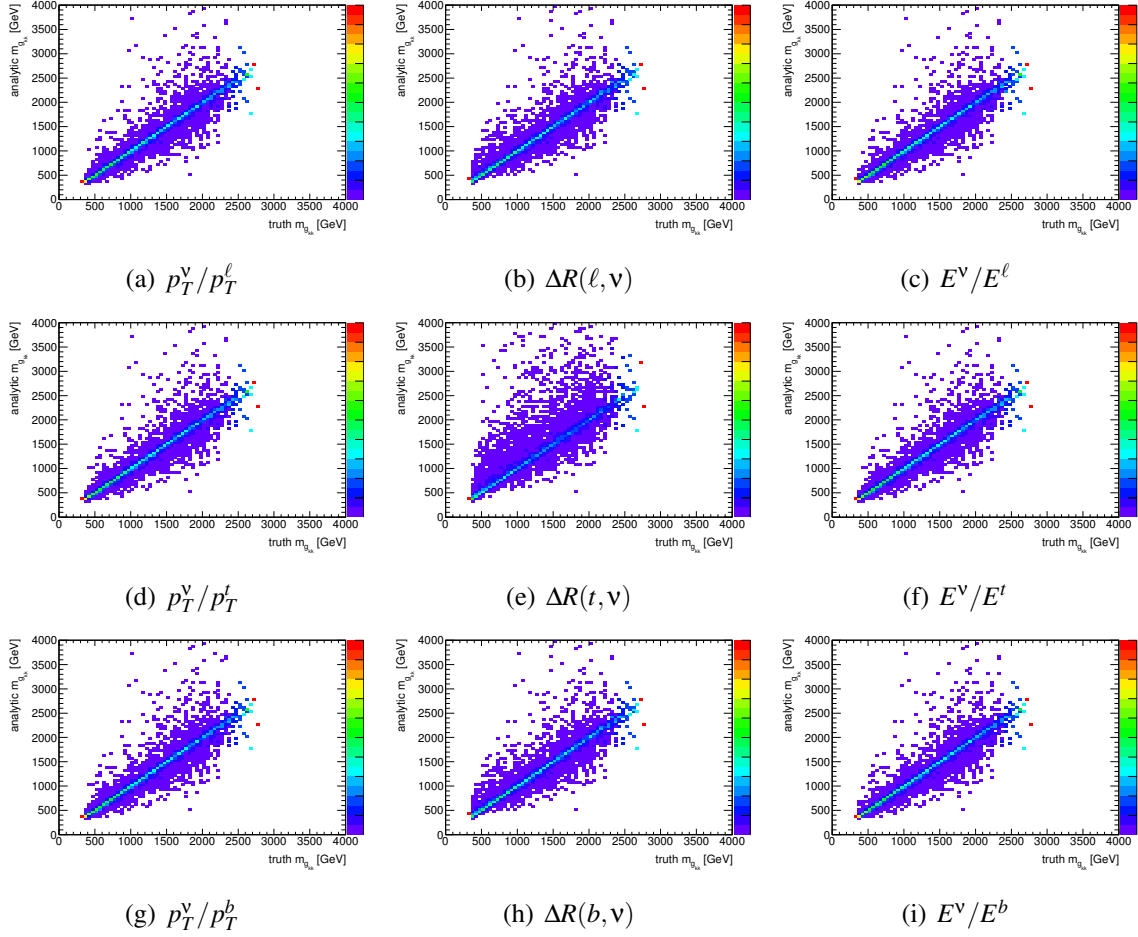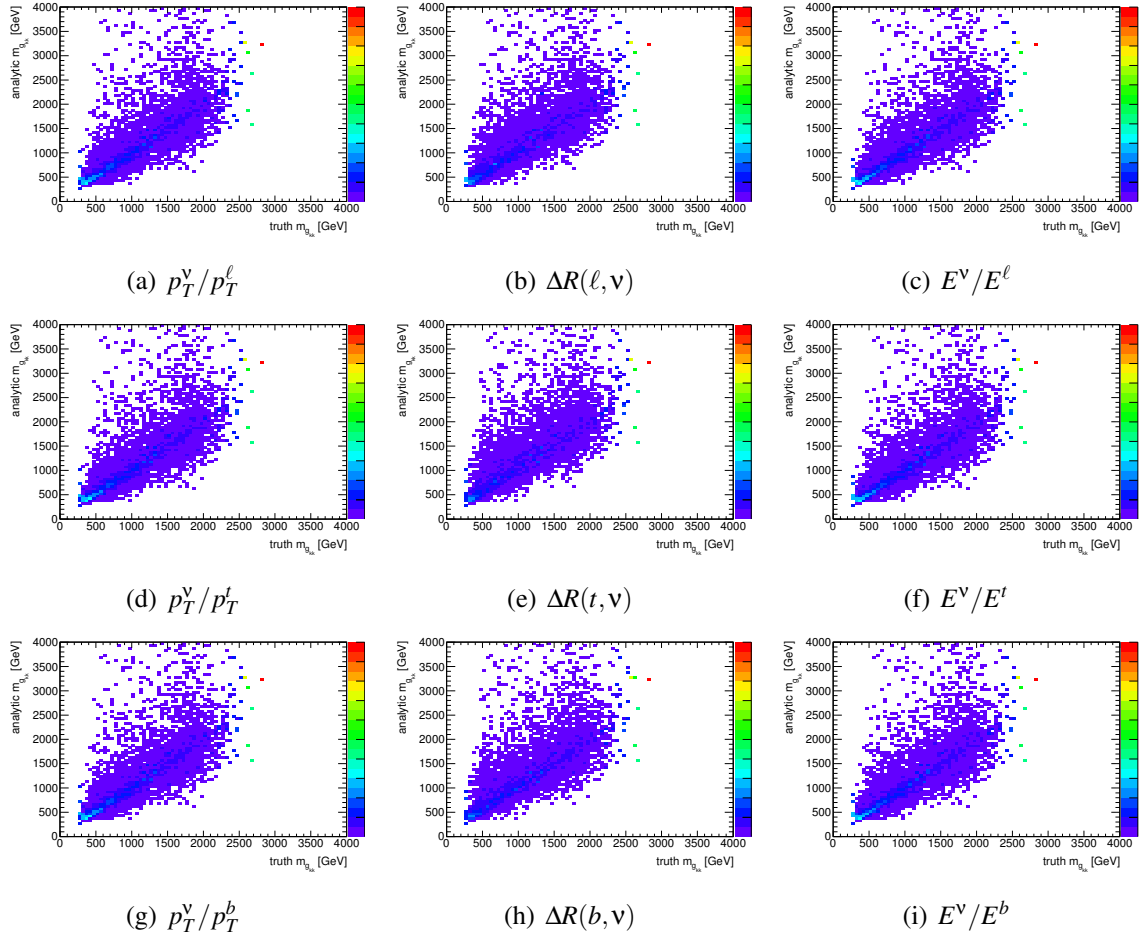(i) E^ν/E^b

Figure B.2: The 2-dimensional distribution of the invariant mass using generator level neutrino four-vectors in the mass reconstruction and using analytic neutrino solutions with highest probability using selection criteria listed in the subfigure caption. Analytic neutrino solutions are determined using reconstructed level objects, and top and *W* boson pole masses in equation 5.2.

Appendix C

Limit Setting Procedure

In chapter 7, the performance of the invariant mass and the effective mass were compared by computing the expected upper limits each observable set on the cross-section of the $t\bar{t}$ resonance.

These upper limits are calculated using a Bayesian approach [36]. To calculate the expected number of events, a likelihood function is defined. This likelihood function is represented by a Poisson probability and is given by:

$$\mathcal{L}(Data|N_{KK-gluon}) = \prod_{k=1}^{N_{bin}} \frac{\mu_k^{n_k} e^{-\mu_k}}{n_k!},$$

(C.1)

where n_k is the observed number of events in bin k, μ_k is the sum of KK-gluon signal and background expectation, $\mu_k = N_{sig} + N_{bg}$. The likelihood is a product of single bin Poisson probabilities over all bins in the spectrum of the observable. For the purpose of this thesis, only the irreducible Standard Model $t\bar{t}$ background is used as an estimate of the total number of background events.

Using Bayes' Theorem, the likelihood is converted into a Bayesian posterior probability density using a uniform (non-informative) prior, which is implemented using the Bayesian Analysis Toolkit [36]. The 95% Bayesian upper limit is obtained by integrating 95% of the posterior probability distribution, giving the number of KK-gluon events excluded at 95% C.L.

$$\int_0^{N_{KK-gluon}} P(N_{KK-gluon}|Data) = 0.95$$

(C.2)

A large set of pseudo-experiments are generated to obtain a distribution of the 95% CL Bayesian upper limit. The median of this distribution is taken to be the expected upper limits. This is repeated for the each mass point between 500-2300 GeV in 50 GeV mass increments. Five hundred pseudo-experiments were generated for upper limit plots shown in Figures 7.8 and 7.9. A more detailed description of the method is available in [39].

Bibliography

[1] D. Griffiths. *Introduction to Elementary Particles*. Wiley-VCH, 2nd edition, 2008.

[2] K. Nakamura et al. Review of Particle Physics. *J. Phys. G*, 37:075021, 2010.

[3] Y. Nambu. The Confinement of Quarks. *Scientific American*, 235(5):48, 1976.

[4] P. W. Higgs. Broken symmetries, massless particles and gauge fields. *Physics Letters*, 12(2):132, 1964.

[5] The ATLAS Collaboration. Observation of a new particle in the search for the Standard Model Higgs boson with the ATLAS detector at the LHC. *Phys. Lett. B*, 716:1, 2012.

[6] CMS Collaboration. Observation of a new boson at a mass of 125 GeV with the CMS experiment at the LHC. *Phys. Lett. B*, 716:30, 2012.

[7] O. Klein. Quantentheorie und fünfdimensionale Relativitätstheorie. *Z.F. Physik*, 37, 1926.

[8] T. Kaluza. Zum Unitätsproblem in der Physik. *Sitzungsber. Preuss. Akad. Wiss. Berlin. (Math. Phys.)*, 96, 1921.

[9] M. Shifman. Large extra dimensions: Becoming acquainted with an alternative paradigm. In *Crossing the boundaries:gauge dynamics at strong coupling*. World Scientific, 2009.

[10] Lisa Randall and Raman Sundrum. Large mass hierarchy from a small extra dimension. *Phys. Rev. Lett.*, 83:3370, 1999.

[11] H. Davoudiasl, J. L. Hewett, and T. G. Rizzo. Experimental probes of localized gravity: On and off the wall. *Phys. Rev. D*, 63:075004, 2001.

[12] CDF Collaboration. Observation of top quark production in $\overline{p}p$ collisions with the collider detector at fermilab. *Phys. Rev. Lett.*, 74:2626, 1995.

[13] D0 Collaboration. Observation of the top quark. *Phys. Rev. Lett.*, 74:2422, 1995.

[14] K. Agashe, A. Belyaev, T. Krupovnickas, G. Perez, and J. Virzi. LHC signals from warped extra dimensions. *Phys. Rev. D*, 77:015003, 2008.

[15] M. Benedikt et al. *LHC Design Report – The Injector Chain*. CERN, 2004.

[16] J.-L. Caron. The LHC injection complex. *LHC-PHO-1993-008*, 1993.

[17] The ATLAS Collaboration. The ATLAS Experiment at the CERN Large Hadron Collider. *JINST*, S08003, 2008.

[18] Useful Diagrams of Top Signals and Backgrounds. *http://www-d0.fnal.gov/Run2Physics/top/top _public _web_pages/top _feynman _diagrams.html*.

[19] The ATLAS Collaboration. Electron performance measurements with the ATLAS detector using the 2010 LHC proton-proton collision data. *Eur. Phys. J*, 1909, 2012.

[20] M. Cacciari, G. Salam, and G. Soyez. The anti-k_t jet clustering alogrithm. *JHEP*, 04:063, 2008.

[21] The ATLAS Collaboration. A search for $t\bar{t}$ resonances with the ATLAS detector in 2.05 fb^{-1} of proton-proton collisions at $\sqrt{s} = 7$ TeV. *Eur. Phys. J. C.*, 72:2083, 2012.

[22] S. Agostinelli et al. Geant4 - A Simulation Toolkit. *Nucl. Instr. and Meth. A.*, 506(3):250–303, 2003.

[23] Top Working Group. Private Communications. *https://twiki.cern.ch/twiki/bin/view/AtlasProtected/TopMC2010*.

[24] S. Frixione and B.R. Weber. Matching NLO QCD computations and parton shower simulations. *JHEP*, 06(029):013004, 2006.

[25] G. Corcella et al. HERWIG 6: An event generator for hadron emission reactions with interfering gluons (including supersymmetric processes). *JHEP*, 0101:010, 2001.

[26] J.M. Butterworth, J.R. Foreshaw, and M.H. Seymour. Multiparton interactions in photoproduction at HERA. *Z. Phys.*, C72:637–646, 1996.

[27] Mangano M.L. et al. ALPGEN, a generator for hard multiparton processes in hadronic collisions. *JHEP*, 0307:001, 2003.

[28] J. A. et al. MadGraph/MadEvent v4: The New Web Generation. *JHEP*, 0709:028, 2007.

[29] T. Sjöstrand et al. High-Energy-Physics Event Generation with PYTHIA 6.1. *Computer Phys. commun.*, 235:238, 2001.

[30] M. Peskin and D. Schoeder. *An Introduction to Quantum Field Theory*. Westview Press, 1995.

[31] The ATLAS Collaboration. Prospects for early $t\bar{t}$ resonance searches in ATLAS. *ATL-PHYS-PUB-2010-008*, 2010.

[32] Lars Sonnenschein. Analytical solution of $t\bar{t}$ dilepton equations. *Phys. Rev. D*, 73:054015, 2006.

[33] Y. Bai and Z. Han. Top-antitop and Top-top Resonances in the Dilepton Channel at the CERN LHC. *JHEP*, 056, 2009.

[34] A.V. Prokhorov (originator). Encyclopedia of Mathematics. *http://www.encyclopediaofmath.org/index.php/Covariance*.

[35] J. Erdmann et al. Kinematic fitting of $t\bar{t}$ events using a likelihood approach - The KLFitter Package. *ATL-COM-PHYS-2009-551*, 2009.

[36] A. Caldwell, D. Kollar, and K. Kröninger. BAT - The Bayesian Analysis Toolkit. *Computer Physics Communications*, 180:2197, 2009.

[37] K. Rehermann and B. Tweedie. Efficient Identification of Boosted Semileptonic Top Quarks at the LHC. *JHEP*, 1103, 2011.

[38] The ATLAS Collaboration. A search for $t\bar{t}$ resonances in the lepton plus jet final state using 4.66 fb^{-1} of pp collisions at $\sqrt{s}$ = 7 TeV. ATLAS-CONF-2012-136, 2012.

[39] The ATLAS Collaboration. A Search for $t\bar{t}$ Resonances in the Dilepton Channel in $\mathcal{L} = 1.04$fb^{-1} of pp Collisions at $\sqrt{s} = 7$ TeV. *ATLAS-CONF-2011-123*, 2011.